Hydrogen Bonding and Covalent Coupling in Adsorbed Molecular Monolayers

Jason Michael Garfitt, MSc (hons)

Thesis submitted to the University of Nottingham

for the degree of Doctor of Philosophy

September 2014

Abstract

This thesis examines multiple different molecular networks adsorbed on several different substrates, namely, highly oriented pyrolytic graphite (HOPG), Au(111) and graphene.

STM investigations into hydrogen-bonded structures formed by closely related tetracarboxylic acid molecules were performed. The molecule p-terphenyl-3,5,3,5-tetracarboxylic acid (TPTC), which is known to form random tiling networks, was observed on a graphene on copper substrate. The network formed from deposition of TPTC from nonanoic acid was examined statistically. Aqueous solutions of TPTC were also examined on HOPG where a new structure, distinct from the random tiling, was observed. Aqueous solutions of related molecules biphenyl-3,3',5,5'-tetracarboxylic acid (BPTC) and quaterphenyl-3,3',5,5' -tetracarboxylic acid (QPTC), were also studied on HOPG. QPTC formed a similar structure to the aqueous solutions of TPTC, but BPTC formed two different phases, one of which was a kagome network. Addition of nonanoic acid to a dried network of TPTC deposited from aqueous solution resulted in solvent induced recrystallisation into a random tiling network comparable to that observed on graphene on copper, which was statistically analysed.

Studies investigating the potential for covalent bonded molecular networks identified two distinct phases of the molecule 1,3,5-Tri(4-bromophenyl)-benzene (TBPB) adsorbed on Au(111). Concentration variation indicates an island based growth mechanism for these domains from solution. Dimerisation of TBPB was achieved by deposition onto heated substrates and a discussion of possible reasons for the reaction termination at dimers is provided. Attempts to repeat the TBPB experiments on graphene on copper failed due to excessive corrosion. Variations using larger molecules failed

due to lack of solubility. Preliminary experiments on 10,10'-dibromo-9,9'-bianthryl (DBrBA) showed promise but were irreproducible, however micron scale dendritic structures were observed suggesting poor compatibility with the solvent.

Finally, a discussion of the development of a nickel catalysis based graphene fabrication method is given and the limits of what is achievable with this method are discussed.

The results from this thesis highlight the importance of solvent selection for the future understanding of molecular network fabrication. We also demonstrated the feasibility of covalently bonded networks prepared in ambient conditions.

Keywords: Nano, Scanning tunnelling microscope, STM, SPM, microscopy, Au, gold, graphite, HOPG, graphene, tetracarboxylic, conjugated, molecular networks, self assembly, monolayer

Acknowledgements

Firstly thanks to my supervisor Peter Beton for his guidance thoughout my PhD studies. Also thanks is given to Izabela Cebula for her contributions to the raw data compiled to produce the tiling statistics on graphene on copper, and James C. Russell for his collaboration with the work on saturated solutions of TBPB. Additional thanks to J. Stirling, A. Summerfield and J. O. F. Thompson for various discussions and morale raising and most importantly to Fiona M. Stewart.

And finally, I would like to thank the EPSRC (engineering and physical sciences research council) for funding this work.

EPSRC
Engineering and Physical Sciences
Research Council

List of Publications

A. J. Pollard, R. R. Nair, S. N. Sabki, C. R. Staddon, L. M. A. Perdigao, C. H. Hsu, J. M. Garfitt, S. Gangopadhyay, H. F. Gleeson, A. K. Geim, and P. H. Beton. *Formation of Monolayer Graphene by Annealing Sacrificial Nickel Thin Films* J. Phys. Chem. C Volume: 113 Issue: 38 Pages: 16565-16567

Russell, James C. and Blunt, Matthew O. and Garfitt, Jason M. and Scurr, David J. and Alexander, Morgan and Champness, Neil R. and Beton, Peter H., *Dimerization of Tri(4-bromophenyl)benzene by Aryl-Aryl Coupling from Solution on a Gold Surface* J. Am. Chem. Soc. Volume: 133 Issue: 12 Pages: 4220-4223

Perdigao, Luis M. A. and Sabki, Syarifah N. and Garfitt, Jason M. and Capiod, Pierre and Beton, Peter. H. *Graphene Formation by Decomposition of C-60* J. Phys. Chem. C. Volume: 115 Issue: 15 Pages: 7472-7476

Contents

Chapter 1

Scanning Tunnelling Microscopy

1.1 Introduction to STM

Science has always questioned the composition of the materials in the world around us, and over time this has led to a focus on smaller and smaller objects. Historically, standard optical microscopes, which use visible light to resolve objects, had been used as the main form of microscopy since the mid 17th Century, popularised as a technique by Robert Hooke's *Micrographia* published by the Royal Society [1]. As the objects and their components being studied became smaller and smaller, optical microscopes reached a fundamental limit which could not be overcome, regardless of how well crafted their lenses and other components.

The resolution limit for optical microscopy is determined by the wavelength of light used, and for visible light the wavelength (λ) ranges from 380 nm to 770 nm. The maximum achievable spatial resolution, or the minimum separation of two distinguishable features (Δx_{min}) can be calculated using the Rayleigh criterion (equation 1.1).

$$\Delta x_{min} = \left(\frac{1.22\lambda}{nsin\theta}\right) \tag{1.1}$$

Here n is the refractive index of the media through which the light propagates and θ is half the angle from which light can enter the lens. For an ideal optical system operating in air, $\eta = 1$ and $\theta = 90°$ allowing us to resolve objects 437 nm or further apart [2].

To overcome this resolution limit several other types of microscopy have been developed. In electron microscopy a beam of electrons is used instead of visible light. It follows similar principles to the optical microscope, in that it uses lenses to focus the beam. The lenses used, however, are very different (using electromagnetic fields) and the electron beam propagates through vacuum, as air will scatter the beam. One microscopy technique that takes a completely different approach is what is known as scanning probe microscopy (SPM), in which images are constructed based on the interactions between a sharp probe and a surface.

The first type of SPM technique developed was scanning tunnelling microscopy (STM), invented by Gerd Binnig and Heinrich Röhrer in 1981 at the IBM Research Laboratory, Zurich, Switzerland. These researchers were awarded a share in the Nobel prize for Physics in 1986 for the development of this technique [3].

The STM has sufficient spatial resolution to distinguish individual atoms. For example, work by Hallmark *et al* in 1987 achieved sufficient resolution to observe the 0.28 ± 0.03 nm spacing of atoms in the (111) plane of gold [4].

Since its inception, STM has been used in areas such as supramolecular chemisty, electrochemistry, nano-electronics, topographic surface analysis, biochemistry, thin films, industrial coatings, spectroscopy and tribology [5,6]. The STM technique utilizes a flow of current, therefore it requires conducting substrates (it is also technically possible on thin layers of insulators on conductors).

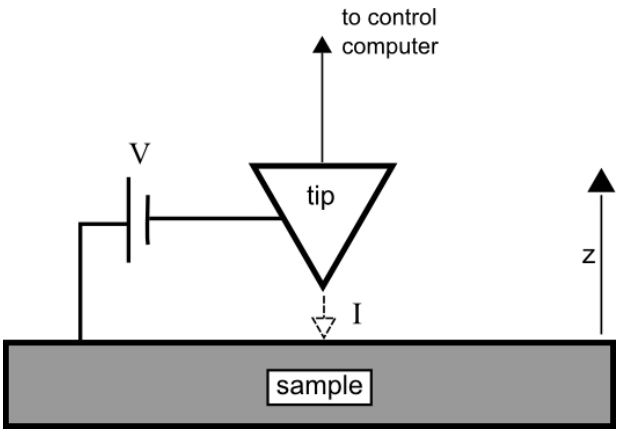

Figure 1.1: Simple geometry layout of an STM system showing tip, surface and an applied voltage between them.

1.2 Basic principles of operation

The major components of STM include a metallic probe, piezoelectric scanners and an electronic feedback system. The tip of the probe is so sharp that in the ideal situation there is only a single atom at the apex (in reality there are often several but this is discussed later in 1.3.1). The high resolution of STM is directly influenced by the sharpness of the tip. If such a tip is brought within sufficiently close proximity to an electrode, where there is a potential difference between the two, electrons can quantum mechanically tunnel across the gap between them.

1.2.1 Tunnelling

Quantum mechanical tunnelling is where a particle may pass through a potential barrier which, under classical mechanics, it should not be able to cross. All particles are described by an associated wavefunction. The time independent Schrödinger equation (equation 1.2) describes the wavefunction of particles whose energy depends only on position.

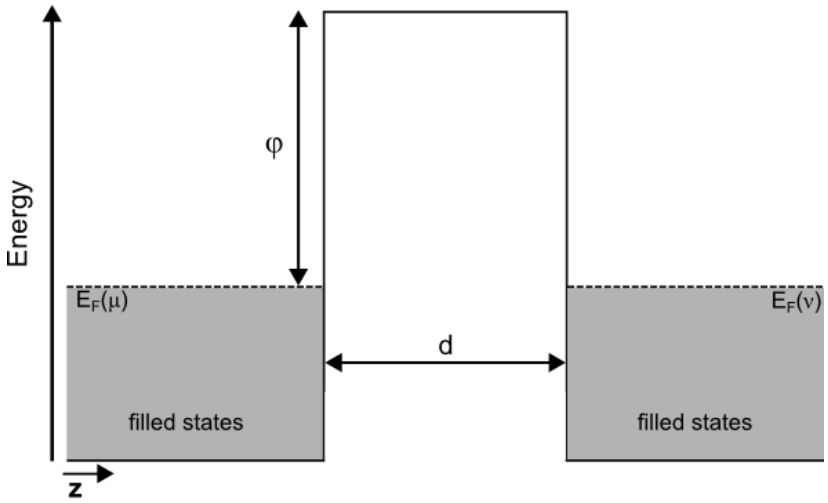

Figure 1.2: One-dimensional representation of two electrodes within close proximity, separated by a vacuum gap.

$$\frac{-\hbar^2}{2m}\frac{d^2\psi(z)}{dz^2} + U(z)\psi(z) = E\psi(z) \tag{1.2}$$

Here ψ is the wavefunction, $\hbar$ is Planck's constant divided by 2π, m is the mass of the electron, U is the potential energy function, z is the position of the particle (it will become clear why we are using the z axis later), and E is the energy of the particle.

The simplest model which describes vacuum tunnelling in the STM is a one-dimensional case where an electrode with an electron state labelled μ, is brought within close proximity of a second electrode with an electron state labelled ν. The vacuum gap between these two electron states acts as a potential barrier, a region through which, classically, the electrons within the electrodes cannot pass without first gaining more energy. The height of this barrier above the Fermi level is equal to the *work function* ϕ, which makes $U(z) = E_F + \phi$ inside the barrier. The separation between the two electrodes is d (figure 1.2).

Taking a low temperature approximation ensures that, for both electrodes, all the electronic states below the Fermi level are filled, and all those above the Fermi level are empty.

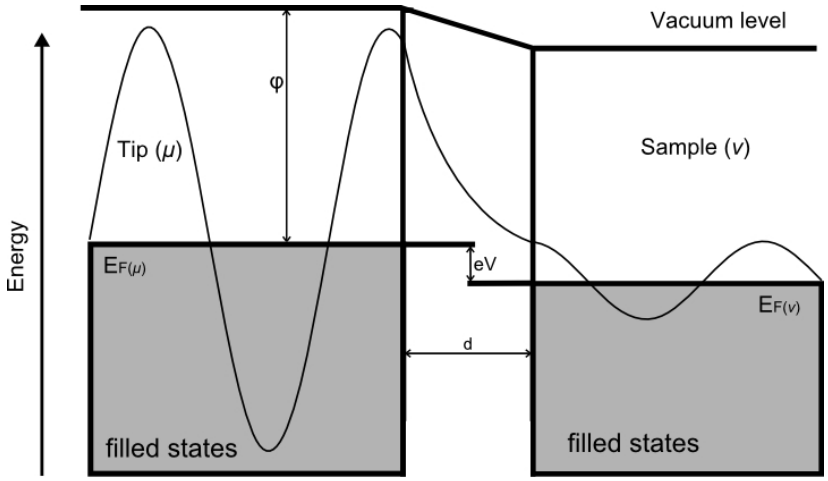

Figure 1.3: **One-dimensional potential barrier for vacuum tunnelling between two electrodes, such as an STM tip and sample. In this instance there is an applied potential difference V, between the two electrodes. The decay of the wavefunction through the barrier is shown.**

Classical mechanics does not allow an electron to penetrate the barrier region, however quantum mechanics does. The solutions of the Schrödinger equation in one dimension, within a rectangular barrier are of the form:

$$\psi = e^{\pm \kappa z} \tag{1.3}$$

where z is the direction along the line of separation between the two electrodes, and κ is governed by the relationship in (1.4):

$$\kappa^2 = \frac{2m_e\phi}{\hbar^2} \tag{1.4}$$

Here m_e is the mass of the electron, ϕ is the work function of the material (the energy required to extract electrons from the Fermi level of a metal across a surface carrying no net charge [7]). There is a finite electron probability close to the barrier and, as the wavefunction cannot be discontinuous, the wavefunction (ψ) must exponentially decay through the interior of the barrier. This decay into the barrier occurs at both sides of the barrier, and if the barrier is thin enough this results in wavefunctions from both sides overlapping within the barrier, leading to the possibility of transmission of an electron through the barrier in a way known as tunnelling [8–10].

As the probability density of the electron within the barrier is given by $|\psi|^2$, the tunnel current, I, will be proportional to the minimum value $|\psi|^2$ takes within the barrier. For a barrier of width d, this gives:

$$I \propto e^{-2\kappa d} \tag{1.5}$$

From Equation 1.5 we can see that this current will decrease exponentially as the distance between the electrodes is increased. To put some numbers to this, for a metal with ϕ between 4 and 5 eV (typical of many metals [11]), κ is close to 10 nm^{-1}. This leads to a drop in current by almost an order of magnitude for every 0.1 nm the vacuum gap is increased, resulting in a very high vertical resolution for the STM technique.

In the case shown in Figure 1.2 where both electrodes are made of materials with the same value of ϕ, no tunnelling will occur, as there are no empty states available to tunnel into. However, if a potential difference, V, is applied across the vacuum gap, the Fermi level of one electrode will shift up in energy relative to the other by an amount eV (see figure 1.3). This allows electrons in the filled states on one side of the barrier, to tunnel into vacant states on the other. Once a single electron has tunnelled from μ to ν across the vacuum gap, it will have left an empty state in μ, which allows tunnelling in the opposite direction. As tunnelling can occur in both directions (providing there is an available state to tunnel into) the measured tunnelling current is actually the net electron flow across the vacuum gap and not the total flow. Note that we are assuming only elastic tunnelling takes place in these models.

The larger the applied potential difference, the more states can tunnel and the higher the current will be for a certain gap width, d.

1.3 Tersoff-Hamann theory

Although the one dimensional approach offers us a simple model for tunnelling, it does not represent the true three dimensional nature of the system. Tersoff and Hamman [12] introduced a three-dimensional approach where they assume the end of a tip comes to a spherical point, with a radius of curvature ρ around a point r_0,confined within a spherical potential $V(r)$.

The main assumption of the theory is that the spherical electronic states in the tip, those that have an l (angular momentum) quantum number of zero, dominate over the other terms and so the others can be ignored.

Several authors [10, 13] quote a formula, attributed to Bardeen, for the tunnelling current from a first order perturbation theory approach as:

$$I = \frac{2\pi e}{\hbar} \sum_{\mu,\nu} f(E_\mu)[1-f(E_\nu)] - f(E_\nu)[1-f(E_\mu)]|M_{\mu\nu}|^2 \delta(E_\mu - E_\nu + eV) \quad (1.6)$$

$f(E)$ is the Fermi-Dirac distribution for the respective electrodes. The Fermi-Dirac distribution shows us the probability that a state with energy ε, is occupied [14]. The factor $f(E_\mu)[1 - f(E_\nu)]$ is the probability of an electron tunnelling across the vacuum gap from electrode μ to electrode ν.

With the low temperature approximation, there are no populated excited states, which sets all the states below the Fermi level to be full, and all those above to be empty. This simplifies equation (1.6) as we can only have $f(E) = 1$ or $f(E) = 0$. As such, $f(E_\mu)[1 - f(E_\nu)] = (1 - 0) = 1$ and $f(E_\nu)[1 - f(E_\mu)] = 1 - 1 = 0$ when a negative bias is applied to electrode μ, resulting in electrons flowing from μ to ν. A low voltage limit ensures that only those states at the Fermi level can contribute to the tunnelling phenomenon.

Applying these simplifications and taking the low voltage limit ($V \simeq 0$),

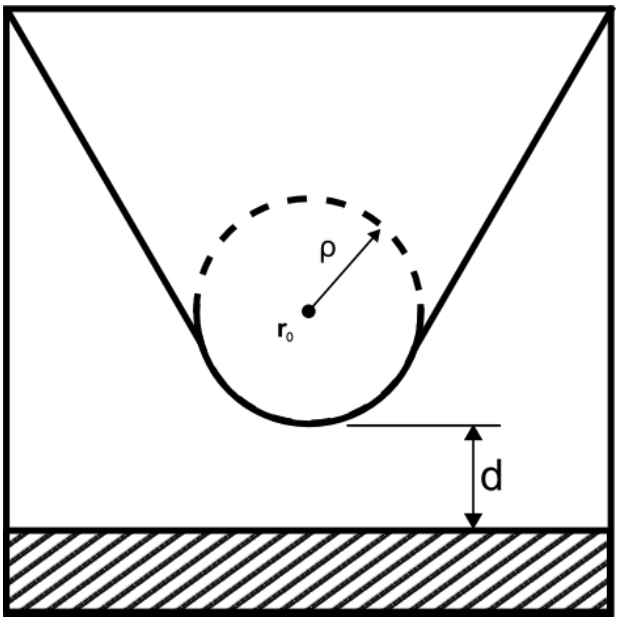

Figure 1.4: **Spherical Tip Apex:** The assumed tip apex geometry for Tersoff-Hamann theory. Radius of curvature ρ, center r_0 at a separation d from the surface along the z axis. Figure adapted from [12]

equation (1.6) reduces to:

$$I = \frac{2\pi}{\hbar} e^2 V \sum_{\mu,\nu} |M_{\mu\nu}|^2 \delta(E_\mu - E_F)\delta(E_\nu - E_F) \tag{1.7}$$

where μ and ν label the states on the tip and the sample respectively. The degree of overlap between the states in μ and the states in ν is represented by the term $|M_{\mu\nu}|^2$, known as the tunnelling matrix element, and Bardeen's method [15] can be rearranged to show that this can be expressed as,

$$M_{\mu\nu} = \frac{\hbar^2}{2m} \int d\mathbf{S}(\psi_\mu^* \nabla\psi_\nu - \psi_\nu \nabla\psi_\mu^*) \tag{1.8}$$

where the integral in equation 1.8 is over the surface of the tip.

The wavefunction used for the tip is modelled on a sphere of radius of curvature ρ with a centre r_0. It is assumed that the work function ψ for the tip is equal to that of the surface and that ψ_μ has no angular dependence (spherical tip states only).

$$\psi_\mu = \Omega_t^{-1/2} c_t \kappa \rho e^{\kappa\rho} (\kappa|\vec{r} - \vec{r_0}|)^{-1} e^{-\kappa|\vec{r}-\vec{r_0}|} \tag{1.9}$$

Here Ω_t is the volume of the probe and c_t is a normalization constant of order 1.

Tersoff and Hamann [12] use a general equation (1.10) for the wave-function of the sample..

$$\psi_\nu = \Omega_s^{-1/2} \sum_G a_G e^{(\kappa^2 + |\vec{\kappa_G}|^2)^{1/2} d} + e^{i\vec{\kappa_G}\vec{x}} \tag{1.10}$$

This equation uses the same definition of κ given in equation (1.4), has Ω_s as the sample volume, $\vec{\kappa_G} = \vec{\kappa_{||}} + \vec{G}$, where $\vec{\kappa_{||}}$ is the surface Bloch wave vector of the state, and $\vec{G}$ is a surface reciprocal-lattice vector [12], and d is the width of the vacuum gap. This general form should account for any general surface, with the sum over $\vec{G}$ becoming an integral for a non periodic surface.

If we substitute (1.10) and (1.9) into (1.8) and evaluate for G we can simplify $M_{\mu\nu}$ to become:

$$M_{\mu\nu} = \frac{-4\pi\hbar^2}{m} \kappa^{-1} \Omega^{-1/2} \kappa \rho e^{\kappa\rho} \psi_\nu(\vec{r_0}) \tag{1.11}$$

As this keeps $\psi_\nu(\vec{r_0})$ as a seperate factor we can see we do not need to make an assumption for ψ_ν to calculate our tunnelling current. Substituting this into (1.7) gives:

$$I \propto \sum_\nu |\psi_\nu(\vec{r_0})|^2 \delta(E_\nu - E_F) = n(\vec{r_0}, E_F) \tag{1.12}$$

The quantity $n(\vec{r_0}, E_F)$ is the local density of states at the Fermi level.

The local density of states is defined as the sum of the electron probability density ($|\psi|^2$) at a specified position (r_0) for all electronic states whose

energy lies within the specified energy range ($E_\nu - E_F$).

The tip images the local density of states (LDOS) at the Fermi level.

1.3.1 Breakdown of Tersoff-Hamann theory

There are several different ways in which the Tersoff-Hamann model breaks down. Real systems will have some degree of thermal energy, imperfect tips, and do show some image dependence on the voltage bias. Semiconductors have been shown to have a strong variation in the LDOS with respect to voltage [10], discontinuously so at band edges. A good example of how the dependence on voltage affects data can be seen in the case of III-V semiconductors such as GaAs. When imaging GaAs surfaces, a positive bias will reveal the position of the Ga atoms and a negative bias the As atoms [16]. This effect is due to the surface electronic structure, where occupied states are concentrated preferentially on the As atoms and unoccupied states on the Ga atoms [12].

Extension from the low voltage limit

The low voltage limit of the model discussed in the previous section accounts for electronic states within a small energy interval of the Fermi level. We can see from equation 1.7 that tunnelling current *does* depend on voltage and so this low voltage limit is not strictly correct. With a finite voltage the energy range of contributing states will be larger and may allow additional states to take part. This will change the measured local density of states.

Lang [17] gave an extension to the Tersoff-Hamann model which accounts for finite voltages under the condition that the bias voltage (V) is much less than the work function, ϕ of either the tip or sample.

$$I(V) \propto \int_{E_F}^{E_F+eV} n(\vec{r_0}, E)dE \tag{1.13}$$

Selloni *et al.* [18] introduce a κ independent term to account for the voltage dependence, however this still requires the assumption that the value of ϕ is the same for both tip and sample.

The fact that there is a dependence on voltage of all images opens up the field of scanning tunnelling spectroscopy. If there was no variation in tunnelling current as a function of voltage, all I-V spectra would be flat lines and this field of study would not exist.

Contributions from higher angular momentum states

Chen [19] showed that the Tersoff-Hamann model does not permit the formation of images with features of the order 0.3 nm or smaller. This includes atomic resolution images on close packed metal surfaces, several of which have been produced in the literature [20] and covers most other conducting elemental solids, which have an interatomic distance smaller than this limit. Although the assumption of a spherical tip state is good for some materials, such as sodium, which has a simplicity useful for theoretical models, for others like tungsten, which is a commonly used tip material in ultra high vacuum STM studies, it is not a complete picture. Chen showed [19] that the contribution of d (l=2) states accounts for 85% of total density of states for tungsten and attributed the contributions from these higher angular momentum states as the reason sub 0.3 nm resolution has been achieved.

Tip Anisotropy

A real tip is never perfectly spherical and the actual structure is rarely known (exceptions include carbon nanotube terminated and other chemically functionalised tips [21]), and tip anisotropy can cause significant deviation from this model. The STM image is "a convolution between the tip and the sample surface structure" [22] so naturally, any changes in the tip

state will affect the resultant image. In the extreme case of a forked tip this can lead to image artefacts where each single molecule or step will appear as a pair instead. One more assumption made in the Tersoff-Hamann model is that the work functions of both the tip and the sample are the same. This is often not the case as, for example, a tungsten tip imaging a gold (111) surface will have a variation in the work functions of 0.76 electron volts [11].

1.4 STM of adsorbed organic molecules

The situation covered in the model system of section 1.2.1 deals with only clean tip and sample electrodes but we should also consider the case of organic molecules on the sample.

The degree to which the states in the tip and sample overlap is described by the tunnelling matrix element $M_{\mu\nu}$ as shown in equation 1.8. If we were to change these states then we would change the tunnelling matrix element and therefore the measured current. In extended periodic crystalline structures, such as metals, the surface states are the Bloch wavefunctions of the crystallite. Bloch functions are a description of electron wavefunctions within a periodic potential such as an extended atomic lattice within a crystal. In the case of a single molecule, the periodic approach is invalid. Molecules are not as periodic or regular over the same length scale as crystals, and so a different approach is required.

Electronic wavefunctions in molecules are described by molecular orbitals. A molecular orbital is defined as "A one-electron wavefunction describing an electron moving in the effective field provided by the nuclei and all other electrons of a molecular entity of more than one atom" [7].

There are two main schools of thought as to the exact mechanism involved in the tunnelling of the molecule-substrate system [23].

The first school of thought proposes that tunnelling still occurs between

the metallic substrate and the tip, but the Bloch wavefunction of the surface state of the substrate is perturbed by the presence of the adsorbate molecule. The attractive forces of the nuclei can act to lower the work function of the substrate surface state. Therefore the STM image will be a map of changes in the local work function [24] in addition to changes in height.

The other school of thought [25] claims that the shape in which a molecule appears within the STM data corresponds to the molecular orbital involved in the tunnelling. That is, tunnelling occurs directly from the orbitals of the adsorbate molecule. For a system where the tip is grounded and the bias is applied to the sample, for $V > 0$ electrons tunnel from the highest Bloch wavefunction in the tip, to the lowest unoccupied molecular orbital (LUMO) in the sample. For $V < 0$ electrons will tunnel from the highest occupied molecular orbital (HOMO) in the sample to the lowest Bloch wavefunction in the tip. This only takes place if the potential difference provides sufficient energy for the transition to be possible.

Certain organic molecules also have a sufficiently conductive nature [26] to allow tunnelling from them, with the charging being neutralised by conduction to/from the underlying substrate. Such conductive molecules contain conjugated systems: an organic system of alternating single and double bonds, and often feature aromatic rings [7].

When imaging molecules, a much lower set point is typically used compared to plain substrates, e.g. 0.1 nA or lower compared to 1 nA for a bare metallic substrate. This is to increase the distance between the tip and the sample and to reduce the chances of the molecule being moved by the tip, as adsorbate manipulation with the tip is known to be possible [27].

1.5 Image formation

There are two main modes used for obtaining STM images: constant height mode, and constant current mode.

Constant height mode is a simpler mode of imaging, requiring no feedback loops, in which the tip is held at a fixed distance above the surface at the point of initial approach. The tunnelling current is measured as the probe is scanned across the surface. As the tunnelling current decreases exponentially with separation (equation 1.5), a very accurate height map can be obtained. This mode only requires piezo drives in the x and y directions once the approach is complete, however the tip can easily crash as it cannot react to raised features, so the applications of constant height mode are limited.

Constant current mode makes improvements on the older constant height mode by the addition of a Z piezo and a series of electronic feedback loops. A fixed value of current is set (normally in the range of a few pA -1 nA) and if a measured deviation from that current is detected, the feedback loops will adjust the z position of the tip in order to obtain the specified current once again.

1.5.1 Alternative sources of contrast

For the majority of samples, height is the greatest source of contrast in STM images. There are, however, other features which can contribute to contrast within images. The tunnelling current depends on the work functions of the materials of the sample and tip. If one of these work functions changes, e.g. due to change in elemental composition of a region of the sample [28], the tunnelling current will be affected. Unfortunately it is impossible to distinguish these contributions to the final signal, and so if elemental variation is expected to be an important factor, the use of a complementary technique is recommended to confirm this.

1.6 Piezo drive

The probe is manipulated by a piezo drive unit, consisting of three mutually orthogonal piezoelectric actuators. Piezoelectric materials expand in one lattice direction and contract in another upon the application of an electrical current. The most commonly used material for piezo scanners is the ceramic known as PZT ($[Pb(ZrTi)O_3]$ [10]. The z piezo controls the tip-sample separation, with the x and y piezos controlling the scanning.

The dimensional change is well defined and, when close to the equilibrium position, can be approximated to have a linear relationship to the applied voltage. At large voltages some degree of non-linearity can be observed [10, 29] along with some degree of hysteresis. The components of the piezo drive are typically of the order of 10^{-3} m.

Early STMs used simple piezoelectric tripod scanners, with a beam of piezoelectric material along each axis. Although very simple in design, construction was not easy [30], and there were several problems arising from the asymmetry in this type of scanner, including a large suceptibility to thermal drift [31]. The typical expansion/contraction responsiveness for a tripod scanner is 1.5 nm/V and the lowest mechanical response frequency is typically 5 kHz [32] (the higher this value, the less the scanner will be affected by noise).

Modern instruments (including those used for the research described in this thesis) use a tube scanner. Tube scanners have a compact and simple structure, high sensitivity, and a high resonant frequency. The tube scanner consists of a single hollow cylinder of piezoelectric material with four external electrodes dividing it into symmetrical quadrants, parallel to the axis of the tube, and a single internal electrode. Applying a voltage to any one of the outer quadrants will cause the material under that electrode to expand, and if an opposite voltage of equal magnitude is applied to the diagonally opposite electrode, the result is a bending of the whole tube perpendicularly to its axis. If the voltage is only applied to one of

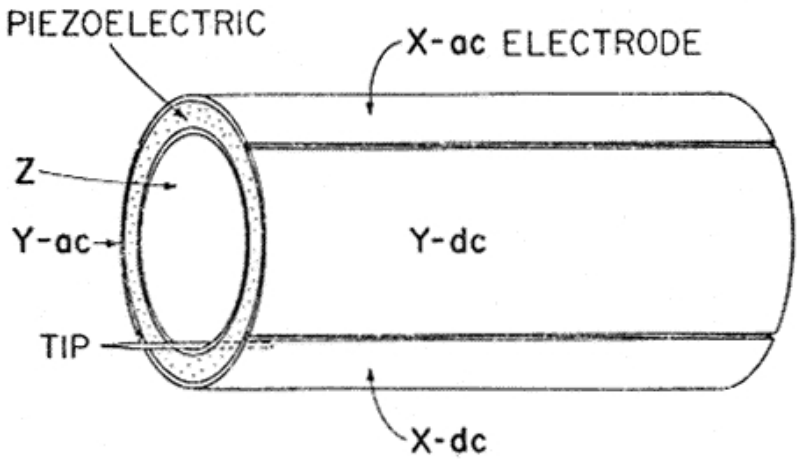

Figure 1.5: The piezo tube scanner, as used in most modern commercial systems. The outside is sectioned into four equal areas parallel to the tube, with opposite pairs used to control deflection of the tip in the x and y direction respectively. An inner electrode can be used to elongate the whole tube in the z direction [32].

the outer electrodes, an asymmetric stress develops in the tube, the inner electrode partially charges, and there is some loss of orthogonality in the tip motion [10]. A voltage applied to the internal electrode results in a uniform elongation of the entire tube.

The responsiveness is typically 5 nm/V, allowing for scanning over larger areas, and comparatively less non-linearity than the tripod scanner while scanning the same size area, due to lower voltage requirements. The mechanical resonances are much higher, typically 8kHz perpendicular to the tube axis and 40kHz parallel to the tube axis [32]. This allows for much higher scan speeds. The piezo tubes are also smaller than the tripod systems which leads to a much more compact STM.

1.7 Feedback electronics

Most imaging performed with STM is done in "constant current mode". The sample bias voltage and a desired tunnelling current are selected by the operator. Once the tip is brought sufficiently close to the the sample to reach the desired tunnelling current, scanning can proceed. Variations in the surface topography, and therefore the tip-sample separation, will lead to

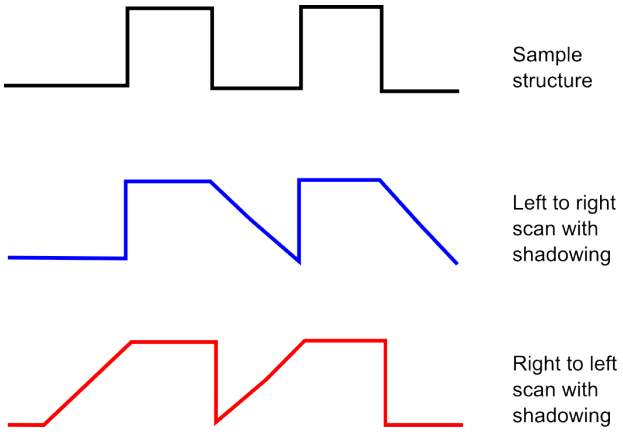

Figure 1.6: **Shadowing effect:** When scanning a raised block, a shadowing effect can occur due to low gains. The low gain leads to the z piezo responding slowly to step changes in surface height.

a change in tunnelling current (see 1.5), as will any change to the electronic structure caused by dopants or defects. The tip sample separation needs to be adjusted continuously throughout the scanning process in order to maintain a constant value for the tunnelling current.

Changes in the tunnelling current are monitored by a control system which adjusts the position of the z piezo accordingly. The contrast within the resulting STM image corresponds to the position of the z piezo within its range (usually black at maximum extension and white at maximum contraction). The ability of the feedback system to respond to changes in the tunnelling current is crucial. If the response rate is too low, it can damage the tip on high features, or lead to a shadowing effect on troughs (see Figure 1.6). The shadowing effect is an imaging artefact which arises from low gain values, when the position of the tip cannot respond quickly enough to a steep drop in height, following a raised feature. This is visible as a difference between the trace (left to right) and retrace (right to left) scan images.

The current flowing across the tunnel junction is measured and amplified by a current-to-voltage preamplifier placed as close to the tunnel junction as possible [10], in order to minimize the effects of any noise. The close proximity of this amplifier to the point of signal acquisition minimises the effects of noise throughout the rest of the electronic systems.

This signal is compared to a reference current to produce an error signal. The feedback control aims to minimise this error signal by means of a negative feedback loop. If the error signal shows that the measured current is larger than the set point current, the control system will send a voltage to the Z piezo causing it to contract, increasing the tip-sample separation. If the error signal shows the measured current is lower than the set point current, the control system will send a voltage to the Z piezo causing it to expand and close the gap. It should be noted that whether the measured current is subtracted from the set point current, or the set point subtracted from the measured current is arbitrary and as such the sign of the error signal can vary among different commercial suppliers. This has no effect on the final outcome.

How quickly a system responds to these changes and how large the steps it takes to compensate for these differences are governed by details within the feedback control system. Proportional-integral-derivative type feedback controllers are commonly used in scanning probe microscope systems.

1.7.1 PID feedback controller

The Proportional-integral-derivative control algorithm has been used for the control of many different processes since the 1940s [33] and is especially effective in single-input-single-output systems, such as the case of STM, where the single input is the tunnelling current, and the single output is the Z piezo position. It consists of three components, and the final correction is given by the summation of these 3 modes.

Proportional mode

The proportional mode makes adjustments (as its name suggests) proportional to the error signal. The response is shown in equation 1.14

$$\Delta V_{out} = K_p V_{in} + I_p \tag{1.14}$$

Here ΔV_{out} is the change in the voltage output of the P-mode of the control algorithm, which will eventually be added to the signal sent to the Z piezo. The change in signal is used instead of the actual signal so that the Z piezo maintains the current position, rather than returning to the equilibrium position [34]. V_{in} is a voltage proportional to the error signal, I_p is a constant that sets the initial values and K_p is a constant known as the proportional gain. By varying the value of K_p we can increase or decrease the rate of response to any changes in the system.

With proportional gain alone, the error will reduce but it will only reach zero in the ideal case of a uniformly flat planar surface.

The proportional gain feedback loop will adjust the tip position to one appropriate for the tip surface separation at the last point of measurement. Under experimental conditions there will always be some degree of sample tilt, so the next point of measurement will be either higher or lower than the previous. Eventually the degree of correction will be equal to the height change between pixels and the error will remain constant.

As the proportional gain is increased, the final value of the error signal decreases in magnitude, returning the system to a "steady state" faster. If the proportional gain is increased too high, it can lead to instabilities.

Integral mode

The next mode is called the integral mode and is given by the following equation:

$$\Delta V_{out} = K_I \int_0^t V_{in}(t')\mathrm{d}t' + I_I \tag{1.15}$$

Here K_I is the integral gain and I_I is a constant that sets the initial conditions. For a constant error signal (V_{in}), the V_{out} increases linearly with

a slope $V_{in}K_I$. The integral mode responds to changes more slowly than the proportional mode, but it is capable of reaching zero error. If the Integral gain is too high the system becomes oscillatory and at even higher values the whole system becomes unstable due to overshooting the target value by a sufficiently large amount that the error is greater in magnitude than it was before the correction was made.

Derivative mode

The final mode in this kind of feedback system is the derivative mode.

$$\Delta V_{out} = K_d \frac{\mathrm{d}V_{in}(t)}{\mathrm{d}t} + I_d \tag{1.16}$$

Here K_d is the derivative gain and I_d is a constant that sets the initial conditions. The derivative mode is often left out of feedback control for scanning probe applications (i.e. $K_d = 0$) as a small level of measurement noise can lead to a much larger noise in the error signal. This is due to the derivative of a step change being infinite.

Final notes on gains

One may think that it would be desirable to set the values for these gains as high as possible. Overly high gain values can however, lead to an over-correction, causing the system to oscillate around the set point. The value for V_{out} would become a decaying sinusoidal at first, which is acceptable, providing the oscillations have a short lifetime, but if the gains were increased further, the oscillations would have an increasing decay time until they reached the point where the feedback was responding to itself, and the error would continually increase, resulting in complete instability of the system.

Ideally gains should be as high as possible without triggering any oscillatory behaviour with a lifetime longer than the time taken for each pixel of

data acquisition, in order to maximise image quality, and maintain image independence from scanning direction.

Chapter 2

STM Experimental Methods

2.1 Ambient vs ultra high vacuum

All of the STM experiments performed within this thesis were undertaken using a system which operates with the sample under ambient conditions. There are many works within the literature that examine similar interactions where the sample is held under vacuum. Here we look at the advantages and disadvantages associated with each of these two different approaches to STM experimental set-ups.

2.1.1 Ultra high vacuum

Ultra high vacuum conditions (UHV, 10^{-8} mbar to 10^{-12} mbar [35]) simplify the conditions within a scanning probe imaging experiment. UHV conditions ensure the sample stays clean, tips and samples are much more stable than in ambient conditions due to lack of oxidation. There are no sudden air currents, such as can be generated from people opening lab doors, or air conditioning systems. Samples can be prepared *in-situ* preventing any contamination of the surface.

UHV also allows for the option to use cryogenics for extreme low tem-

perature experiments, as removing thermal energy from the system reduces drift.

Molecule deposition within UHV systems has traditionally consisted of the powdered form of the molecule loaded within a Knudsen effusion cell, which is heated until the molecules have sufficient energy to sublime. An aperture on the Knudsen cell limits the path of the sublimed molecules so they may only progress towards the sample surface [36]. More recently other methods have been under development, such as electrospray deposition [37] which is starting to allow a greater range of molecules to be studied under UHV.

There are several problems associated with UHV. Long load times mean it can take many hours to change the sample or tip, due to the need for pumping. Experimental set up can be tricky as there are only certain places cables can enter the system. Many organic compounds cannot be studied on surfaces due to their high volatility at the low pressures used in UHV. They are also much more expensive than their ambient counterparts.

UHV experiments are mostly used to gain a basic understanding of an experiment, or to perform highly detailed measurements, however the data they obtain is not necessarily of the same state your sample will be in at conditions appropriate for any applications. For molecules of biological significance the UHV environment is drastically different to the conditions in which the molecule is normally found.

2.1.2 Ambient conditions

Despite the many advantages of UHV conditions, there is much work being performed using ambient STM systems. The main advantage of operating in ambient, is the fact that anything that is observed is relatively stable in the conditions typical of those conditions that commercial technology is expected to be capable of operation in.

Ambient STM has a much higher throughput of samples, as a sample and/or tip can be changed on the timescale of minutes rather than hours. With an ambient STM, a loose cable can be replaced without the need to dismantle the entire system. Ambient STMs are also much cheaper than their UHV counterparts due to the lack of expensive pumps and stainless steel vacuum chambers.

Ambient conditions are presently the only way of being able to conduct STM studies into the interaction with surfaces of organic molecules too delicate for the sublimation based sample deposition methods required for UHV studies.

It is also possible to study the effects different solvents have on these structures (see section 5.5), although for non volatile solvents we are no longer scanning in air and have to resort to liquid STM (section 2.1.2).

Ambient STM does experience a much higher level of tip instabilities when compared to UHV, and as such the tip can change dramatically over a single scan. Some of the other disadvantages, such as dealing with local air currents, can be compensated for by use of acoustic dampening cupboards and other methods.

Liquid STM

A progression from the ambient STM technique, liquid STM has been developed to help study interactions at the solid-liquid interface. Liquid STM is of significant importance to biochemistry, where many of the biological structures of interest are only active in aqueous buffer solutions [38]. In biochemistry, liquid STM is a unique technique due to the ability to collect structural data of molecules in their natural chemical environments, unlike other techniques operating on this length scale which require UHV conditions (such as electron microscopy). Solvent selection is a very important step in the preparation for liquid STM experiments. The selected solvent

needs to have a low enough volatility for the time taken for evaporation of the solvent to be much longer than the time taken to gather data. Evaporation during an experiment can lead to scan instability, not to mention the effects a change in the concentration of any molecules in the solution could have on any formed structures. Solvents which do evaporate quickly are allowed to do so before scanning begins, returning us to the condition of scanning in air.

Additionally, the liquid must not be able to conduct electricity or contain ions otherwise there will be conduction through the solution, without the need for quantum mechanical tunnelling. It is also essential that the solvent molecule has a lower affinity for the substrate than the solute, otherwise all STM images will only contain the adsorbed solvent molecule, as it is present in much greater numbers than the solute. Examples of solvents which work well for use in liquid STM include nonanoic acid and phenyloctane [39]. It is much more common to encounter false approaches in liquid STM than other variants of the technique. This is where the tip interacts with one of the solvent molecules in such a way that results in a spike in tunnelling current and the automated tip approach system acts as if it has encountered the surface. After this current spike, the z piezo-drive fully extends but is unable to reach the tunnelling current and the approach has to be restarted. To avoid this it is required to set a higher "stop at" current in the approach settings, however this increases the likelihood that the tip will crash during an approach so generally much slower tip approach speeds are used with liquid STM.

During approach, once the tip breaks through the surface tension of the liquid it is very difficult to see how close it is to the solid substrate surface. The sample is left for over 10 minutes for temperature equilibration before continuing with the automated fine approach. As such, approaching the tip takes much longer when operating in liquids than compared to operating in air. Nonetheless the sample load times are still significantly faster than the load times for UHV studies.

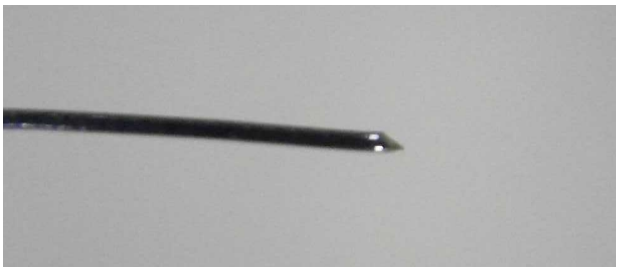

Figure 2.1: **Pt/Ir stm tip:** A freshly cut 0.25mm Pt80/Ir20 wire tip for use in ambient STM

2.2 Probes

Probes are typically made of electrochemically etched tungsten (W), common in ultra high vacuum systems (UHV), or tips cut from an alloy of platinum and iridium (ambient STM) [38, 40].

For ambient and liquid STM systems tips made from freshly cut platinum-iridium alloyed wire are used. The high level of chemical stability of this alloy make it ideal where oxygen is present, or in mildly acidic solutions. Preparation of Pt-Ir tips takes a very short time as one need only clip the end of the wire at an angle to form a sufficiently sharp tip [9]. In UHV systems, where oxidation is not a factor, tungsten is used because it is easy to electrochemically etch into a sharp point and relatively inexpensive compared to Pt-Ir wire.

2.3 Scanning process

The scanning unit for the STM, which contains the scan head, tip, and sample plate, is positioned on a large mass block (such as steel, wood or marble) which in turn is suspended from the ceiling of an acoustic impedance cabinet by a series of bungee cords. This is in order to minimise vibrations, which (due to the exponential dependence of tunnelling current on the tip/sample separation) can cause strong noise. Once a sample has been prepared it is loaded onto the sample plate. A freshly cut Pt/Ir tip is loaded and the sample positioning screws are adjusted until the tip as close to the surface

Figure 2.2: The head unit and sample holder

as visibly possible.

The sample plate has several key features marked in figure 2.3. The pcb connector marked 'a' is where the sample plate electronics connect to the rest of the STM. The metal bar marked 'b' is threaded onto the screw that can be seen at its centre. This screw goes all the way through the sample plate, passing through contacts for the electronics, with a spring between the large metallic base plate and the screw head. This screw can be pressed to raise the metal bar 'b', with the spring returning the bar to the initial position with sufficient force to maintain good contact with 'c'. Clip 'c' is the sample contact clip through which the bias voltage is applied to the sample. Care must be taken when positioning this clip in the case of substrates consisting of a thin metallic film on an insulator, in order to avoid scratches which can break the circuit prematurely. The actual sample is marked 'd'. In figure 2.3 the sample is a HOPG block. Finally, 'e' is a glass cover-slip to insulate the sample from the main support plate.

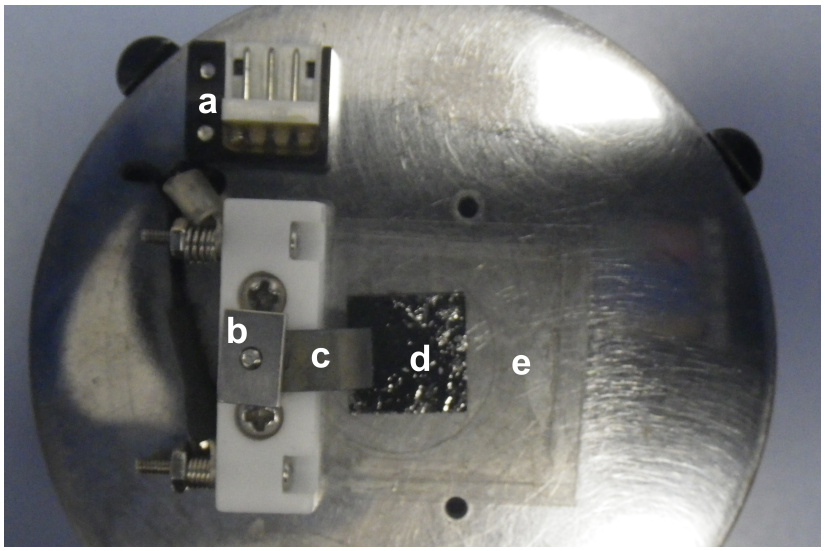

Figure 2.3: The sample plate for the Picoplus STM featuring a)electronics connector, b) clip securing plate, c) sample contact clip, d) the actual sample, and e) a glass slide

The ideal position for the sample, is such that the front (manual approach) legs are equal in height (left to right) and marginally shorter than the rear (automatic approach) leg. This is so that when the software approaches by adjusting the rear leg, it will result in the sample being approximately level once scanning begins. At this point the current reading on the front of the scan head unit should be 0.00. If this number is reading an actual current, the tip has crashed and will need to be replaced.

The set point, bias voltage and gains are set to the desired values. Typical values for the gains are between 1 and 5. The values for the set point and bias voltages are dependent on the sample to be scanned. As the theory in Chapter 1 shows, a high set point leads to the tip scanning closer to the sample than a low one, and increases the risk of the tip crashing, or sweeping aside molecules, but provides a higher signal to noise ratio than a lower set point. The bias voltage sets the minimum energy required for states to contribute to the final image. Typical set points are 1 nA for plain HOPG and 0.05 nA for molecules on a surface. Bias voltages vary between 0.1 V and 1.5 V

The scan location is centred within the piezo range before approach at a value between 1% and 10% of the maximum motor speed (the maximum

speed of the motor is 400μm per minute). The drift settles somewhat during the approach.

The tip quality is initially compared by examining the trace and retrace. If they are drastically different, the sample is withdrawn and the tip replaced. If they are fairly similar a feature such as a step edge or adsorbate is searched for. If the step edges are crisp and clear then the tip is probably sharp enough to see molecules (often molecules will have already been seen by this step). The initial scan area is typically 200 x 200 nm, 150 x 150 nm or 100 x 100 nm. Next the scan size is adjusted to one appropriate for the molecules that have been deposited on the surface, typically between 100 x 100 nm and 30 x 30 nm, with smaller scan sizes used for obtaining fine structure detail, and larger scans to determine long range order and molecular interactions. Several different areas of the sample within the piezo range are scanned, and further adjustments to gains, set points and bias can be made to optimise the contrast within the image. There are no precise values that will work every time due to the unknown nature of the exact tip state. Minor improvement to the tip can be achieved with a series of incrementally increasing voltage pulses (starting around 1.0 V and gradually increasing to as high as 2.0 V), however this also has the chance to make the tip worse and is a risky strategy to rely on, but it can be worth it if a tip is about to be changed. Larger voltage pulses will change the tip more dramatically than smaller ones, so it might be worth attempting several smaller pulses before increasing the magnitude of the pulse voltage.

2.4 Drift compensation

2.4.1 What causes tip/sample drift?

"Drift" is the name given to the distortion in scanning probe images caused by the undesired relative motion of the sample with respect to the probe. This motion arises from the differences in rates of thermal expansion for the

various materials involved, their response to local temperature fluctuations across the lab and ceramic creep. These temperature fluctuations arise from the flow of air currents around the lab in addition to any heat generated by the STM during operation (resistive heating of wires, inelasticity of piezo expansion/contraction etc.)

2.4.2 Correction methods

There are two main types of drift correction, those requiring prior knowledge of the surface structure (useful for identifying preference of two known structures) and those that rely on no prior knowledge of the structure (bond lengths and angles in newly identified structures).

For known structures it is possible to overlay a simulated image of the known structure and distort the data image until it matches the known structural model. This can also be done on images with partial coverage, such as scans on highly oriented pyrolytic graphite (HOPG) where the exposed graphite lattice can be used for calibration. This was the method used in the studies of TBPB performed in chapter 6.

For unknown structures there are multiple different methods. The simplest involves measuring the drift over a sequence of images and distorting the image data to compensate.

2.4.3 Drift estimate correction method

For this method, which is based on one discussed by Yurov and Klimov [41], it is required to have set of at least 4 subsequent scans in alternating scan directions. The drift needs to be relatively linear. This assumes that X is the fast scan direction and Y is the slow scan direction.

To calculate the drift vector for the data contained in the second image of the sequence (image 2), a measurement of the drift is needed between

the first and third images of the set. A distinct feature present within both images is selected and the X and Y pixel locations of the feature within the image are measured. The vector between these two points is the total drift over the time taken for two full scans. The magnitude of this vector needs to be halved in order to calculate the drift that took place during the acquisition of the data for the second single scan. This gives us a measure for the drift during the creation of image 2.

Tip drift will appear to either compress or stretch the features in the image in the Y (slow scan) direction, so the opposite process needs to be applied to compensate. If the y component of the drift is in the same direction as the slow scan direction, then the same scan area will contribute more than once to the data image. In an example where the tip is scanning from the bottom to the top of the selected area, as the tip moves up, the sample will also drift up leading to some of the same area being imaged again. This results in an image made from data collected over a smaller area than intended and results in the features in the image to appear stretched. In our example we will require the whole image to be compressed until the image area corresponds to the real area over which that data was collected.

In an example where the drift vector is opposed to the slow scan direction, if the tip is scanning from the top to the bottom of the selected area, as the tip moves down, the sample will drift up leading to areas of the image being skipped. This results in an image made from data collected over a larger area than intended and results in the features in the image to appear compressed. In the compressed example we will require the whole image to be stretched until the image area corresponds to the real area over which that data was collected. The effect of the alignment of the y component of the drift vector is further explained in Figure 2.4

For an image where the drift vector is opposed to the slow scan direction, the Y scaling factor (S_f) is

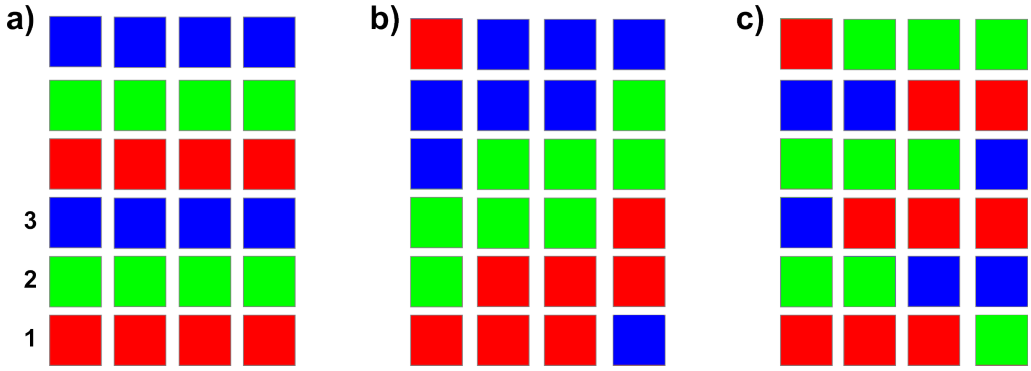

Figure 2.4: **Drift vector direction effects for a periodic sample with ridges of three different heights (labelled red, green and blue)**. If a) shows the expected image for drift free data acquisition over a specified area, then b) and c) show the resultant images, scanned from bottom to top and left to right, for the case where the drift vector and scan direction are aligned, and opposed respectively. In this case the $Drift_y$ is comparable to the slow scan speed. In b), as the scan tip has moved up, the sample has also moved up causing some of the area from a) line 1 to be scanned again in image b) line 2 and so on. In c), as the scan tip has moved up, the sample has moved down causing some of the area from area line 3 to be scanned into image line 2.

$$S_f = (S_0 + Drift_y)/S_0 \tag{2.1}$$

where S_0 is the y length of the area claimed to be scanned.

For an image where the drift vector is aligned with the slow scan direction, the Y scaling factor is:

$$S_f = (S_0 - Drift_y)/S_0 \tag{2.2}$$

In each case the whole scan is then scaled in the Y direction by the scale factor. The distances in y, in nm represented by each pixel remain the same as claimed by the original image.

In the fast scan direction it is assumed that drift will have a negligible stretching effect on each line, however the position of each line is shifted slightly. This is compensated for by skewing the image. The skew angle

(using trigonometry) is given by

$$Drift_x/S_0 = tan\theta \tag{2.3}$$

Repeat for image 3 of the set, using image 2 and image 4 to calculate the drift vector.

To confirm that drift has been correctly removed, it is possible to overlay the two corrected images (image 2 and image 3), with the top layer partially transparent, so that the structures line up with each other.

2.4.4 Limitation of this method of drift correction

This method for drift correction makes several assumptions which may cause errors in the final measured values of angles and distances. Firstly, it is assumed that drift is both linear and constant over the sequence of 3 scans. In reality drift is often non linear as typically the expansions that cause the drift slow down as the temperature difference that created them becomes smaller as the two bodies reach equilibrium. The direction of the drift can also deviate over the course of a scan and may lead to additional distortions. Secondly this method assumes that the drift in the Y direction is much smaller than the scan speed in the Y direction. This is why we have merely divided the drift vector by 2 to calculate the drift value over 1 scan, rather than calculating the fraction of the image scanned before the feature we are using to measure the drift (in the first image), and after it (in the third image), and adding 1 for the complete scan in between them. In order to calculate this properly it would be required for the scan direction to be known (which is not always the case), and if the drift is small then assuming the two partial scans total to a complete one does not affect the end result much.

The third approximation concerns the drift in the X direction. By applying a skew to compensate for X drift, we are assuming that because scanning in the X direction is much faster than the Y direction, the stretch along an individual linescan of the X axis is negligible. As there is still some drift in X, we have applied all the drift which occurred over each line at the end of the line, resulting in each line of the scan being shifted relative to each other by a small amount. As we are able to get two corrected images to overlay each other with a high degree of accuracy, we can see that these assumptions make good approximations.

Chapter 3

STM Substrates and Other Experimental Methods

3.1 Substrates

All experiments discussed in this thesis utilise one of the following substrates: highly oriented pyrolytic graphite (HOPG), Au(111) on mica, or graphene on polycrystalline copper. Substrate selection is important, as the molecule to be imaged needs an interaction with the surface within a certain energy range. Too weak an adsorbate-substrate interaction will lead to a high mobility of the molecule, causing high-resolution STM imaging to become impossible as the motion of the molecules can lead to a smearing out of the image. Too strong an adsorbate-substrate interaction prevents desorption required for error correction, resulting in a higher number of defects and smaller crystallite size of the formed crystal domains [42]. Desorption is the process where a molecule can leave the surface and go back into solution, allowing it to rebind later in a different position.

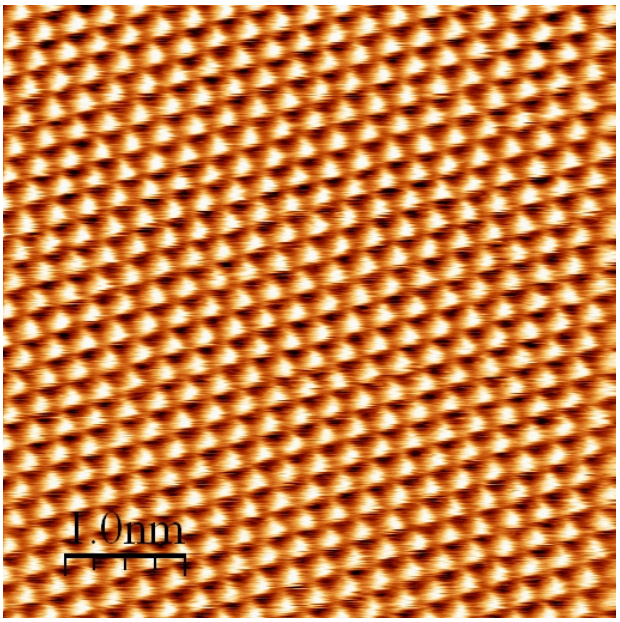

Figure 3.1: A 5 nm x 5 nm STM image obtained of a freshly cleaved HOPG surface imaged in air. The hexagonal carbon structure can be seen in triangular form due to the atoms in the second layer being centered under spaces in the hexagons. This image was taken with a tunnel current of 1 nA and a tip bias voltage of 0.075 V

3.1.1 HOPG

Highly oriented pyrolytic graphite (HOPG) consists of layers of two-dimensional sp^2 hybridised carbon sheets stacked on top of each other by Van der Waals and π-stacking interactions. The graphite blocks have been annealed at high temperatures ($>$ 3400 K) under a mechanical stress to improve the rotational alignment of the sheets (minimising layer mismatch) [43]. The separation of the nearest neighbour carbon atoms is 0.142 nm [44] and the plane separation is 0.335 nm [45]. Graphite blocks, 10 mm x 10 mm, with a *mosaic spread* of $3.5° \pm 1.5°$ were purchased from Agar Scientific.

The *mosaic spread* is used as an indication of the quality of the orientation of planes within a graphite block and the lower this angle the better. The term 'mosaic spread' comes from X-ray diffraction studies of HOPG. HOPG is an example of a mosaic crystal, that is, a structure consisting of many micro-crystallites which are oriented almost, but not exactly, parallel to one another [46]. Mosaic spread is a measure of how far a HOPG block deviates from a perfect crystal and is quantified in the terms of the full width at half maximum (FWHM) of Bragg diffraction profiles obtained

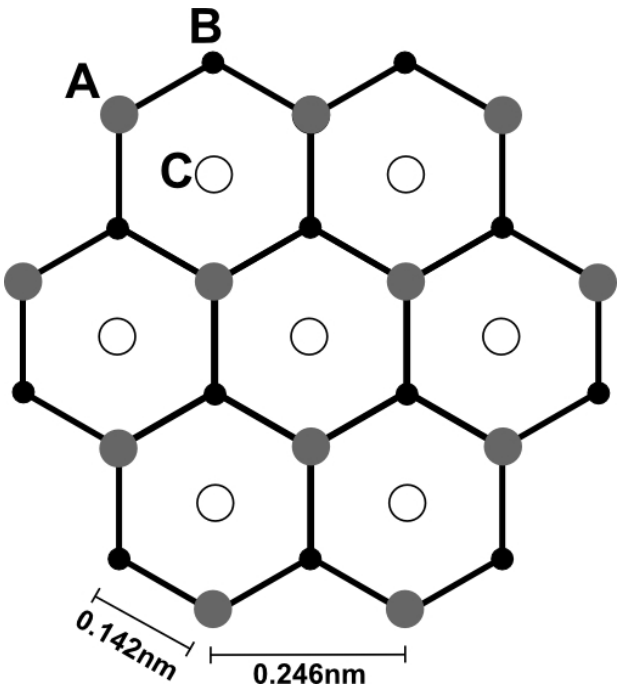

Figure 3.2: **Graphite Lattice** Atoms at sites marked 'A' are 10 pm higher than atoms marked 'B'. Site 'C' has a vacancy corresponding to the position where the higher atoms, in the second layer below the surface, lie. Due to this, the atoms in position B on the top layer, lie above a vacancy in the layer below. Adapted from [44]

from X-ray diffraction studies.

For use as an STM sample substrate the restrictions on mosaic spread are not as constrained as they are for HOPG used in X-ray diffraction, as it is only the top complete layer that is being used. Mismatches are more likely to exist close to step edges so generally avoiding such areas is advised.

The neighbouring atoms in the unit cell of graphite are inequivalent [47], with a minor buckling of the aromatic rings causing a difference in relative heights of 10 pm between the atoms. Figure 3.2 shows a top down view of the graphite lattice illustrating this atom inequivalency. Atoms at sites marked 'A' are 10 pm higher than atoms marked 'B' due to there being an atom from the subsequent layer directly below the site A atom. The site B atom has a vacancy directly below it. Site C has a vacancy corresponding to the position where the higher atoms, in the second layer below the surface, lie. Figure 3.1 shows the HOPG structure visible by STM, which has a triangular symmetry, whereas the atomic structure of the graphene sheets in a graphite block are hexagonal.

There are two contributions generally accepted as to the cause of the triangular appearance. One, is a consequence of Bernal/A-B stacking, which is commonly observed in graphite [48]. Bernal stacking can be summarised as a relative lateral shift between the graphene planes in neighbouring layers that make up the bulk graphite, as shown in figure 3.3 and by the position of site C in figure 3.2. This shift positions the raised atoms of the second layer into site C.

This carbon site asymmetry results in a triangular shape in the electronic π-bands [18] above and below the carbon atoms. It is predominantly the π-bands that contribute to the STM images of graphite. One would expect that the 'A' site atoms would be the main contributors to the triangular STM images of HOPG, due to the 'A' site atoms being higher than the 'B' site atoms, however due to interlayer interactions, there is a higher density of π electron states near the Fermi level above the site 'B' atoms relative to the site 'A' atoms [49].

There is still some controversy in the interpretation of the origins of the observed structures in STM images. Some authors [50] claim that the triangular reconstruction, although the most commonly observed contrast experimentally, may be due to anisotropy in the tip. Padres *et al* claim that the much rarer imaging of a hexagonal structure is observed when the mechanical interaction of the tip is sliding the top layer of graphite relative to the second layer, which removes the A-B site inequivalency [49]. Mizes *et al* showed how most of the observed structures of HOPG can be simulated by the combination of 3 sine waves, with the size of the phase shift between them giving rise to the various different observations, which they propose is caused by tip anisotropy [50]. Most authors agree that the difference in observations are due to imaging artefacts and not due to different surface morphologies.

The image shown in figure 3.1 shows our experimental data matching the form predicted by Selloni et al [18].

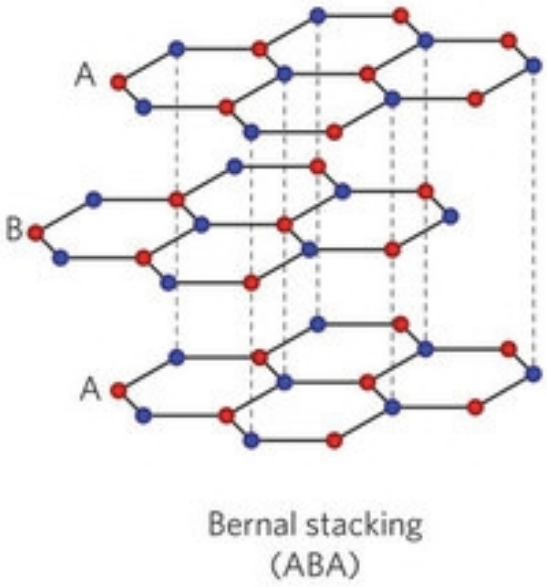

Figure 3.3: **A-B/Bernal Stacking** The offset of the carbon sheets results in an atom being occupying the central vacancy in each hexagon. The distance between nearest neighbour red and blue atoms in a sheet is 0.142 nm [44]. Adapted from [51]

HOPG summary

HOPG has the advantage of being a relatively cheap, easy to prepare, low noise substrate. Due to the high strength of the carbon-carbon bonding, there are no mobile substrate adatoms to worry about during scanning. As the inter-layer stacking interaction is so much weaker than the bonding holding each individual layer together, steps tend to be very large and flat. HOPG has high thermal and chemical stability, which allows for use under various temperatures and solvents and lacks any catalytic activity which might prevent usage in certain experiments.

3.1.2 Au(111)

The gold substrates used consist of a 100 nm thin film of Au(111) on mica purchased from Georg Albert [52]. The mica backing allows us to use a thinner film of gold while maintaining a rigid mechanical support. The Au(111) on mica is stored under a pressurised nitrogen atmosphere until required for use in order to minimise surface contamination. The (111) face

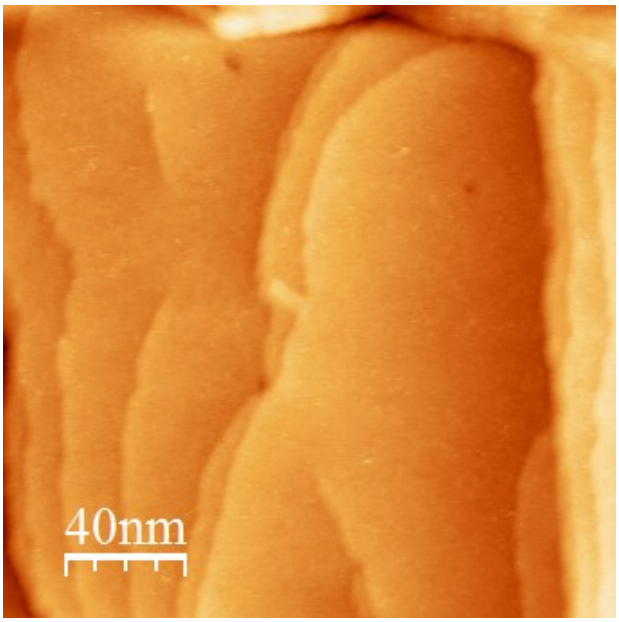

Figure 3.4: This is a 200 nm x 200 nm STM image obtained of the Au(111) surface after cleaning but prior to any molecular deposition

of gold is sufficiently flat for molecular deposition STM studies, as can be seen in Figure 3.4.

Prior to molecular deposition the gold sample was stored under a pressurised nitrogen atmosphere to protect it from dust and adsorption of molecules from the air in the lab. Surface preparation was performed in one of either two ways: plasma cleaning or flame annealing. For plasma cleaning, the sample is heated to a temperature of 100 °C. Once this temperature is reached, an oxygen plasma, sustained by microwave radiation, is applied for 12 seconds. For flame annealing the sample is held under a hot butane flame until a faint orange glow appears for several seconds. If the glow is too bright the sample can be degraded. An over anneal can be seen by the shiny surface of the gold "misting up" in which case the substrate would be discarded. Out of the two techniques the plasma cleaning shows less variation but takes much longer (as the plasma cleaner requires time to heat up).

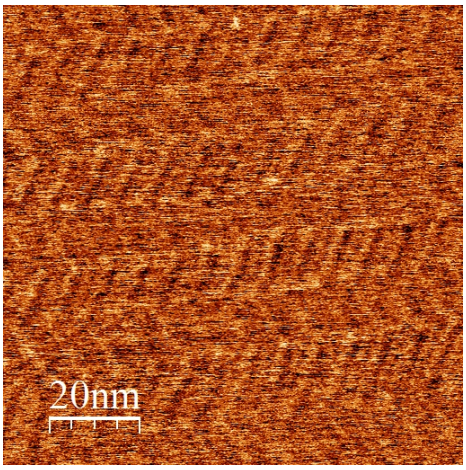

(a) Experimental Image

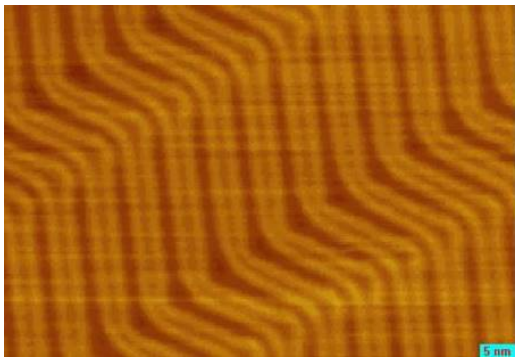

(b) Textbook herringbone [55]

Figure 3.5: On the left is a 100 nm x 100 nm STM image of the Au(111) surface after flame annealing showing the zig zag lines of the herring-bone reconstruction as obtained using our equipment. On the right we have a textbook image of the same reconstruction. [55]

Herringbone reconstruction of Au(111)

After annealing, the gold surface forms what is known in the literature as a *herringbone* surface reconstruction. This appears as a periodic arrangement of zigzagged lines with a 120° angle at the changes of direction (known as 'elbows' in the literature) occurring on average every 25nm [53]. Gold is the only known metal with a face-centred-cubic crystal structure, that undergoes a surface reconstruction along the (111) plane [54].

The atoms in the bulk of the gold align in a face-centered cubic (FCC) packing configuration. At the surface there are regions where 23 atoms in the surface layer pack into 22 bulk lattice sites [56], resulting in a 4.2% contraction in the $[1\bar{1}0]$ direction [57]. This row of 23 atoms can be considered a 22 x $\sqrt{3}$ rectangular unit cell superlattice on the bulk gold [58], with the first and 23rd atoms in their normal bulk state positions (so the 23rd atom is the same as the first), and the others form a compressed line in between them. The stress caused by attempting to fit 23 atoms into 22 lattice sites, results in a realignment in the middle of this row of 23 atoms, where the packing arrangement shifts from FCC (ABC stacking), to hexagonal close packed (HCP) (AB stacking, as seen in HOPG as discussed earlier in sec-

tion 3.1.1) in order to accommodate the additional atom. At the transition between the FCC and HCP configurations, atoms are able to move upwards with respect to the surface plane, in order to alleviate the stress within the surface. This upward shift of 20 ± 5 pm [53] occurs at the same position in every group of 23 surface atoms and is what results in the observed bright lines of the herringbone reconstruction and explains why they are always found in pairs, one for either side of the HCP region. The ratio of the widths of the domains of FCC and HCP packing are not equal, the HCP domain is 0.5 times as wide as the FCC domain [57]. These bright lines lie perpendicular to the compression direction and exist in 3 rotational domains separated by 120°. These raised lines are even visible though monolayers of adsorbed molecules (as seen later in Figure 6.9 in Chapter 6). The elbows of the herringbone reconstruction are known nucleation sites for adsorbed materials [56]

The herringbone reconstruction has been observed through many complementary techniques, including low energy electron diffraction (LEED) [59], resonance high energy electron diffraction (RHEED) [60], transmission electron microscopy (TEM) [61] and helium atom scattering (HAS) [58], in addition to STM. The use of complementary techniques confirms that this is a real structure and not just an STM imaging artefact.

A detailed study of the Au(111) surface was performed by Barth *et al* [53] and more information can be found in their work.

3.1.3 Graphene on copper

Graphene is a popular substrate in the scientific literature at the time of writing. In the three year period between 2009 and 2012 there were over forty thousand journal articles published containing the word 'graphene' [62]. There are many reasons why graphene is such a heavily researched material, but as for use as an STM substrate, it is the high charge carrier mobility μ, measured to be over 10,000 $\mathrm{cm^2V^{-1}s^{-1}}$ at 300 K [63], and the

zero-band gap in the electronic structure [64], which make it interesting. The micro/nano electronics industry has been making major developments towards including graphene in many new experimental devices, and due to recent developments in graphene transfer, it can be used on many different materials. There are still many thing about graphene that are not fully understood which are relevant for many potential applications. Sensor applications require a good understanding of the adsorption mechanics of various different molecules [65] and much current research is examining this further.

Graphite is formed of stacked graphene monolayers. A-B/Bernal stacking of these graphene layers results in an in-equivalence of sub surface atoms in the graphite bulk, causing bulk graphite to lose many of the properties that make monolayer graphene so interesting, such as the transition from a zero-band-gap semiconductor (graphene) to a semi-metal (graphite) [66]. However graphene is structurally similar enough to graphite for experiments that work on HOPG to be likely to also work on graphene. The importance here is to understand any differences in results between graphene and HOPG.

Graphene on copper was selected as a substrate for several reasons. Firstly, copper is the metal upon which single layer graphene has been reliably grown as monolayer [67] and is commercially available. Graphene films from Graphene Laboratories Inc. were used in the experiments in section 5.3. As there is no need for the transfer of the graphene film, we do not risk adding any additional defects which may be caused by such a process.

Some preliminary experiments with bare copper showed that the reactivity of copper in solutions of nonanoic acid could prove to be a problem. The copper surface oxidised, turned green, due to the formation of the copper (II) oxidation state, after only a few hours so that scanning is not possible, as the surface is not stable.

There exists in the literature evidence of copper surfaces being stabilized from chemical attack by coating with few layer graphene [68], which indicated that STM experiments involving carboxylic acid solvents may still be possible.

The graphene coating did not stop the oxidation completely, but it did slow it down to a rate where imaging the molecule was possible. The sample would usually be usable for several hours of scanning.

The copper foil upon which the graphene is grown is quite thin (20μm). The delicate nature of the foil necessitates great care during handling. The malleability of the foil can lead to a slight folding, or bending, especially around the edges, if due care is not taken when cutting the foil to size, or when loading the sample into the sample plate. Any creases or ridges in the foil can pose problems during scanning due to the large height variations the tip will experience.

3.2 Atomic force microscopy

Atomic force microscopy (AFM) is another scanning probe technique which is used to analyse samples on the nanometre scale. It is similar to the STM disussed in Chapter 1, in that it consists of an atomically sharp tip moved by a piezoelectric drive and operates using a similar feedback loop. The major difference is in the way that the signal the images are created from is obtained. Rather than using a voltage bias on the tip to generate a signal, the AFM has a tip on the end of a flexible cantilever. The simplest mode of AFM to explain is contact mode AFM. When the tip is brought close to the surface it initially experiences an attractive force due to van der Waals interactions. However, once it is brought even closer it will start to experience a stronger repulsive force due to the Pauli exclusion principle that no two electrons may occupy the same quantum state. This interaction is described by the Lennard-Jones potential (Figure 3.6). These forces cause

a deflection in the cantilever, which is measured by reflecting a laser off a mirrored coating on the back of the cantilever onto a segmented solid state photodetector. The laser is initially aligned so that the laser spot is split equally between the segments of the detector, and any deflection of the spot results in a difference in voltage between the different segments of the detector. This is used as the signal for image formation and feedback control. By knowing the stiffness of the cantilever, an accurate measurement of the height of the deflection can be obtained. AFM as a technique is capable of detecting forces as small as 10^{-13} N [5].

In tapping mode AFM (also known as AC mode or intermittent contact mode), the type used in the work in Chapter 7, this cantilever is oscillated at close to the resonant frequency. Tapping mode is preferential to the simpler contact mode as there is less chance of damaging the tip. The interaction with the surface potential shifts the amplitude of these oscillations and it is the change in amplitude which is measured and used to form the images. Images can also be constructed from the phase shift between the driving oscillation and the actual oscillations, making these images more sensitive when there is a sudden change in surface height. For our experiments we use a driving frequency 5% below the resonant frequency in order to be on the steepest linear part of the frequency curve (Figure 3.8). This allows us the greatest frequency shift for the smallest height difference and is crucial to obtaining optimal resolution.

Under ambient conditions AFM has the advantage over STM in that it can look at insulating samples, wheras STM can not, however the ambient AFM systems can not reach as good a spatial resolution as the STM and cannot examine unoccupied states. As a technique AFM ultimately can reach as good (if not better) spatial resolution as STM by using cryogenics, UHV and a further variant called Q+ AFM (which will not be discussed here) and can be seen in the famous image of pentacene by the IBM research lab [69].

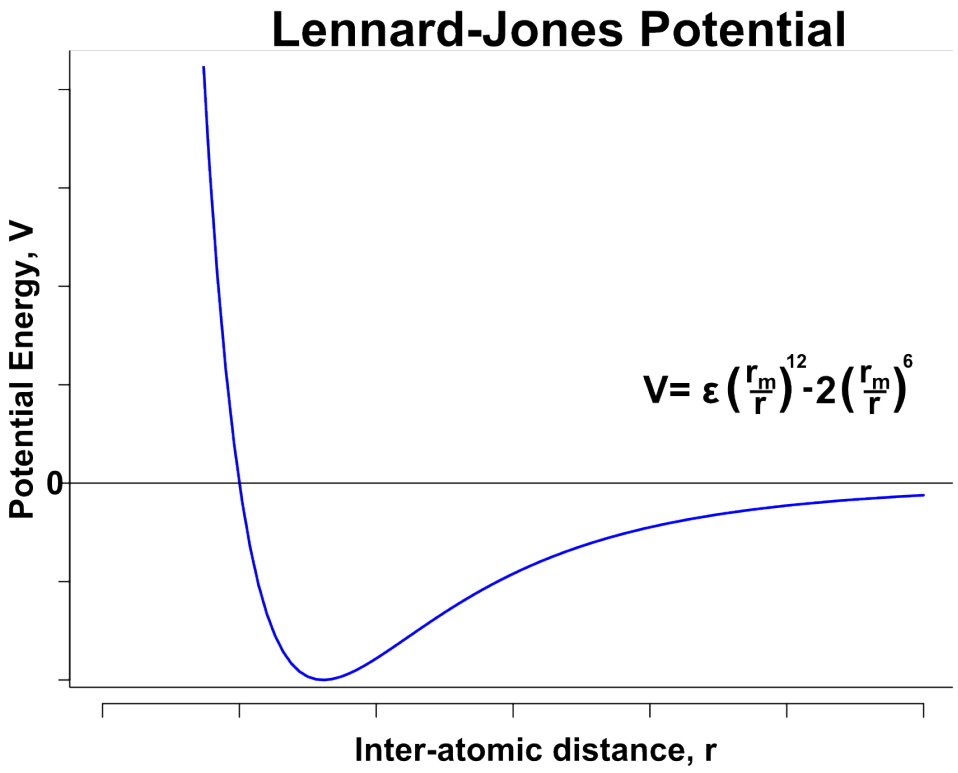

Figure 3.6: The Lennard-Jones potential energy curve, where r is the inter atomic distance, ϵ is the depth of the potential well (the bonding energy), and r_m is inter atomic distance at which the potential reaches a minimum.

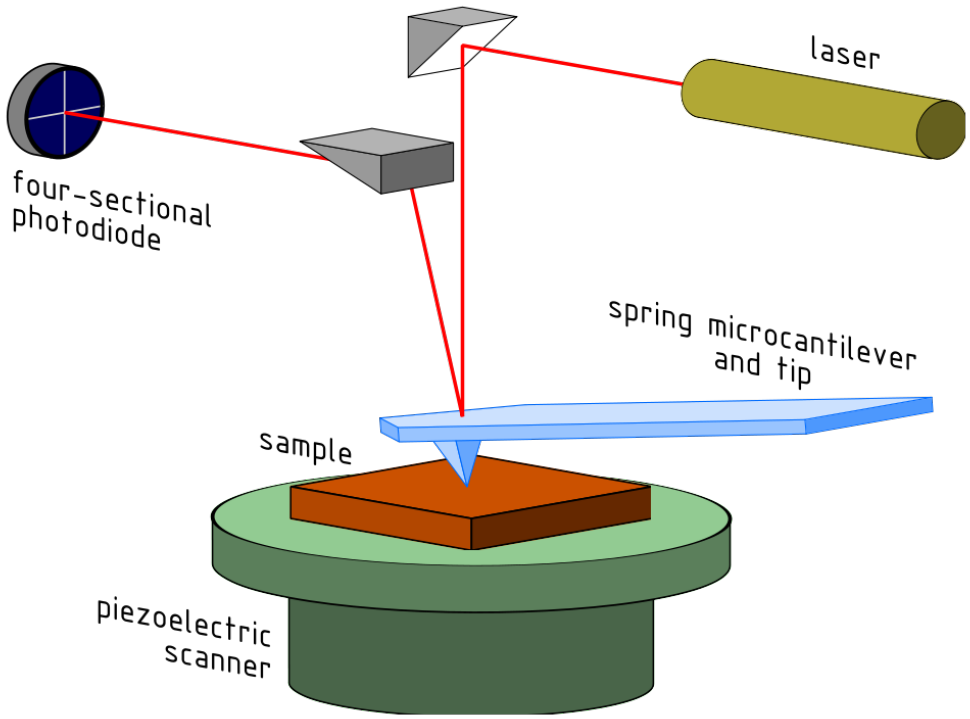

Figure 3.7: The schematic of a typical ambient AFM, showing how reflection of a laser is used to detect deflections of the cantilever. In AFM, the piezodrive typically moves the sample rather than the tip. Image from wikimedia commons

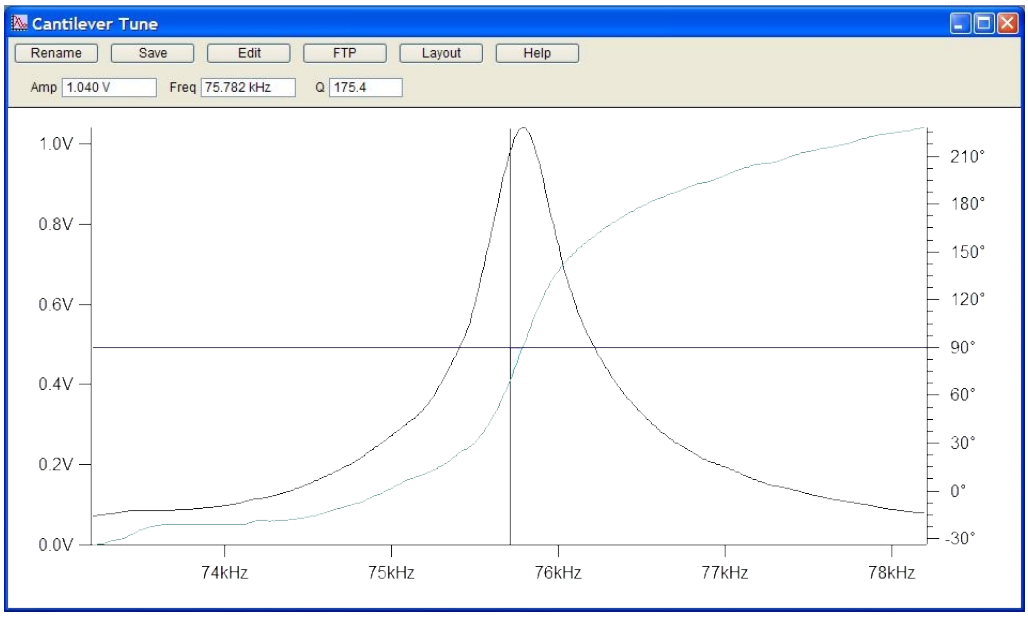

Figure 3.8: **AFM cantilever calibration:** here a typical afm cantilever has been tuned to 75.782 kHz, which is 5% below the resonant frequency. The vertical black line indicates where the chosen driving frequency lies on a curve of frequency vs displacement (converted into voltage difference on the photo-diode). Note the steep linearity of this section of the curve.

Chapter 4

Self Assembly and Molecular Networks

4.1 Introduction to molecular self assembly

Molecular self assembly is the process in which specially designed molecular units naturally fit together to form specific structures in a way that duplicates the methods found in nature [70]. The elements involved in many of these processes are the same elements featured in most compounds found in nature: carbon, hydrogen, nitrogen and oxygen [71]. Self assembly is the preferred method for the production of novel new materials for lubrication, organic electronic devices, electrochemistry applications, nanoscale patterning and even designer proteins [42]. The structures that can be formed exist in one dimension (chain polymerization), two dimensions (as discussed later in this chapter) or three dimensions (such as protein folding).

This thesis focuses exclusively on two dimensional structures on a surface. The two dimensional case has been chosen for several reasons. Two dimensional systems are much less complex than three dimensional ones when it comes to modelling. Current nano-fabrication methods in industry (such as for computer chip patterning) use layer by layer processing tech-

niques to build a three dimensional structure out of a series of 2 dimensional layers. However the main reason is compatibility with scanning probe techniques such as STM, which allows for a greater level of characterization of the structure.

4.1.1 Molecular networks: Introduction

Two dimensional molecular networks, often called self assembled monolayers (SAMs) within the literature, are a type of molecular crystal which can be formed on atomically flat surfaces. Silinsh and Čápek define molecular crystals as "a specific kind of solids formed by electrically neutral molecules or atoms, which interact with nonbonding, relatively weak interaction forces" and give van der Waals interactions and hydrogen bonding as examples of these forces [72]. Van der Waals interactions include the attractive force between two permanent electric dipoles, the attractive force between a permanent dipole and an induced dipole, and the attractive force between two induced dipoles (London dispersion forces) [7]. Molecular networks have been developed using various types of bonding between monomers, with hydrogen bonding, metal co-ordination, and full covalent bonding all investigated. There was also some work by Saywell *et al* [73] which demonstrated molecular centres could be positioned relative to each other by utilising the van der Waals interactions between interdigitating alkane side chains.

A typical example of a self assembled monolayer (SAM) is that of alkylthiols (organic chain molecules terminated with a S−H group) on gold [74–76], which form large scale ordered crystallites with a periodicity of 0.5 nm [74]. The alkane chains can be easily functionalised for specific purposes, yet their proximity to one another can lead to interactions between the alkane chains of adjacent molecules. Control of the spacing of the thiolates is needed in order to open up a wider range of applications, which leads us onto the field of nano-porous networks as templates.

Applications for such molecular networks include the formation of nanoporous

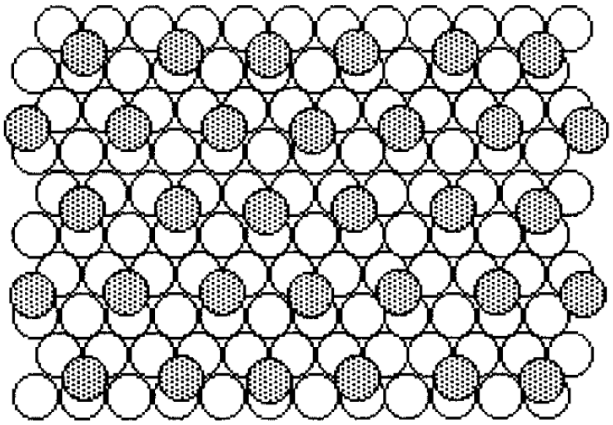

Figure 4.1: Hexagonal coverage scheme for alkanethiolates on Au(111). The open circles are gold atoms and the shaded circles are sulphur atoms. Adapted from [75]

solids, and clathrates, which are "inclusion compounds in which the guest molecule is in a cage formed by the host molecule or by a lattice of host molecules" [7]. These have potential uses in hydrogen or ion storage, or uses as molecular sieves and filters. Many of the experiments to demonstrate the capacity of these pores for templating applications use adsorption of fullerene (C_{60}) molecules to fill the pores [77]. There is also development working towards chemical sensor chips, where an array of pores can be functionalised to bind to a specific molecule, changing the electrical properties of the surface when they bind (this would require fully conjugated covalent bonded systems). Another application of functionalised pores would be for catalysis, with every pore acting like the active site on an enzyme, tailored to a specific reaction. There are many other potential applications waiting to be realised but first we need to learn the nuances of designing the molecules to form these crystals and have a greater understanding of how they fit together. The field of *crystal engineering* is a well established and expanding field in chemistry, pharmacology, and nanoscale physics, which concerns itself with the design and characterisation of the molecular building blocks which come together to form these networks. Producing sufficient quantities of these designer molecules has prompted development of new pathways in organic synthesis.

Adsorption of molecules has been examined on multiple different sur-

faces including: HOPG, graphene, Au (multiple crystal faces), Cu(111) [78] and (100) [79], Ag, and Ag terminated silicon [80].

Interactions with the surface

There are two main ways a molecule can interact with a surface, chemisorption and physisorption [81]. Chemisorption involves the formation of a (covalent or ionic) chemical bond with the surface, a classic example of which is the bonding between thiol (S−H) terminated molecules, and gold, due to the strong interaction of sulphur atoms with the gold surface [76]. Physisorption involves weaker interactions such as van der Waals interactions. Any molecule will physisorb to a surface, if the temperature is low enough, but chemisorption requires specific substrate-molecule combinations. Chemisorption can significantly change the substrate surface properties which can increase options for applications different to those appropriate for the unmodified substrate [42]. Chemisorption is much more directional due to geometric restrictions on the formation of the covalent bond, with good orbital overlap required. The higher strength of the surface binding minimises the possibility of error correction during network formation. Physisorption lacks these strict directionality restrictions and the binding is much more uniform across the surface (for conducting surfaces). The lower strength of the interaction between a surface and physisorbed molecules causes the interactions between two physisorbates to dominate over the interaction with the surface. Once a molecule is physisorbed to the surface it can (if the temperature is high enough) diffuse freely laterally, which assists in the formation of large domains of adsorbates. The topography of the specific substrate may impose additional restrictions on surface diffusion, such as a preferential direction for diffusion along troughs and channels created by any surface reconstruction, or step edges preventing diffusion past them. Chemisorbed species are much less mobile on the surface as the chemical bond needs to be broken each time a molecule moves from one binding site to another, and in many cases the energy required to

break this bond is sufficient for sublimation of the molecule (particularly in UHV studies). All the interactions of molecules with surfaces within this work will be physisorption. More detail on chemisorption and physisorption can be found in the review by Venables [82].

The objectives of studying two-dimensional molecular self assembly are: to find out what shapes and patterns various molecules form on different surfaces under various conditions, how stable these structures are, and to gain an understanding of what is happening in such a way that we can tailor the design of future molecules to produce a desired structure. All of these further the knowledge applicable for crystal engineering.

4.1.2 Molecular network deposition techniques

There are several ways in which molecules can be deposited on a surface in such a way they will form a molecular network. Here we will only cover methods appropriate to sample preparation under ambient conditions (UHV conditions open up other options such as Knudsen cell evaporation and electrospray deposition). The simplest method is *drop casting*, merely pipetting a droplet of the solution onto the prepared substrate and allowing time for the molecules to organise. This can lead to multiple layers if there are too many molecules present for the available area of sample so it can be difficult to prepare exact monolayer coverage across the entire sample. A slight modification of the drop casting technique would be *spin coating*, where the the sample is affixed onto a spindle (often by suction) and rotated at high speed. Spin coating is widely used in industry for forming thin films (such as photoresists) a fraction of a micrometer thick and there have been several cases of spin coated films being studied by STM [83].

The next type of sample deposition to be discussed is the immersion technique. Immersion techniques, where the sample is entirely immersed into the solution, provide several advantages. There is a longer dwell time for the molecule, allowing time for error correction, and there are no con-

cerns about having insufficient molecules for complete coverage. The major drawback is the large amount of molecular solution required. For standard immersion, the immersion vessel is narrow, such as a test tube with internal diameter only slightly larger than the substrate is wide. The substrate is held under solution for a pre specified length of time before removal. Excess of volatile solvents can be left to evaporate and non volatile solvents can have the excess blown off with nitrogen gas. The problem is that immersing the substrate in the solution will contaminate the entire tube full of solution with anything that has been on the substrate. Although substrates are usually clean on the prepared surface side, they are often less clean on the back side. In a typical case the minimum amount of solution needed for an immersion will be of the scale of a few millilitres per sample, compared to drop casting which will typically use two orders of magnitude less. If the solute molecule is cheap then this is possible, but often STM studies will be using molecules specifically synthesised for the study and so are only available in small amounts or are very expensive. This makes the immersion method much less favourable.

There is also the technique developed by and named after Langmuir and Blodgett which deals with immersion in a slightly different way.

The Langmuir-Blodgett Technique

The Langmuir-Blodgett technique for the preparation of thin films is a specialised type of immersion technique for ambiphilic molecules (a molecule possessing both a hydrophobic and a hydrophilic end). This technique utilizes the smooth surface of water to prepare a monolayer. Full details will not be discussed here (as this technique was not used for the data presented within this thesis) but a basic outline is given to provide the reader with some basic knowledge of this technique as it occurs within related literature. Further reading on the Langmuir Blodgett technique can be found in their original papers [84–86] and in several books covering the technique and related research applications [87–90].

A clean trough is filled with ultra pure water and has two barriers, mounted on motors which allow them to be moved either together or apart. These barriers are partially submerged within the trough, preventing anything floating on the water passing them, but still allowing water to flow underneath them. The surface of the water is cleaned (by vacuum suction on areas where contamination is visible) and the cleanliness is measured in the space between the barriers by surface tension causing capillary action on a Wilhelmy plate. Once there is no change in tension as the barriers close, the central surface is sufficiently clean. The solution of the molecule is added to the surface of the water within the barriers, with the barriers wide apart and allowed time to evenly disperse. In this case the solvent used for the solution of the molecule must be volatile enough to evaporate off from the surface of the water during this dispersion time. As the molecules are ambiphilic, it is most energetically favourable for the hydrophilic part to submerge itself in the water and the hydrophobic part to remain above the surface. The ambiphilic molecules effectively form a two-dimensional gas between the barriers, which can then be further confined by adjusting the barrier position. As the area the molecules are confined to reduces, the percentage of surface coverage increases until a complete monolayer is formed. The barrier is stopped once a turning point is reached in the surface pressure measurement, as this indicates a single complete monolayer. The substrate is then dipped into the trough and then withdrawn. Whether the substrate is hydrophilic or hydrophobic determines whether a single monolayer or a bilayer is formed on the surface. Typically, hydrophilic substrates will be coated in monolayers and hydrophobic substrates will become coated in bilayers. Samples can be dipped repeatedly (with the barrier spacing adjusted between dips) to create thicker layers, but more layers make the samples less suitable to examination with STM.

4.1.3 Desired characteristics from a molecular network

There are several properties that are desired from an ideal molecular network depending on the function required. Ideally we would want the network to be a perfect crystal of the desired configuration, with no defects throughout the structure. Applications such as catalysis or sensor applications, require the development of a functionalised porous network. If a porous network can be developed so that each layer stacks aligned above the last, we can use layers of a 2D network to created channels in 3D which could act as a molecular sieve for filtration applications. Nanoelectronic devices require a fully conjugated covalent system for electron delocalisation to allow the network to be conducting. Many applications also require pores that can be functionalised easily.

Summary of desired properties from a molecular network

This list summarises the points discussed earlier in this section:

- Minimum number of molecular components, all of which are easily synthesised
- Sufficiently strong bonding for network to be stable at room temperature
- Sufficiently weak inter-molecular bonding for error correction
- Sufficiently weak surface binding for error correction
- High enough affinity with the surface to come out of solution
- Solvent independent structure
- Controllable pore size
- Ability to functionalise as appropriate to desired function

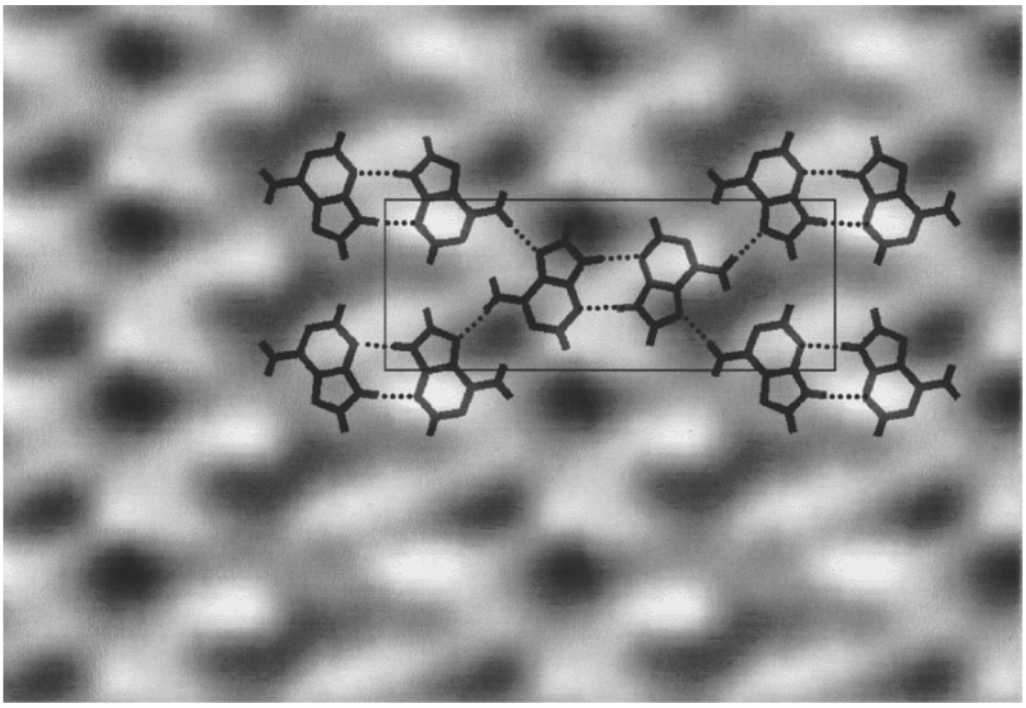

Figure 4.2: Adenine network on graphite. Adapted from [93]. Size of the imaged area = 4.8 nm by 3.2 nm, U=1.0 V, I=90 pA, constant current mode.

4.1.4 Hydrogen bonded networks

In the middle ground between weak van der Waals interactions, and strong covalent bonding, we have the hydrogen bond. Responsible for many of the unusual properties of water [91], the hydrogen bond is a specific type of permanent dipole bond occurring between an electronegative atom with a lone pair, such as F, O, N, and a hydrogen atom bonded to another such electronegative atom [7]. The associated energies are $\sim 20 - 25 kJmol^{-1}$ [7], typically one order of magnitude higher than thermal energy at 298K (standard room temperature). Hydrogen bonding has been of much interest for many years and has been shown to be a key factor in biological systems, such as in the DNA three-dimensional structure shown by Watson and Crick [92]. The hydrogen bonding between base pairs has also been studied in two-dimensions, specifically adenine by Freund *et al* [93] and others, using STM on HOPG surfaces.

Trimesic acid (Figure 4.3) is one of the most extensively studied hydrogen bonding carboxylic acids with over 40 years of work using both STM

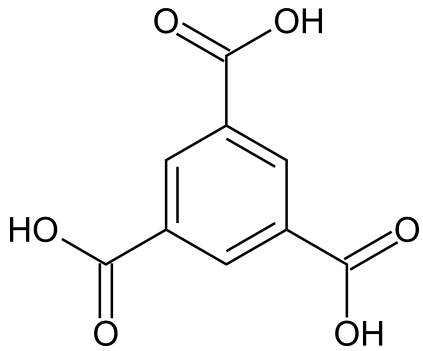

Figure 4.3: Line structure of trimesic acid

and X-ray crystallography. Duchamp's X ray work has focused on the 3D crystal structure [94] and observed a series of interlinked two-dimensional hexagonal 'chickenwire' sheets held together with hydrogen bonding. Study of these two dimensional sheets helps us to understand the three-dimensional structure, and many other papers have been published on trimesic acid [95]. A key feature of this network is the presence of 1.4 nm pores in the structure. Work has also been performed on derivatives of trimesic acid with minor changes to the molecule to study the effect this has on the properties [95].

Lackinger *et al* [96] studied hydrogen bonded networks between molecules of trimesic acid, and observed a case of solvent induced polymorphism, that is, two different structures forming for the same molecule on the same substrate, dependent on the solvent from which the deposition occurred. It is partly due to this observation by Lackinger *et al* that molecules require examination in several different solvents before the bonding within the networks they form can be fully understood.

Korolkov *et al* also managed to image the same hexagonal pored bonding structure for trimesic acid in aqueous solutions [97] demonstrating that the network can be formed without the need for harmful organic solvents.

Some work has gone towards pore functionalisation of trimesic acid networks but to date most of the additions have been made with the aim of increasing understanding of the relationship between the molecular structure and the crystal structure, rather than for a specific application [95].

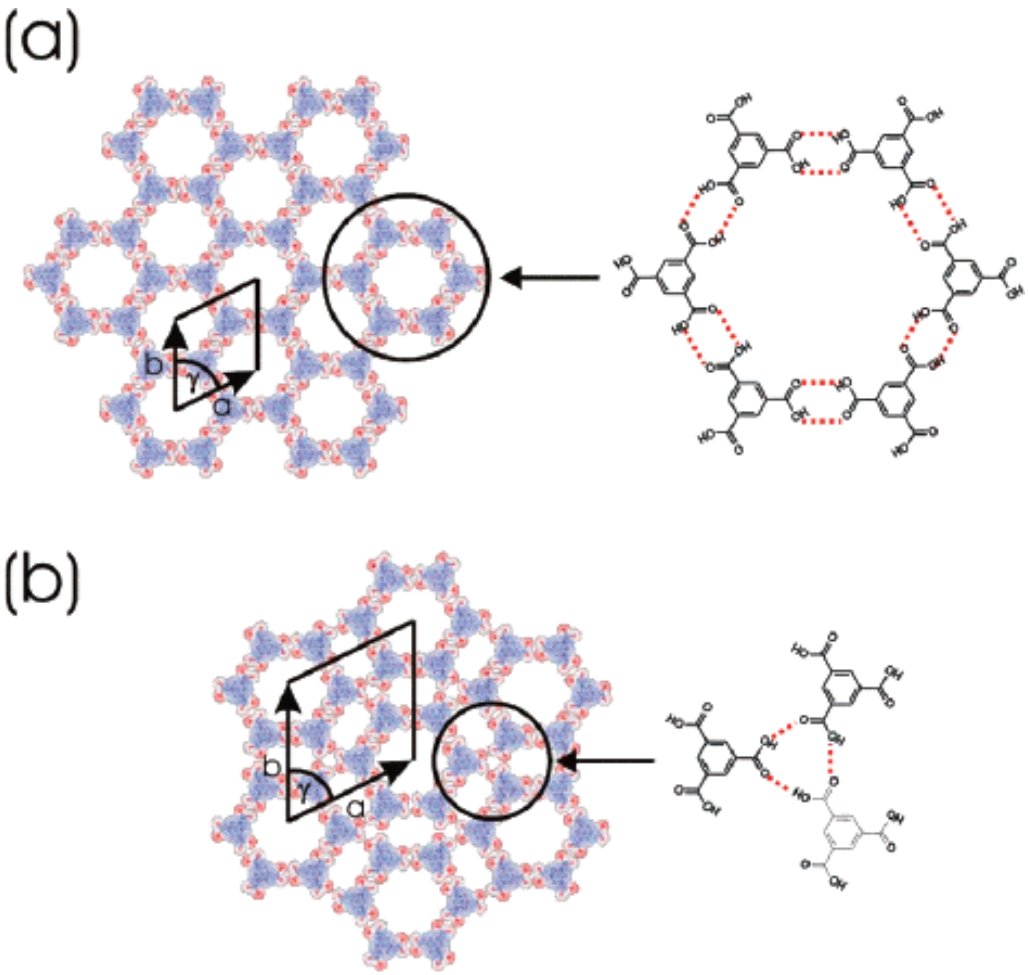

Figure 4.4: Schematics of the two trimesic acid networks observed by Lackinger *et al* [96], a) chickenwire structure ($\alpha = \beta = 1.7$ nm, $\gamma = 60$, area = 2.5 nm^2, 2 molecules per unit cell) and b) flower structure, ($\alpha = \beta = 2.5$ nm, $\gamma = 60$, area = 5.4 nm^2, 6 molecules per unit cell). Observed by STM under ambient conditions on a HOPG substrate in a) heptanoic acid and b) pentanoic acid.

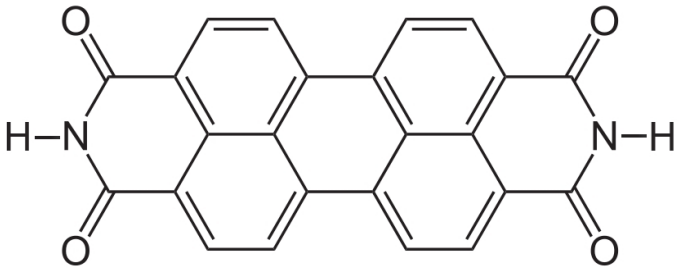

Figure 4.5: Line structure of perylene tetra-carboxylic di-imide (PTCDI)

Modifications have been made for testing what can be added as additional side chains to the central aromatic ring without disrupting the stability of the network.

An alternative example of network featuring regular hexagonal pores, similar to the trimesic acid case, is the two component network between molecules of perylene tetra-carboxylic di-imide (PTCDI, Figure 4.5) and melamine (1,3,5-triazine-2,4,6-triamine, Figure 4.6) [80,98]. These two components form a network which is of the same symmetry as the one formed by trimesic acid but is much more structurally stable. The pore size is larger in this network at approximately 3.5 nm [98]. The increase in stability is caused by the fact the molecules are held together with a triple hydrogen bond instead of a single one. The use of a triple hydrogen bond allows for a hetero-bonding configuration, with the two outer hydrogen bonding groups on PTCDI acting as hydrogen bond acceptors, and the central group as a hydrogen bond donor. There have also been observations of a second phase which alternates between hexagonal pores and smaller rhomboidal pores (see Figure 4.8) [98]. This second form is typically found at the edges of the more common chickenwire phase.

Although the PTCDI molecules can interact with each other, the geometric restrictions limit the number of hydrogen bonds that can form between a PTDCI pair, to two. As the PTCDI-melamine network has three hydrogen bonds per junction it is energetically favoured for the binary network to form. Use of multiple hydrogen bonds to form a network provides a network which is stronger than a single hydrogen bonded network, yet pro-

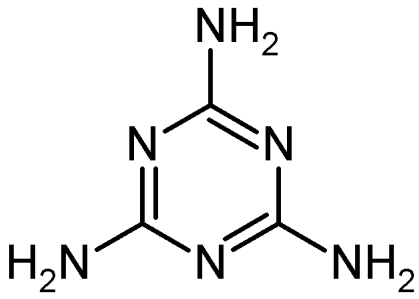

Figure 4.6: Line structure of melamine (1,3,5-triazine-2,4,6-triamine)

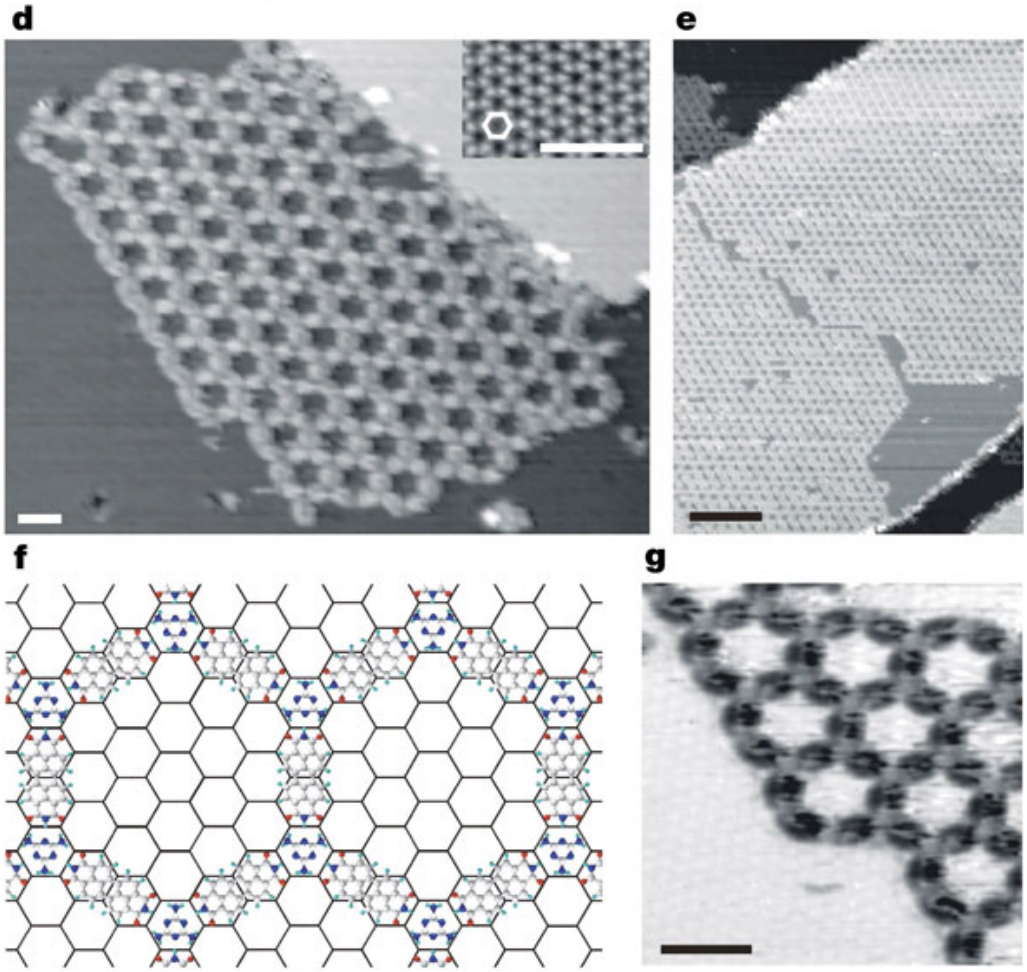

Figure 4.7: d) STM image of a PTCDImelamine network (sample voltage 22 V, tunnel current 0.1 nA). Inset, high-resolution view of the Ag/Si(111)-$\sqrt{3}$ x $\sqrt{3}R30°$ substrate surface. Scale bars, 3 nm. e) STM image of large-area network, with domains extending across terraces on the Ag/Si(111)-$\sqrt{3}$ x $\sqrt{3}R30°$ surface (22 V,0.1 nA). Scale bar, 20 nm. f) Schematic diagram showing the registry of the network with the surface. g) Inverted contrast image (22 V, 0.1 nA) of the network. Scale bar, 3 nm. From reference [80]

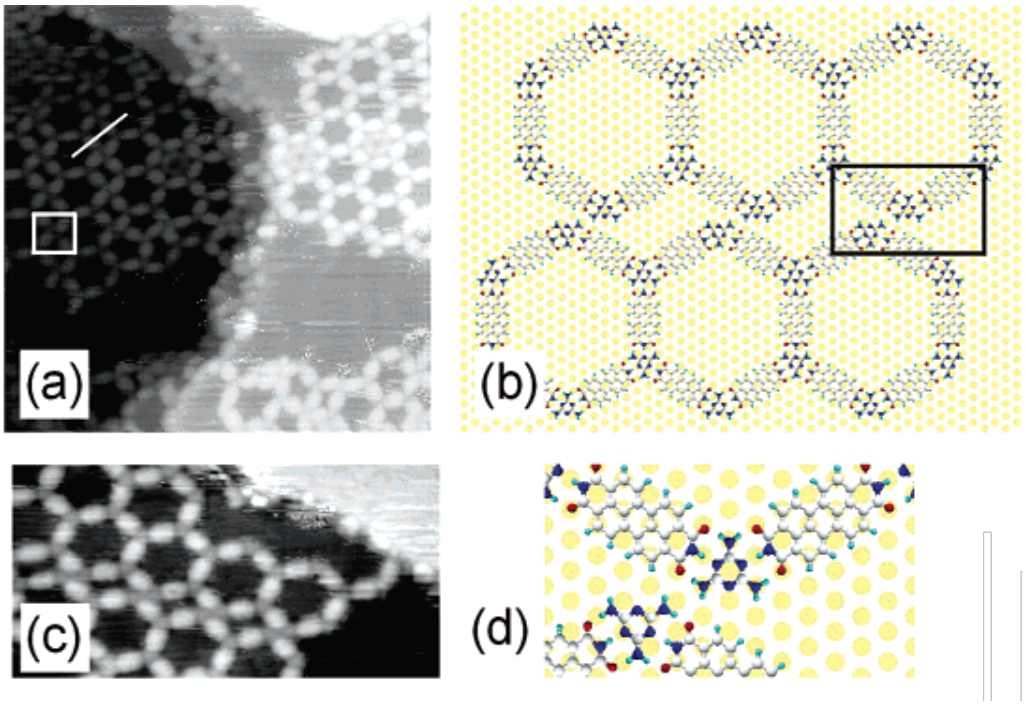

Figure 4.8: Alternative network for the PTCDI - melamine network on gold. a) STM image with a white bar showing the separation of hexagons and the highlighted region showing the new junction. b) schematic for the mixed hexagonal-rhomboidal phase on gold. c) higher resolution image of the junctions. d) More detailed schematic of area highlighted in part b. Image adapted from [98]

vides greater allowance for error correction than covalent bonding. These two mentioned features improve the suitability of this kind of network for templating or functionalised pore based catalysis, but are unsuitable for nanoelectronic applications.

In this two component network PTCDI is fulfilling the role of the molecule controlling the pore size, and melamine is controlling the symmetry of the network and the shape of the pores. In this case, as melamine is a triangular molecule, the resulting network has three-fold symmetry and hexagonal pores. In principle, a square molecule equivalent of melamine, with equally spaced hydrogen bonding groups, would be expected to form a square shaped pore. PTCDI could be replaced with a similar molecule such as naphthalene tetracarboxylic diimide (NTCDI) [99] to produce smaller pores. There have also been cases where the PTCDI and melamine system has formed only rhomboidal pores, converted from the hexagonal pores by annealing at higher temperatures [100] (see Figure 4.9). Although the rhom-

boidal network has less hydrogen bonding than the hexagonal structure, it was reported to have a higher molecular density on the surface. This highlights the importance of surface coverage in network formation and suggests a limit on the maximum achievable pore size.

Both PTCDI and melamine have been studied individually on Au (111) among other surfaces [101–104], with several different structures identified for each molecule. Calculations by the Castell group on PTCDI predicted that non-porous configurations of PTCDI were more energetically favourable than the porous ones [101]. They note that these calculations did not take account of the substrate or entropic stabilisation effects. Conversely, melamine forms a regular, hexagonal pored phase spontaneously with pore size less than 1.8 nm on Au(111) [98, 104]. On substrates where the substrate-molecule interactions dominate the molecule-molecule interaction, the melamine can stand edgeways [105], highlighting the need for low reactivity substrates for porous network formation. The instability of the porous PTCDI networks (relative to the non-porous ones) suggests that PTCDI would require a second component to be added to the network in order to stabilise the pores (such as melamine as discussed earlier).

Other two component networks include melamine with uracil [106,107], melamine with cyanuric acid derivatives [108], 4,4-bipyridine with cyanuric acid derivatives [109], and PTCDI with uracil [107]. Some of these derivatives use sulphur in addition to the more common oxygen and nitrogen based hydrogen bonds. The dipole on a thiol (S−H) group is not as polarised as hydroxyl (O−H) group, due to the reduced electronegativity of sulphur (2.58 on the Pauling scale) compared to oxygen (3.44 on the Pauling scale) [110]. The smaller dipole leads to weaker hydrogen bonding where sulphur is involved.

In addition to the two component networks there have been some studies on three component networks [107]. Gardener *et al* combined melamine, PTCDI and uracil which, after extensive annealing, formed an extended network with large hexagonal pores on Au(111). This was contradictory to

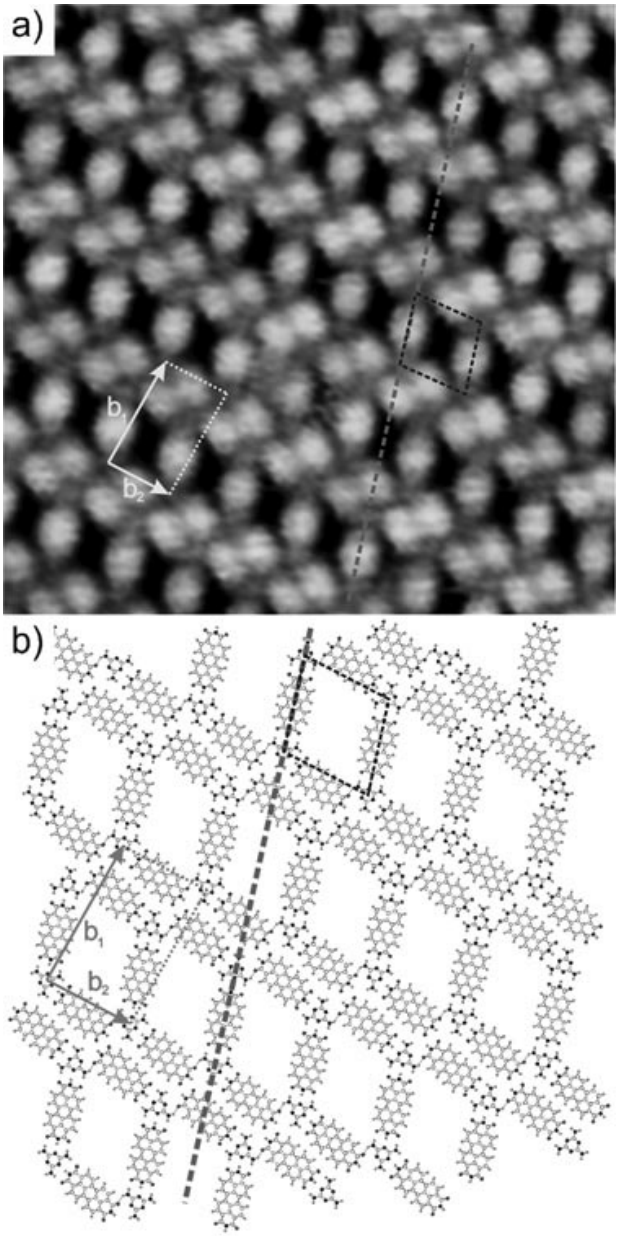

Figure 4.9: a) High resolution STM image showing the rhomboidal form of the PTCDI melamine network (17.5 nm x 17.5 nm, 1.5 V, 0.03 nA) and b) the schematic of the bi-molecular ordering proposed by Staneic *et al.* Figure from [100].

their expectations of phase segregated binary regions. The network they observed after annealing for 10-12 hours at 120° had similar sized hexagonal pores compared to the two component networks but a larger separation distance between them (6.6 nm for the three component network [107] compared to 3.5 nm for PTCDI-melamine [98]).

Some of the largest molecular monomers used to create two-dimensional self assembled structures are porphyrin derivatives. Porphyrins are a class of molecules related to the haem compound which is part of, and gives its name to, the haemoglobin protein found in red blood cells. Porphyrins consist of a planar conjugated organic tetradentate ligand around a metal centre. They can be functionalised in many different positions on the macrocycle, typically generating four fold symmetric structures. Porphyrin networks have been studied with both hydrogen bonding linkages [111] and covalent linkages between the molecules [112].

Figure 4.12 shows an example of a hydrogen bonded network using porphyrin derivatives with 4-carboxylphenyl functional groups studied by Lei *et al* [111]. The full name of the molecule they used is 5,10,15,20-tetrakis (4-carboxylphenyl)-21H,23H-porphyrin which they abbreviate to TCPP. The structure they suggest to fit the scan data features a cycle of four hydrogen bonds resulting in smaller pores than would be observed if the hydrogen bonding groups merely paired up. This demonstrates that if multiple configurations with an equal number of hydrogen bonds are possible, the system will tend towards the most closely packed configuration in order to minimise free surface energy.

4.2 Towards covalent bonding

Work has taken place to realise the additional possibilities available by the progression towards covalent organic frameworks where the molecules are held together via covalent bonding. Covalently bonded networks are ex-

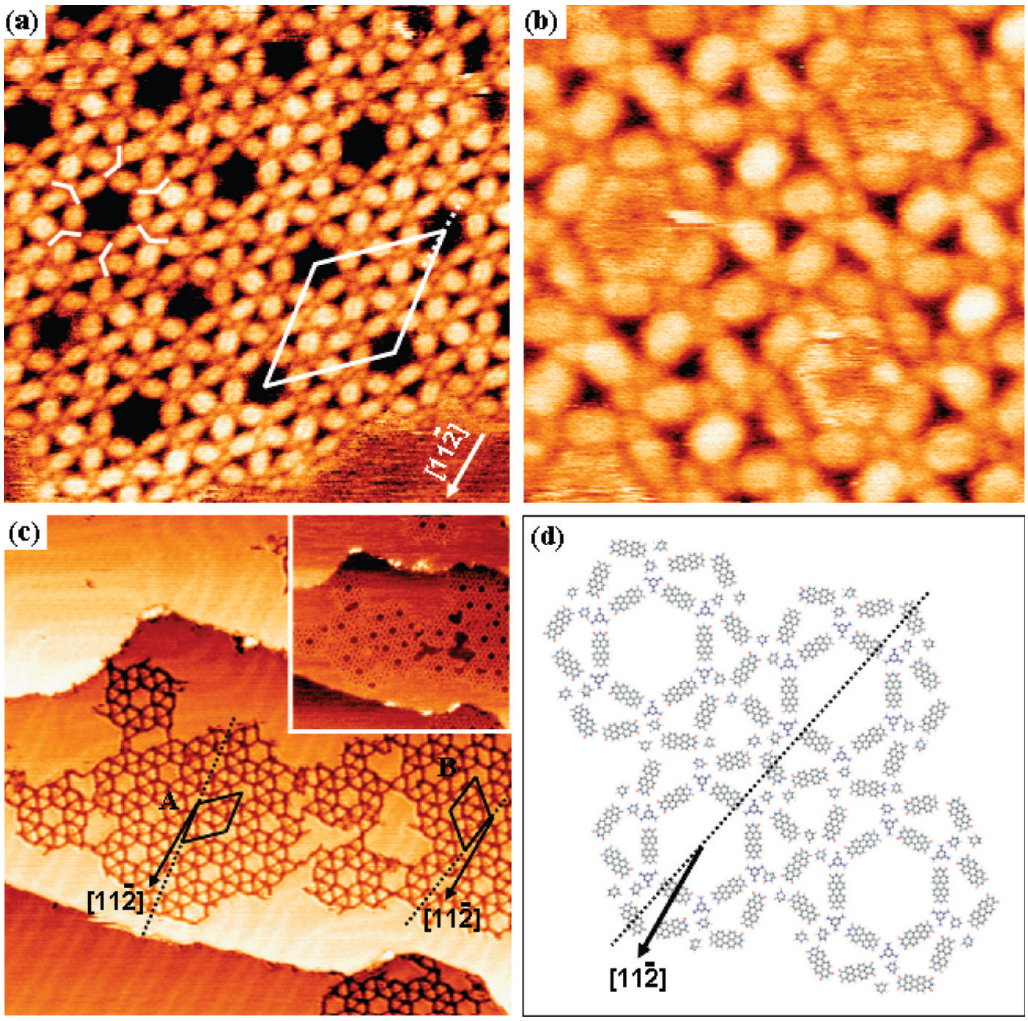

Figure 4.10: **An example three component network comprising of PTCDI, melamine, and uracil.** The white chevrons marked in a) show chirality in the structure. b) A more detailed image of the star network (V_s = −2.0 V, I_t =0.04 nA, 12.8 nm x 12.8 nm). This region is of opposite chirality to that in panel a. c) An image of two regions of the star network, marked A and B, with the herring bone reconstruction of the underlying gold substrate visible. This image displays an unusual contrast effect most likely due to an adsorbate on the tip; an image of the same region of more standard appearance is shown in the inset. (V_s = −2.0 V, I_t = 0.04 nA, 77.1 nm x 77.1 nm) d) A possible arrangement of uracil, melamine, and PTCDI molecules within the star structure. This represents a region with the same chirality as in image b and region B of image c. The stacking and Au(111) [11$\bar{2}$] directions are indicated by a dotted line and solid arrow, respectively. This whole Figure is adapted from [107]

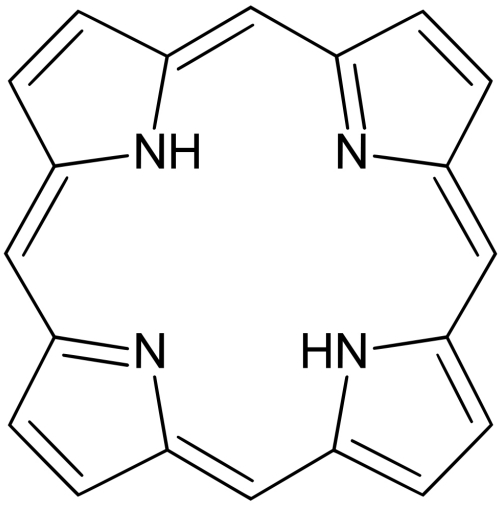

Figure 4.11: Line structure of the basic porphyrin macrocycle. A metal ion (various types) usually resides at the center of this molecule, forming co-ordination bonds with the nitrogen atoms and amine groups. For self assembly studies the basic macrocycle will have additional side groups appropriate for inter-molecular bonding.

pected to have an improved thermal and chemical stability when compared to hydrogen bonded networks and allow the development of fully conjugated systems capable of electron transport [26]. They are often referred to in the literature as surface covalent organic frameworks (SCOFs or sometimes just COFs).

Formation of covalently bonded structures require different functional groups in place of the carboxylic acid group. Reactions that are known to work well at linking two organic molecules include variations of the Ullmann reaction [113, 114], in which a carbon-halogen bond of an adsorbed molecule is cleaved, or a condensation reaction [115–117]. While condensation reactions are fine for UHV studies, where the molecules are deposited by vapour deposition, there are significant disadvantages. Condensation reactions require two different functional groups (such as an amine group and a carbonyl group), which introduces either orientation based restrictions or requires a two component system. Additionally condensation reactions restrict the use of solvents, as commonly used solvents for molecular deposition on a surface often contain carboxylic acid, or alcohol groups, which would also be capable of forming covalent linkages with the networking molecules. In addition, these condensation reactions are more easily reversible, lead-

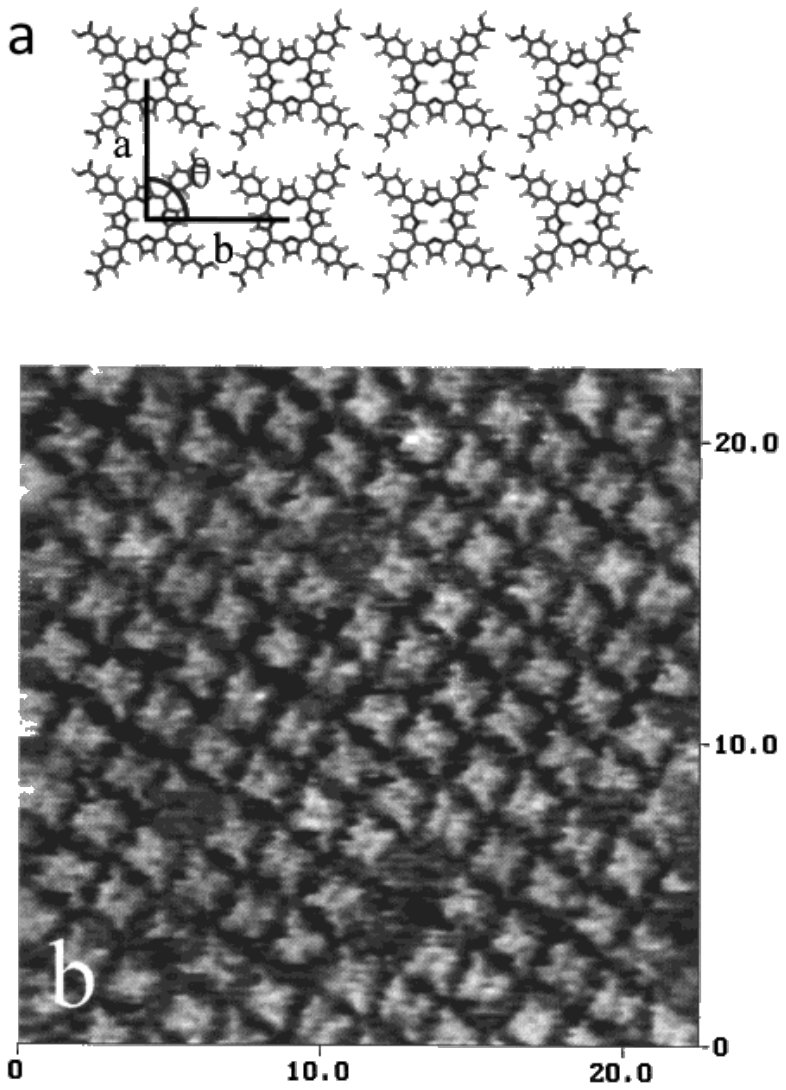

Figure 4.12: a) Lei *et al* suggested this structure for the hydrogen bonded network of the porphyrin derivative TCPP. b) STM data of a 4-fold symmetric 2D network of TCPP in stearic acid on HOPG. Tunneling conditios: 852.3 mV, 1.089 nA. Figure adapted from Figures 2b and 3b from reference [111]

ing to a reduced chemical stability compared to other covalent bonding schemes [118] (but they would still be more chemically stable than hydrogen bonded networks). Although the reversibility of the reaction improves error correction and therefore reduces defect density [117], the fact that the reverse reaction is activated by the presence of water at room temperature, limits the potential applications.

Coupling based on variations of the Ullmann reaction do not have the problems associated with condensation reactions. Bonding between a pair of molecules occurs through a single halide on each molecule.

The Ullmann reaction usually requires catalysis from the copper (111) surface [119], but there are many cases of aryl-aryl coupling with other metals acting as a catalyst [120]. The Ullmann reaction was one of the first covalent reactions to be performed on individual pairs of molecules induced by STM [121]. Another example of the Ullmann style aryl-aryl coupling can be seen in work by Fasel *et al* [122] where they examine 10,10'-dibromo-9,9'-bianthryl adsorbed onto an Au(111) surface and successfully form graphene nanoribbons under UHV conditions. Although they were able to form an extended conjugated system, the Fasel group did not have control over the direction of these ribbons relative to the plane of the underlying substrate. Grill *et al* [112] showed the Ullmann reaction can form covalent structures in 4-fold symmetric systems under UHV conditions. At the time the experiments in this thesis were performed, there was no known study of 3-fold symmetric systems covalently linked outside of vacuum.

Chapter 5

Tetracarboxylic acids and Hydrogen bonded networks

5.1 Related tetracarboxylic acids in the literature

One group of molecules which form interesting networks are carboxylic acids, especially di- tri- and tetra-carboxylic acids. Although there have been cases of three-dimensional self assembly of tetracarboxylic acids [123], it is the two dimensional cases which is of interest to us.

Tetracarboxylic acids are an example of a class of molecules which form extensive hydrogen bonded, two-dimensional, molecular networks as discussed in section 4.1.4. The progression towards studies of tetracarboxylic acids comes as an extension from work on trimesic acid, with the simple tetracarboxylic acid biphenyl-3,3,5,5-tetracarboxylic acid effectively being two trimesic acid molecules, covalently bonded [124].

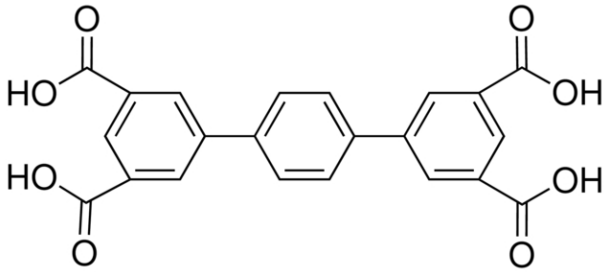

Figure 5.1: **TPTC:** The chemical structure of the TPTC molecule which forms the rhombus tilings.

5.2 TPTC

The molecule p-terphenyl-3,5,3,5-tetracarboxylic acid (see Figure 5.1) referred to as TPTC from here on, is an example of a molecule which can form two-dimensional, single component, molecular networks. TPTC has proved to be an interesting molecule due to the entropically stabilised random tilings which have been observed by Blunt *et al* [125], Stannard *et al* [126] and others.

Previous work using this molecule has looked at the formation of structures on the substrate HOPG, from solution in organic acids (such as nonanoic acid $CH_3(CH_2)_7COOH$). Examples of a random tiling network have been observed, with the molecules able to sit in one of three orientations (Figure 5.2) and the STM data can be mapped onto a rhombus network for easier statistical analysis. Each molecule can be assigned to a coloured rhombus, with each edge of the rhombus aligned to where one of the carboxylic acid groups can form a hydrogen bond. In order to perfectly tile a surface, the rhombus must have internal angles of 60° and 120°. The distance between phenyl rings across a hydrogen bond, has been previously measured to be 0.96 nm [126]. The colour of each rhombus is used to easily identify the orientation of the molecule with respect to the other molecules within that crystallite. It should be noted that there may be some rotational disorder between different crystallites.

The three orientations of the molecule can combine to result in five different types of molecular junction. These junctions are classified based

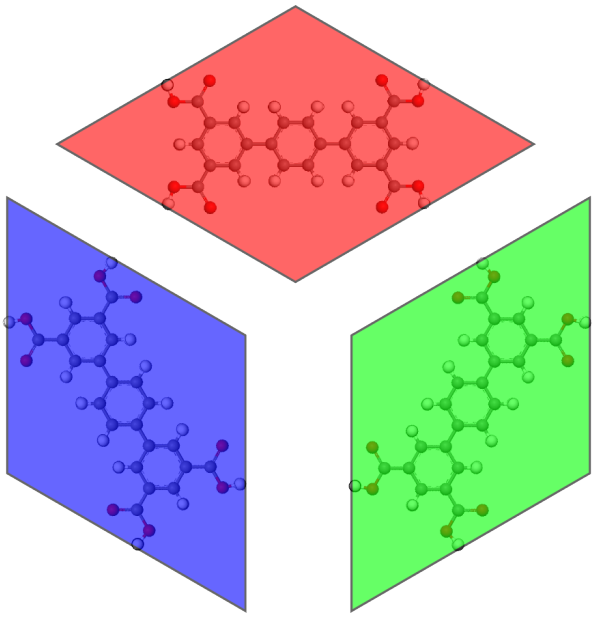

Figure 5.2: **Rhombus Mapping:** Each molecule can be assigned to a coloured rhombus, with each edge of the rhombus aligned to one of the carboxylic acid groups

upon the number and orientations of the rhombi surrounding a point. We have called these junctions 'triangle', 'arrow', 'parallel', 'sunrise' and 'star', as defined in Figure 5.3. DFT calculations performed by Blunt *et al* [125] show that both parallel bonding and non-parallel bonding schemes between TPTC molecules have an equivalent binding energy of 0.80 eV.

Stannard *et al* [126] developed a method for quantifying the degree of 'randomness' within the tiling networks, that is, the degree to which one bonding geometry is preferred compared to another. This involved classifying the interactions between two molecules as either *parallel*, where the molecular axes lie parallel to each other (such as Figure 5.3b), or *non-parallel*, where they do not (such as Figure 5.3a). In a system where the tiling is truly random, the energy of these two states will be degenerate and the structure of the resulting network will be entirely entropically driven. They defined an order parameter Ψ given by:

$$\Psi = \frac{n_0 p - p_0 n}{n_0 p + p_0 n} \tag{5.1}$$

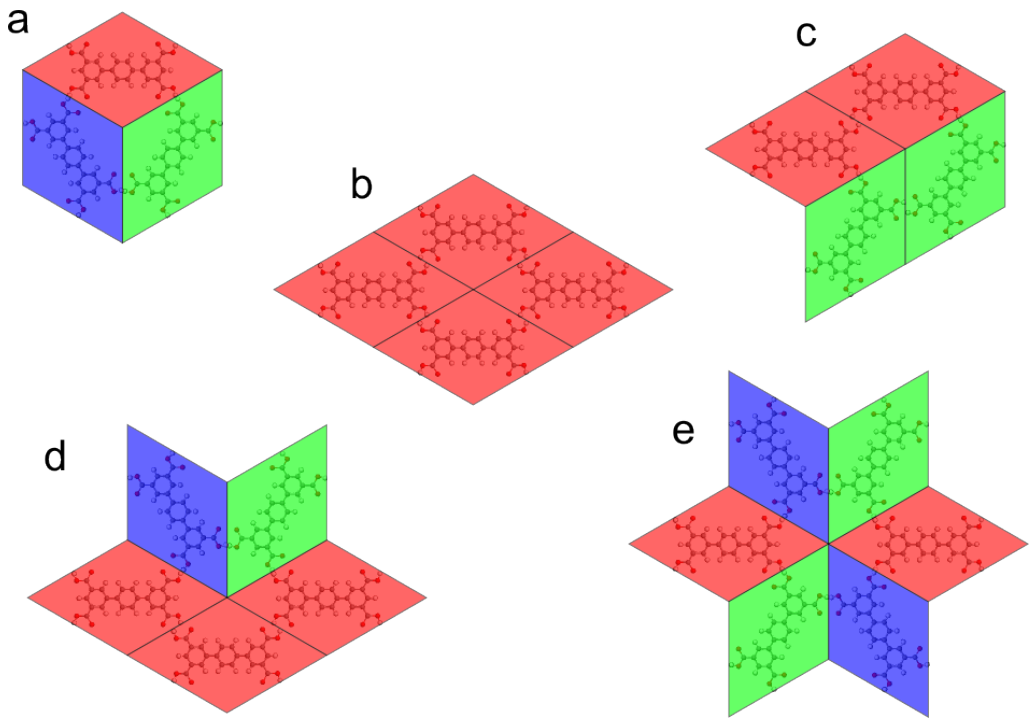

Figure 5.3: **Rhombus junctions:** The five types of rhombus tiling junctions. Throughout this work they will be reffered to as: a)triangle, b)parallel, c)arrow d)sunrise, and e)star.

where n is the fraction of non-parallel interactions between molecules within a tiling network and p the fraction of parallel interactions within the same tiling network. $n_0 = 0.608$ and $p_0 = 0.392$ are constants from the fractions of each interaction in an ideal defect free random tiling calculated by Stannard *et al.* They compared the values of Ψ for a variety of different molecules and solvents within their studies [126].

5.3 Random tilings on graphene on copper

The order parameter Ψ for random tiling networks of TPTC has been shown to vary through the use of different solvents, but no investigation has occurred into different substrates. The micro/nano electronics industry has been making major developments towards including graphene in many new experimental devices, and due to recent developments in graphene transfer, it can be used on many different materials.

Graphene on copper was selected as a substrate for several reasons. First, copper is the metal upon which single layer graphene has been reliably grown as monolayer [67] and is commercially available. As there is no need for the transfer of the graphene film, we do not risk adding any additional defects which may be caused by such a process. Second, copper is rougher than the HOPG, silicon or Au(111) substrates commonly used in STM, so if the tiling is stable on the graphene here, it is likely to be so on many other simpler surfaces.

5.3.1 Experimental procedure

TPTC molecules were synthesised by the Champness group in the School of Chemistry here at Nottingham. Synthesis details are as described in supplementary information in Blunt *et al* [127]. Single layer graphene on 20 μm thick copper was supplied by Graphene Laboratories Inc. A 10 μL droplet of a saturated solution of TPTC in nonanoic acid was placed onto a square of graphene on copper $\approx$ 5 mm by 5 mm and was loaded immediately for scanning.

STM images were acquired with an Agilent Technologies 4500 PicoPlus STM using a PicoScan controller and STM tips formed from mechanically cut PtIr (80:20) wire.

5.3.2 Tiling statistics of TPTC on graphene on copper

The TPTC molecules appear as bright rods within the STM images and can be observed at several different angles. In some cases some hints at the finer substructure are visible (see Figure 5.5). Each image is reconstructed into a tiling pattern as indicated in section 5.2. Duplicate areas are not counted in order to minimise the skewing to the data caused by oversampling of one region. Each image is optimised for contrast using the WSxM software package [128] and converted into a jpeg file, with quality set to

Graphene on Copper Tiling statistics	
Parallel interactions	2125
Nonparallel interactions	5253
Total interactions	7378
Ψ	-0.23 ± 0.01
Average crystallite size	29.8 ± 0.1 nm
Average interactions per crystallite	180

Table 5.1: TPTC random networks on graphene interaction statistics

maximum, resulting in no data loss during file type conversion. Conversion into a rhombus tiling was performed manually using graphics editing software Inkscape [129]. This step is preceded by labelling each junction point between adjacent molecules by placing a coloured ring over each pore to label the different types of junctions seen in Figure 5.3. Identifying the junction type makes it easier to see crystallite domain boundaries. Counting was done using the colour threshold (to select all items of a single colour) and particle analysis functions (to count the number of selected particles) in ImageJ [130].

The number of interactions of each type (parallel and non-parallel) were totalled across over 30 different crystallite domains of various sizes from several different distinct scanned areas, examples of which are included in Figures 5.5, 5.6 and 5.7. The totals were substituted into equation (5.1) for p and n respectively and an overall order parameter was determined to be $\Psi = -0.23$. Only interactions for which the orientation of both the bonding molecules can clearly be seen, are counted. The average crystallite size for the graphene on copper substrate was much smaller than previous work has shown for HOPG. As only interactions with other molecules are accounted for in the Ψ value, the edges of domains can skew the values calculated for individual domains. It is for this reason that the total interactions from all the data was used for the calculation, rather than an average Ψ for the individual domains. The average domain size is calculated by measuring the minimum and maximum distances across of thirty four different domains through the centre.

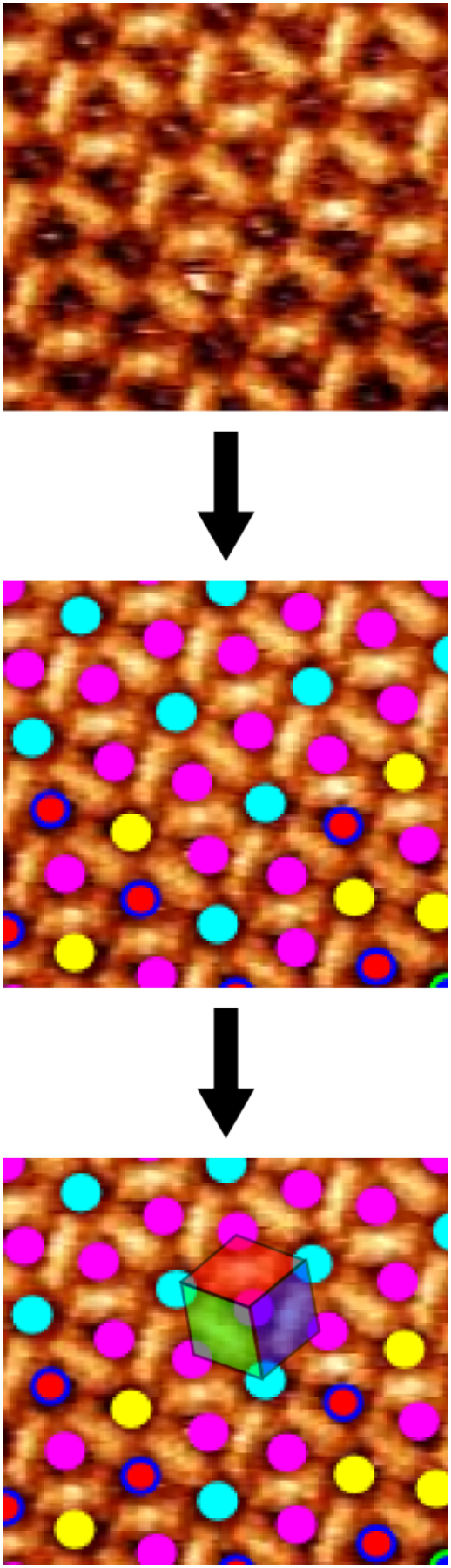

Figure 5.4: **Tiling process for TPTC on graphene on copper from nonanoic acid:** Contrast is optimised for viewing of the bright areas corresponding to the molecules. Each molecular junction in the scan data is examined and assigned a colour according to the grouping. From this grouping each molecule is then assigned a coloured rhombus for tiling statistics as shown. Molecules which are not part of one of the recognised configurations are often unresolvable or distorted to the point where it is unclear of the orientation, and are neglected as they are usually associated with defects.

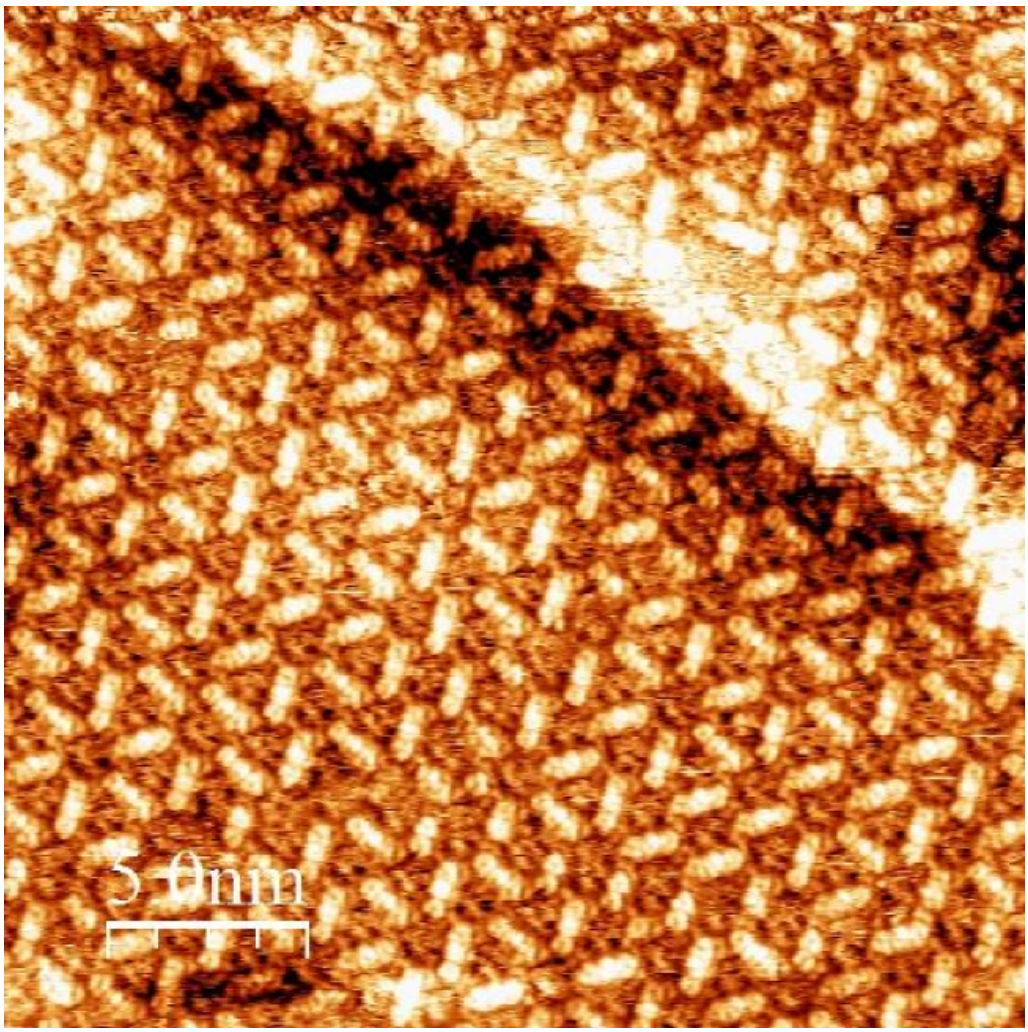

Figure 5.5: **Example STM image of TPTC on graphene on copper from nonanoic acid.** For this image a set point of 0.05nA and a bias voltage of 0.6V were used. This image shows the normal contrast for TPTC molecules in the random tiling configuration. The scale bar is 5 nm.

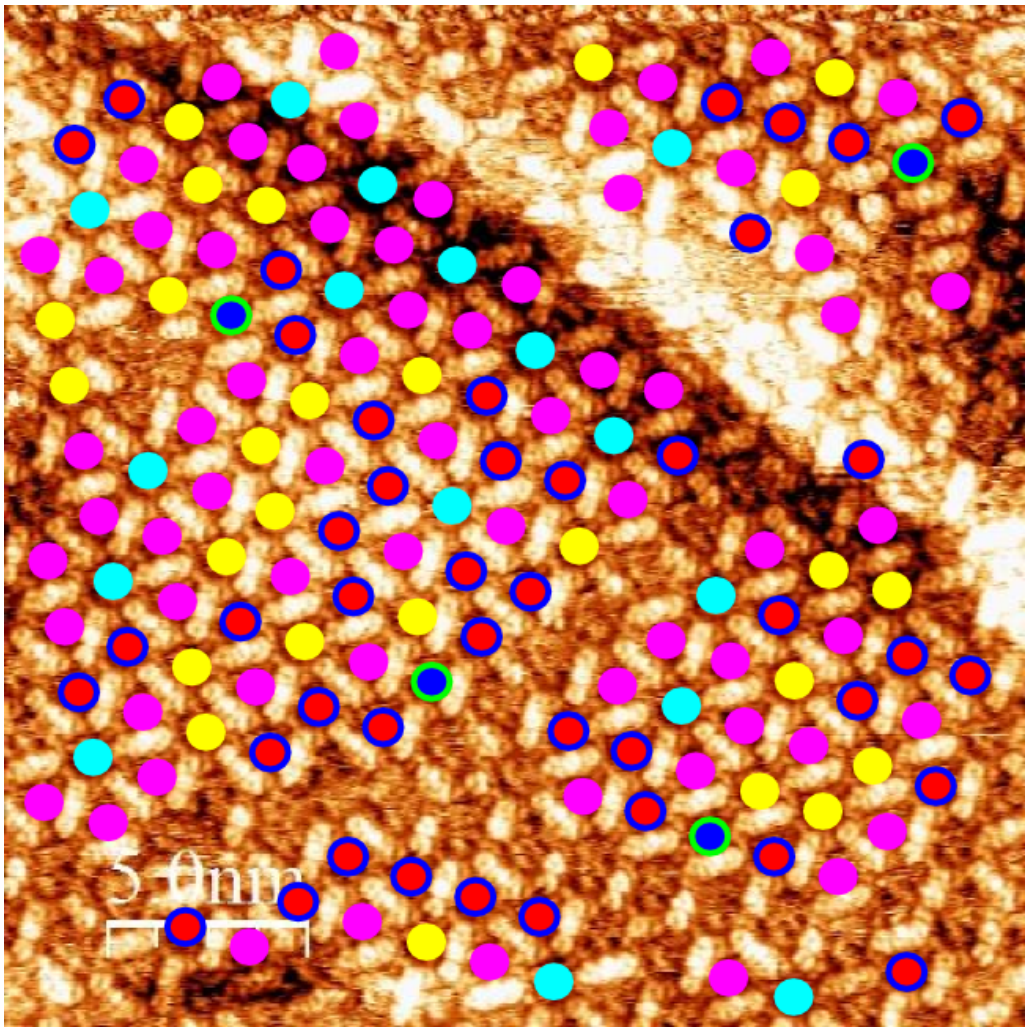

Figure 5.6: **Assigning molecular junctions.** Taking the STM image from Figure5.5, each molecular junction has been labelled a different colour (or combination of colours) to identify the five possible junctions outlined in figure 5.3. From this labelling it is clear that the rhombus network is discontinuous over the step edge. The distinction between domains is less clear if the rhombus alignment is fitted directly.

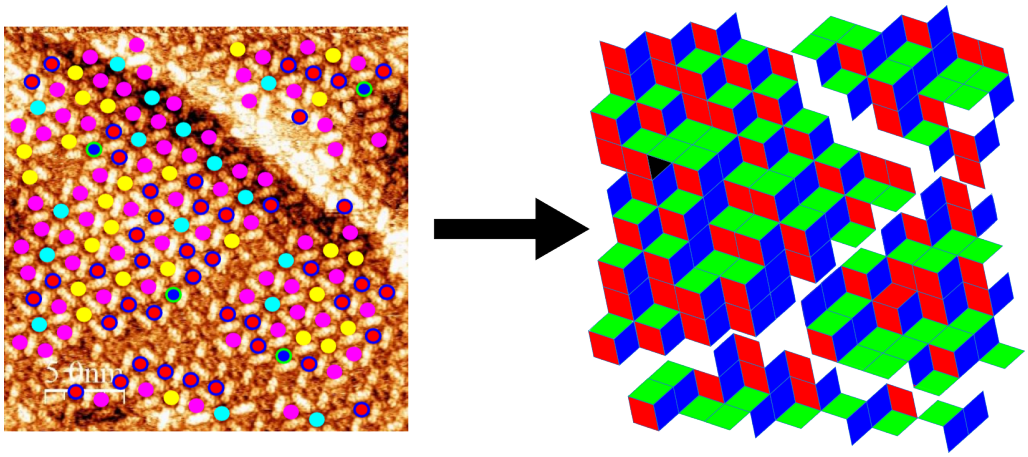

Figure 5.7: **Final conversion from the moleular junction map to the rhombus tiling.** Tiling is performed using both the scan image and the junction map in combination. Once the rhombus tiling is complete, the other layers are hidden before counting the tiles for statistical purposes. Note the vacancy defect (marked black) in the middle left region.

Rhombus Junction configuration ratios	
Triangle	39%
Parallelogram	4%
Arrow	28%
Sunrise	22%
Star	7%
Total junctions counted	3546

Table 5.2: TPTC Rhombus Junction Ratios on graphene on copper to the nearest percentile.

The types of junction points between rhombi were totalled across the data from the rhombus mappings which contributed to Table 5.1. If we had $\Psi = 1$ (parallel bonding only) we would exclusively have the parallel junction type , for $\Psi = -1$ (non-parallel bonding only) we would only have the star (35%) and triangle (65%) junction types present. The ratios of the five types of bonding junctions are shown in Table 5.2. Labelling the junction sites makes it much clearer to see the grain boundaries between domains. The crystallite sizes are much smaller than observed in the images in Stannard *et al* [126], with our values for the recrystallised rhombus tilings having a mean crystallite size of 29.8 ± 0.1 nm. We attribute this decrease in average crystallite size to the rougher surface caused by the underlying polycrystalline copper.

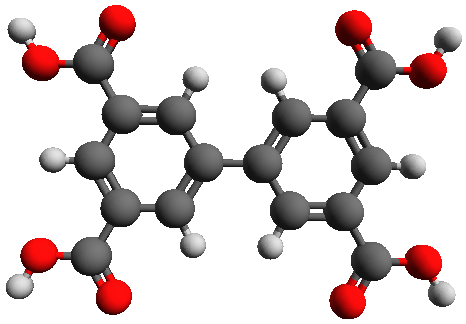

Figure 5.8: 3D space model of biphenyl-3,3',5,5'-tetracarboxylic acid (BPTC)

5.3.3 Conclusions TPTC on graphene on copper

This work has shown the possibility of imaging molecular networks on graphene coated copper substrates and demonstrates that the graphene grown on copper is of sufficient quality for STM studies. The surface roughness made imaging more challenging than other substrates, and the high reactivity of copper led to rapid degradation of the sample, but this can be avoided by using other solvents. Alternate solvents may however lead to different structures to the random rhombus tiling.

5.4 Structure vs chain length on HOPG from water

This section examines how the length of the organic backbone affects the network formed. In this section we introduce two new molecules related to TPTC, a shorter one: biphenyl-3,3',5,5'-tetracarboxylic acid (BPTC) [124], and a longer one: quaterphenyl-3,3',5,5' -tetracarboxylic acid (QPTC). Each of these two molecules have a phenyl group difference in length to TPTC. These molecules have also been looked at on Au(111) by other members of the research group [131].

With a longer backbone, as found in QPTC, we expect a shift in the the tiling patterns towards a preference for the parallel bonding phase. Con-

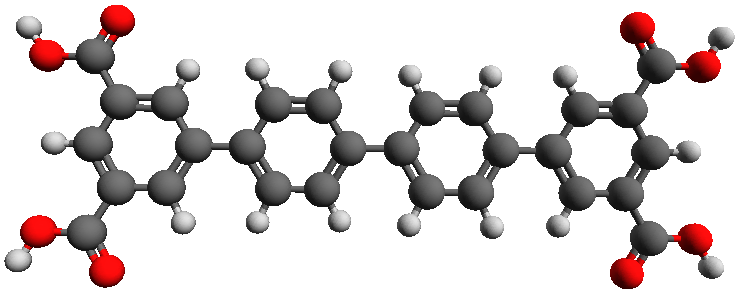

Figure 5.9: 3D space model of quaterphenyl-3,3',5,5' -tetracarboxylic acid (QPTC)

versely, with a shorter organic backbone, such as is the case with BPTC, we expect a shift in the tilings to favour an anti-parallel bonding scheme. This is due to the effect reported by Stannard *et al* which showed a more parallel structure for the molecule with the longer backbone, although in their case the backbone itself was different between the two molecules. [126]. Any deviation from this is expected to be an effect of either the substrate surface or the solvent molecule. Water has been chosen as a possible alternative solvent to investigate solvent dimorphism [96], following work showing network formation of the chemically similar trimesic acid from water [97]. The use of water as a solvent investigates a possible green chemistry approach to the formation of rhombus tiling networks.

5.4.1 Sample Preparation

Powdered TPTC, QPTC, and BPTC was synthesised by the Champness group in the School of Chemistry, here at the University of Nottingham, and the structure was verified using proton NMR. Saturated solutions were prepared by the addition of the powder to ultra-pure water. The water used came from our in house water purification system which consists of several stages of filtering and purification (including UV filtering). When leaving the filtering system, the water has a resistance across 1cm of over 18

$M\Omega$. After preparation, the solutions are ultrasonicated for 30 minutes and left overnight to settle. A 10 mm x 10 mm HOPG block supplied by Agar Scientific ($3.5° \pm 1.5°$ Mosaic Spread), is freshly cleaved using sticky tape to provide a flat clean graphite surface for deposition. Onto this HOPG block we drop cast 20 μ L of solution. This was left to dwell for 5 minutes before being blown off with nitrogen gas.

5.4.2 Discussion of Results: Structural dependence on chain length

BPTC

Initial observations of BPTC on HOPG from water revealed two distinct morphologies. The first one is a disordered amorphous structure (Figure 5.10a). The second shows a clear hexagonal pattern typical of an anti-parallel rhombus tiling bonding scheme (sometimes called a Kagome network in the literature). The structure in Figure 5.10b bears such a great resemblance to the image of TPTC and coronene in nonanoic acid obtained by Stannard *et al* [126] that we became concerned that we may have had a coronene contamination. To eliminate this possibility, all equipment was thoroughly cleaned, a new solution of BPTC in water was made up from a new source of powdered BPTC, and a new HOPG block was used. We still observed both structures roughly equally in frequency between different samples. The cause of the bright features in the centre of the pores, on the anti-parallel configuration, could be caused by solvent molecules adsorbing in the pores.

TPTC and QPTC

Neither TPTC or QPTC formed either the rhombus tiling structure we had seen in samples where deposition occurred from nonanoic acid, or an amorphous phase as seen with BPTC. A structure which initially resembled a

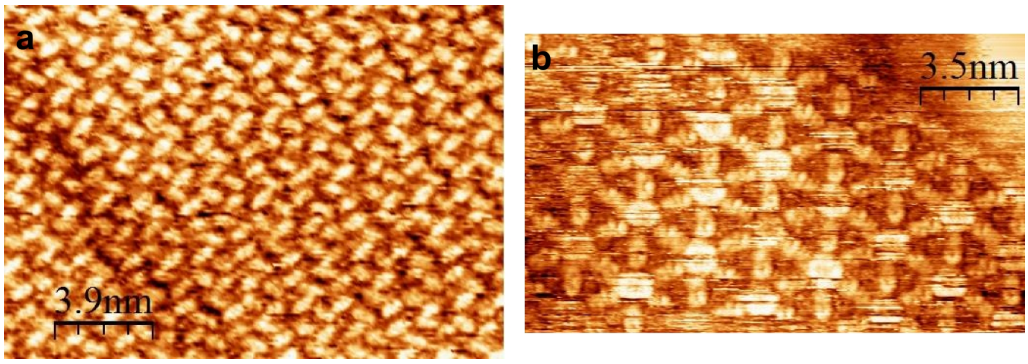

Figure 5.10: a) the amorphous structure of BPTC on HOPG from water and b) BPTC in the anti-parallel rhombus tiling configuration on HOPG from water

fully parallel rhombus tiling was observed, but upon closer inspection it was revealed that this was not the case and we had a new close packed structure present. To further understand the structure we were seeing, a sequence of images of alternating scan directions was obtained. This sequence of images was necessary in order to perform drift correction, as described in section 2.4, and a selection of post processed images were overlayed, with the top image partially transparent, for each molecule as shown in Figure 5.11. Once the drift distortions had been removed it was clear that this was not a parallel rhombus tiling structure.

The structure we observed for QPTC has a lattice where $a = 0.84 \pm 0.02$ nm, $b = 2.43 \pm 0.05$ nm and the angle between them is $\theta = 67° \pm 3°$. For TPTC there appeared to be a partial shift in the lattice in the 'a' direction at several different points on scans we studied. There was much greater long range order in the 'b' direction. The lattice values for TPTC from water are: $a = 0.80 \pm 0.06$ nm, $b = 2.14 \pm 0.05$ nm and angle $\theta = 61° \pm 10°$ between them. These models are shown in Figures 5.12 and 5.14 respectively.

The close packed structure we see here does not show an expected double hydrogen bonding through one corner but instead shows an interaction where the OH of one molecule forms a hydrogen bond as normal but the $= O$ interacts with the partial positive charge accumulating on the central rings of the backbone. This can be taken to suggest that the polarisation of the central rings either results in a larger partial positive charge than the

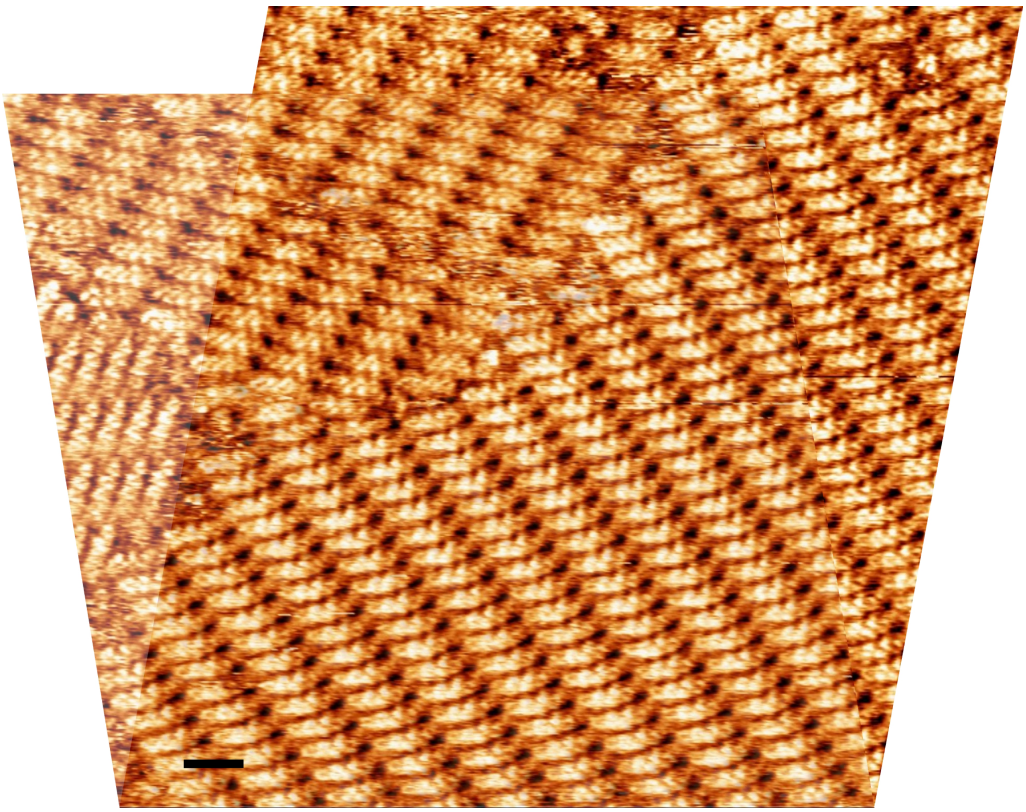

Figure 5.11: **Drift corrected image of QPTC on HOPG from water**. In this case two images have been overlayed and aligned based on the same defect along the grain boundary used to measure the drift for correction calculations. The scale bar is 2 nm

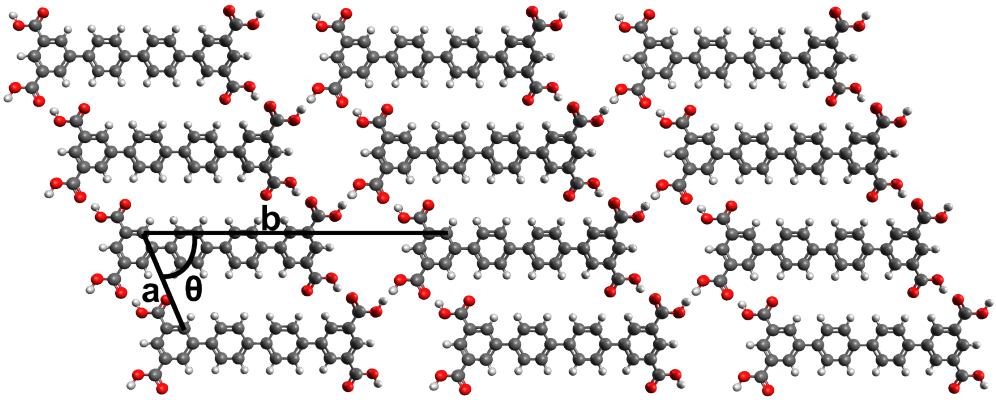

Figure 5.12: **Molecular lattice model for QPTC on HOPG from water**. Note that the polarisation of the central rings is acting as a partial positive charge for stabilizing this structure. The lattice values for QPTC from water on HOPG are:$a = 0.84 \pm 0.02$ nm, $b = 2.43 \pm 0.05$ nm and the angle between them is $\theta = 67° \pm 3°$

Figure 5.13: Drift corrected image of TPTC on HOPG from water. Two sequential images have been overlayed and aligned based on the same defect along the grain boundary used to measure the drift for correction calculations. The scale bar is 8 nm

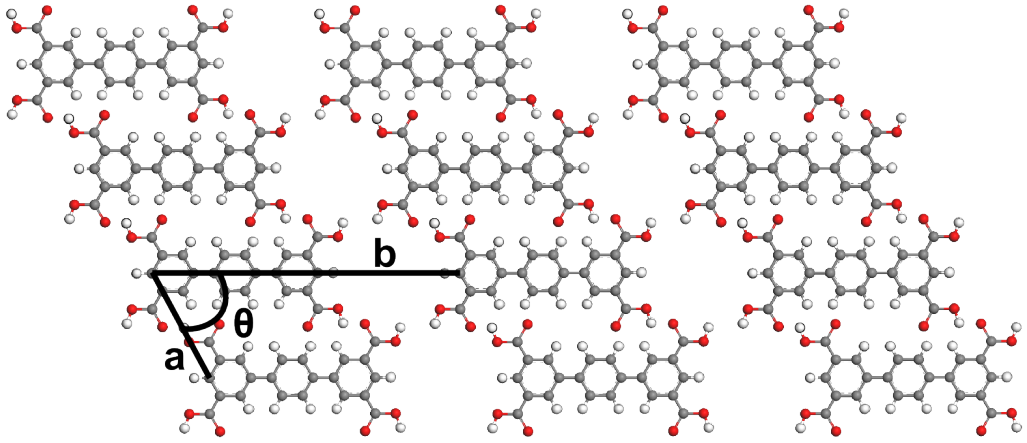

Figure 5.14: Molecular lattice model for TPTC on HOPG from water. Note that the polarised central ring is acting as a partial positive charge for stabilizing this structure. The lattice values for TPTC from water on HOPG are: $a = 0.80 \pm 0.06$ nm, $b = 2.14 \pm 0.05$ nm and angle $\theta = 61^\circ \pm 10^\circ$ between them.

polarisation of the hydrogen in the OH group, or that the close proximity of the oxygen atoms screen the positive charge of the OH hydrogen, giving a longer range to the effective charge on the central ring of the backbone.

5.5 Change of structure with addition of nonanoic acid

The studies by Lackinger *et al* [96] on trimesic acid, found evidence for solvent induced polymorphism in the formation of two-dimensional crystals. For their studies, the solvent from which the molecules were deposited was changed, and led to different phases being observed from different solvents.

In experiments on TPTC performed by J. C. Russell *et al* [132] it was noticed that a tip pulse would cause a change in the structure of TPTC, from the random tilings (as seen in Section 5.2) towards a more close packed structure. As this close packed structure was similar to the structure observed when TPTC was deposited onto HOPG from water, it was decided to evaluate if it was possible to observe a change from the close packed structure to the random network. As it was known (from work by Blunt *et al* [125] and Stannard *et al* [126]) that the random tiling morphology was stable in nonanoic acid, an investigation was carried out into the effect of the addition of nonanoic acid to a dried network of TPTC deposited into the close packed structure from water.

5.5.1 Experimental details

The solutions were prepared in the same way as for the experimental procedure described within Section 5.4. The substrate used is a 10 mm x 10 mm HOPG block supplied by Agar Scientific ($3.5° \pm 1.5°$ Mosaic Spread), which has been freshly cleaved before molecule deposition.

An 80 μ L droplet of the solution was applied to the surface. The volume 80 μ L was chosen to provide a large area coverage of the sample, in order to make it easier to guarantee approaching the STM tip on an area upon which the molecules were present. The droplet was left to dwell on the surface for 15 minutes in order to allow time for a structure to form on the surface. After the 15 min dwell time, the droplet was lightly rinsed off with ethanol (Fluka, ACS reagent grade, $\geq 99.8\%$) and blown dry with nitrogen. The samples were initially imaged in this dried state to confirm successful formation of the structures seen in section 5.4 for TPTC. Samples then had 20 μ L of nonanoic acid (Aldrich, 96%) added to the surface and the samples were imaged at the liquid/solid interface. The best images were obtained with set points between 45 pA and 60 pA with bias voltages between 0.6 V and 1.0 V.

5.5.2 Results: solvent induced recrystallization of TPTC

Images such as Figure 5.15 show that both the close packed structure associated with deposition from water, and the random network associated with deposition from nonanoic acid, are present. This is the typical contrast seen in previous work shown earlier in section 5.3.

There were also cases where uncommon tip structures gave rise to another type of image resolution which can be used to determine the random tiling statistics. This structure, shown in Figure 5.16 has been shown to be convertible into a rhombus tiling (as discussed earlier) by Blunt *et al* [77] using an image where both this 'cloverleaf' resolution and the regular resolution are both visible. Using Figure 5.17, rhombus tiling patterns were obtained for all the data images showing the cloverleaf contrast of the molecule. This data set was combined with the images showing the regular random tiling contrast, after addition of nonanoic acid, to obtain a full set of tiling statistics shown in Table 5.3. The values for junction type ratios in Table 5.3 show similar ratios to that observed on graphene on copper (see

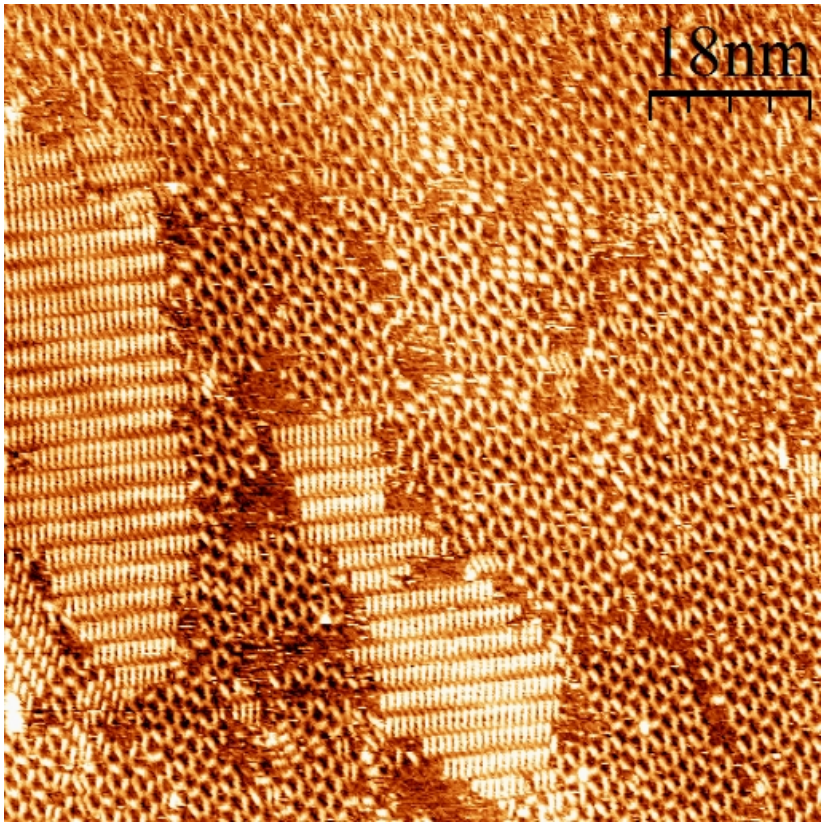

Figure 5.15: Raw data image of TPTC on HOPG. The molecule was deposited from water, dried and then had a few drops of nonanoic acid added to the surface. Here we can see both the close packed structure, and the random tiling network structure are clearly visible. Note that there is significant distortion in this image, caused by thermal drift.

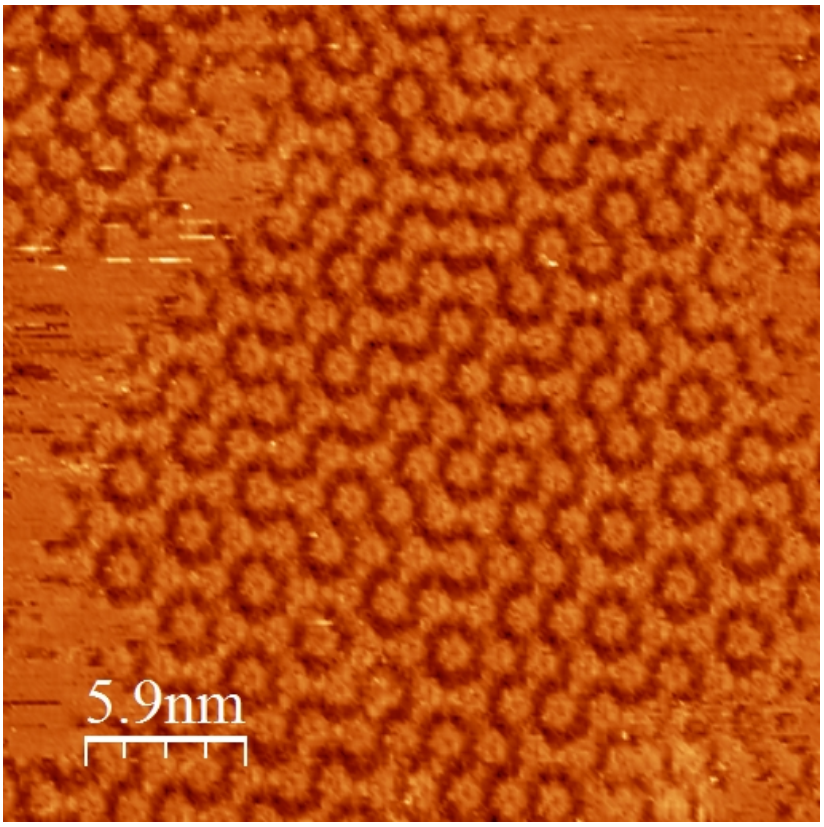

Figure 5.16: Alternative contrast cloverleaf structure for TPTC on HOPG can be observed if the tip is in an appropriate state. It is possible to construct rhombus tilings from these images.

section 5.3). The domains of rhombus tiling network are much larger than those seen on graphene on copper, and as such most of them extend beyond the edges of the scanning area making an estimation of their size impossible with this data. We also observe large areas where there is no molecule breaking up domains. We attribute these gaps to some molecules staying in the solution. For this reason, average domain size has been omitted from Table 5.3.

Nonanoic acid induced rhombus tiling	
Parallel interactions	4288
Nonparallel interactions	11190
Total interactions	15478
Ψ	-0.255 ± 0.008

Table 5.3: TPTC random networks deposited from aqueous solutions after the addition of nonanoic acid.

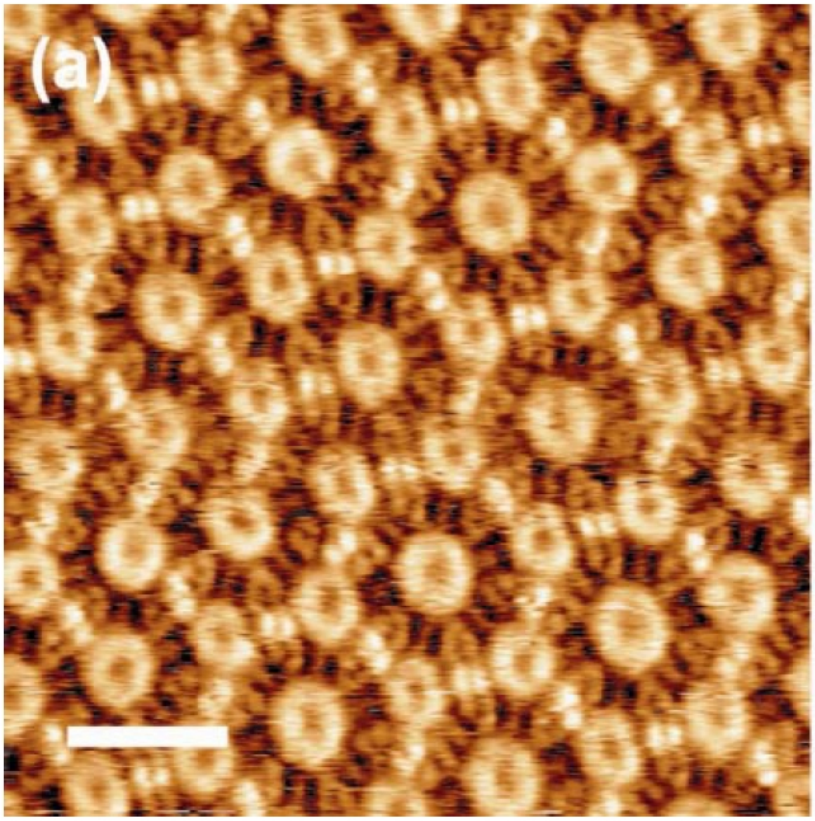

Figure 5.17: Image from [77] showing both the regular and cloverleaf structures of TPTC. Scale bar is 2.3 nm

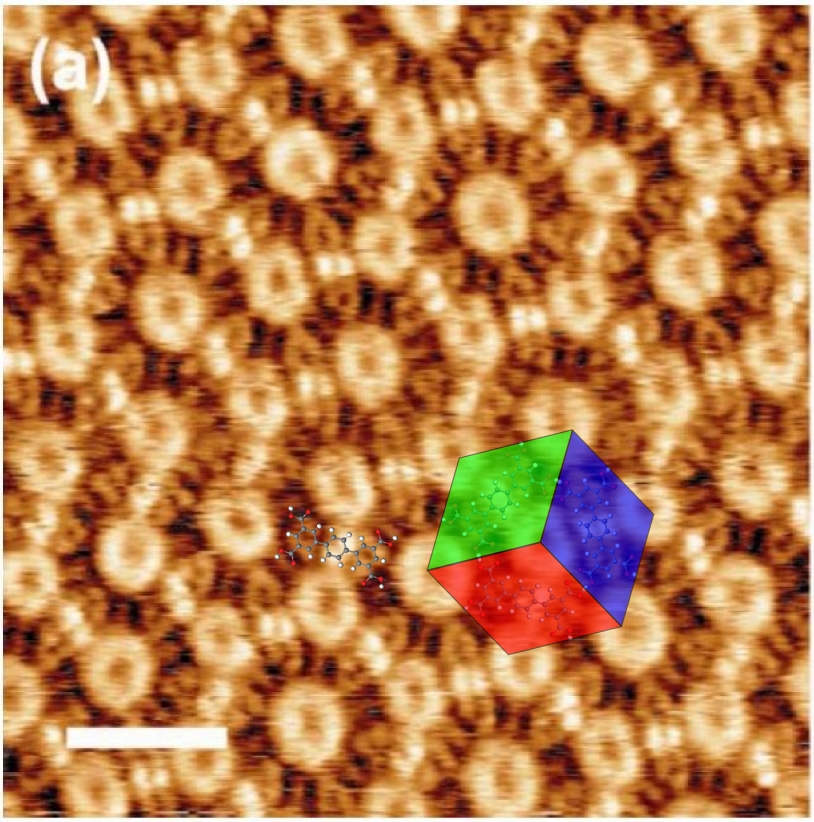

Figure 5.18: Image from [77] with the rhombus tiling overlain. Scale bar is 2.3 nm

Rhombus Junction configuration ratios	
Triangle	40%
Parallelogram	4%
Arrow	26%
Sunrise	21%
Star	9%
Total junctions counted	3870

Table 5.4: TPTC Rhombus Junction Ratios on HOPG after the addition of nonanoic acid, to the nearest percentile. Note the similarities to the values for graphene on copper (Table 5.2).

5.5.3 Conclusions

We have shown that the molecule TPTC also forms a random tiling network on graphene on copper, in addition to that which forms on HOPG, and obtained tiling statistics. We have examined the deposition of TPTC from water and compared the structure to those formed from the related molecules BPTC and QPTC. The molecule TPTC has been shown to exhibit solvent induced polymorphism in network formation. In addition, a structural transition for preformed networks of TPTC has been demonstrated by imaging under a different solvent to that under which the network was formed.

Examining the tiling statistics we can see, in both as deposited networks on graphene on copper, and with polymorphed networks on HOPG, that non-parallel interactions are preferred. For TPTC where nonanoic acid was the most recent solvent the networks had been exposed to, we saw over twice as many non-parallel interactions as parallel ones. In terms of the molecular junctions, the triangular was most prevalent, although it should be noticed that the triangular junction cannot exist without the presence of at least one other junction type. The ratios of the various junction types are similar between both HOPG and graphene on copper, with at most a 2% difference between them.

The values we have obtained for the order parameter Ψ are close to each other (-0.23 and -0.255) yet different to the value of -0.43 for TPTC on

HOPG from nonanoic acid obtained by Stannard *et al* [126]. It should also be noted that the values of Ψ match the value for TPTC on graphene on copper as discussed earlier in this chapter, in section 5.3.2. Our samples also have smaller crystallite sizes than those observed in Stannard *et al*'s work and we attribute these edge effects as a large contribution to the difference in our Ψ value. The presence of these domain boundaries caused a failure of the software designed for automation of the conversion process from raw STM image into a rhombus tiling pattern. The software was also incapable of assignment of images containing the cloverleaf structure and as such, all assignment of rhombus and junction alignment was done manually.

The close packed structure seen in TPTC and analogues thereof when deposited from water show an interaction where the OH of one molecule forms a hydrogen bond as normal but the $= O$ interacts with the partial positive charge accumulating on the central rings of the backbone. The preference for this bonding site over the OH on the functional group is suggested to be due to screening of the hydrogen by the close proximity of the two partially negatively charged oxygen atoms.

5.5.4 Further work

Further work to expand the knowledge of the parameter space surrounding the rhombus random tiling network is recommended. Experiments using a greater range of solvents and obtaining tiling statistics as a function of solvent polarity could help us understand the effects of solvent polymorphism. Initially a good place to start would be seeing if it is possible to observe the transition between the differing order parameters of nonanoic and heptanoic acids. Eventually expansion towards looking beyond solvents from the fatty acid solvent family is a possibility. Further work is currently being undertaken by other members of the research group looking into the formation of the rhombus tiling network (and associated statistics) of TPTC on graphene on silicon oxide. Examination of tiling patterns on other substrates with

threefold symmetry could identify if the rhombus tiling is unique to HOPG and graphene related substrates. As other threefold substrates may not be conducting, atomic force microscopy is recommended as an alternative technique. More data for each of the systems would be ideal to improve the tiling statistics, but an automated system for identification of the different orientations of the molecule that can cope with domain boundaries and other defects needs to be developed to reduce the laborious task of orientation or junction type assignment.

Chapter 6

TBPB molecule: towards covalent bonding

6.1 Introduction to TBPB

Following on from the two-dimensional hydrogen bonded networks discussed in Chapter 5, we progress towards networks which utilise covalent bonding. The molecule we will be referring to as TBPB throughout this document has the IUPAC name 1,3,5-tri(4-bromophenyl)benzene and the structure shown in Figure 6.1.

The molecule was designed with threefold symmetry in mind. The use of symmetrical molecules removes the need for any additional concerns

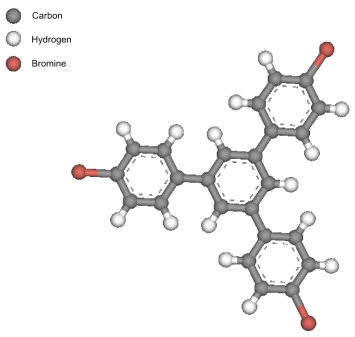

Figure 6.1: The structure of 1,3,5-tri(4-bromophenyl)benzene.

that can be caused by asymmetry. Such concerns would include the need to consider which plane of a molecule is in contact with the surface, or the effects of different enantiomers in chiral molecules. Also symmetrical molecules are easier to synthesise than asymmetric ones [133].

The 3-fold symmetry of the molecule increases its tendency to spread across the surface in multiple directions, rather than forming lines like some more linear molecules [122]. The geometry of the molecule is similar to trimesic acid [97] but with an additional phenyl group between the central aromatic ring and bonding group with the aim to increase pore size. Bromine has been chosen as the halide group for forming the covalent linkages. An important property of the molecule is that the homolytic bond dissociation energy of CBr bonds (3.2 eV) [134] is substantially lower than that of the CC link between phenyl rings (4.8 eV) [135]. This gives quite a broad temperature range where the C−Br can dissociate without the breakdown of the rest of the molecule [78].

It was hoped that these molecules would form an open mesh like structure with large hexagonal pores, similar to the graphene lattice but on a larger scale. Formation of an open hexagonal pore structure, with some degree of long range order, for this molecule had already been observed by Walch *et al* [136] on copper (111) in low temperature UHV experiments, but these had three halides meeting at each junction, rather than two. Other work by the same group did result in larger hexagonal pores following addition of a post deposition annealing step, but there was no observed long range order in this case [78]. UHV studies by Blunt *et al* [137] obtained a structure formed from this molecule on Au(111) wich had large pores, but there was significant variance in the number of molecules contributing to these pores, with anything between four and eight molecules forming each pore. This variation in pore size leads to long range disorder.

6.2 TBPB experimental setup

This work is follow on work from the studies performed in UHV by Blunt *et al* published in 2010 [137]. Progression from UHV to ambient conditions provides an analogous, but methodologically simpler, study, compatible with solution deposition and surfaces that are stable under ambient conditions [138].

The (111) surface of gold has been selected as an appropriate substrate as molecules featuring a benzene backbone have been shown to interact favourably with this surface [112, 137]. It provides the best compromise between inertness against ambient contamination and sufficiently high catalytic activity for the dehalogenation reaction. Gold preparation was performed using the plasma cleaning method described in section 3.1.2.

A series of solutions of TBPB in ethanol (Fluka, ACS Reagent grade $\geq 99.8\%$) were made, ranging from saturated solutions (0.8 mg/mL), down to 0.034 mg/mL concentrations. Ethanol has been chosen for the ability to dissolve the TBPB molecule in addition to being suitably volatile that the solvent will evaporate sufficiently quickly for the samples to be imaged dry. This removes the technical difficulty of performing STM in solution which, although possible, is far from ideal as it introduces additional concerns (see section 2.1.2).

Solutions were sonicated for 15 minutes prior to deposition to allow an even dispersion throughout the solution. 10 μL of solution was drop cast onto a freshly plasma cleaned gold on mica substrate using a micro-pipette. For experiments where the covalent coupling was desired, the substrate was heated to 200 °C on a hot plate in a fume hood, which had been left for 30 minutes to stabilize at the desired temperature. The temperature for heating the samples was set at 200 °C due to Fasel *et al* [122] achieving good linear polymerisation of bromonated compounds at this temperature, albeit they were working under UHV conditions. In room temperature experiments the volatile ethanol evaporated rapidly (approximately 1 minute),

resulting in a dried sample. For heated substrates the ethanol vaporised almost instantly. The substrate was allowed to cool before being scanned, once all visible solvent had evaporated. Allowing the substrate to cool before scanning helps to minimise image distortions caused by thermal drift during the scanning procedure.

STM images were acquired with an Agilent Technologies 4500 PicoPlus STM using a PicoScan controller and STM tips formed from mechanically cut PtIr (80:20) wire.

Images were analysed in WSxM [128] software and were plane fit to compensate for sample tilt, second order flattened to account for macroscopic variations in the surface, and histogram equalized to enhance visual contrast. Any images which received further processing will have it noted in their captions.

6.3 Results and analysis

6.3.1 Initial deposition structures

Before proceeding with aryl-aryl coupling, it is important to consider the morphology of the configurations the molecules will form as deposited. This can help us ensure that the coupling reaction has not activated at room temperature and confirm that the molecule has the desired geometry. The molecules as deposited on the surface appeared to form a protopolymer held together with halogen bonding and van der Waals interactions.

We initially reported the presence of three distinct phases, but this has since been revised to the two that are shown in Figures 6.4 to 6.6. The experimental observation of the coexistence of multiple distinct structures is indicative of the relative weakness and topological versatility of halogen-halogen interactions. Measurement of the lattice constants was performed using imageJ software [130]. Lengths were measured from center of void to

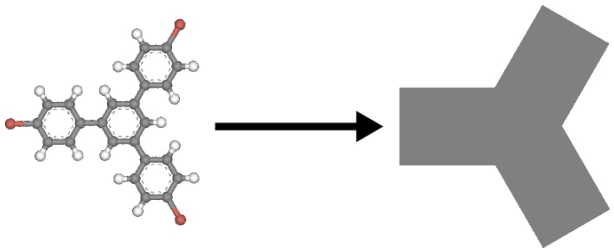

Figure 6.2: For the diagrams 6.4 and 6.6, the molecule will be overlaid with a grey box as shown above to highlight the geometry of the phases.

center of void, across as many repeat units as available in the image (errors are modified accordingly) and divided through to give the value for a unit lattice. The angle of the line with respect to the horizontal is automatically noted by the software when a length measurement is taken. The values of the lattice constants for the observed phases of TBPB are included in Table 6.1. It should be noted that the values in Table 6.1 are slight revisions to the values quoted in [138] following acquisition of additional data.

What was initially reported as "Phase 1" was the first phase observed and matches the image seen in figures in the UHV studies performed by Blunt *et al* [137]. It has been argued that this was the same structure as Phase 2 with the asymmetry caused by thermal drift, as first suggested in Blunt's work [137]. As the positioning of the alternate rows of molecules was halfway between the positions associated with Phases 2 and 3, the images labelled as Phase 1 could be of either phase dependent on the direction of drift. As a series of sequential images was not obtained for Phase 1 we were unable to determine the drift direction needed to perform a full drift correction (see Section 2.4). Examination of the relative lengths of the branches of the molecule reveal that there is some image distortion present. Further examination of samples, in an attempt to obtain a clearer image of "Phase 1" failed to do so over an extensive period, however Phases 2 and 3 were observed multiple times during these experiments. In spite of this, the two existing phases are still labelled as Phase 2 and Phase 3 in order to maintain consistency with other published work [138].

Phase 2 is shown in Figure 6.4 and appears to have a visually similar

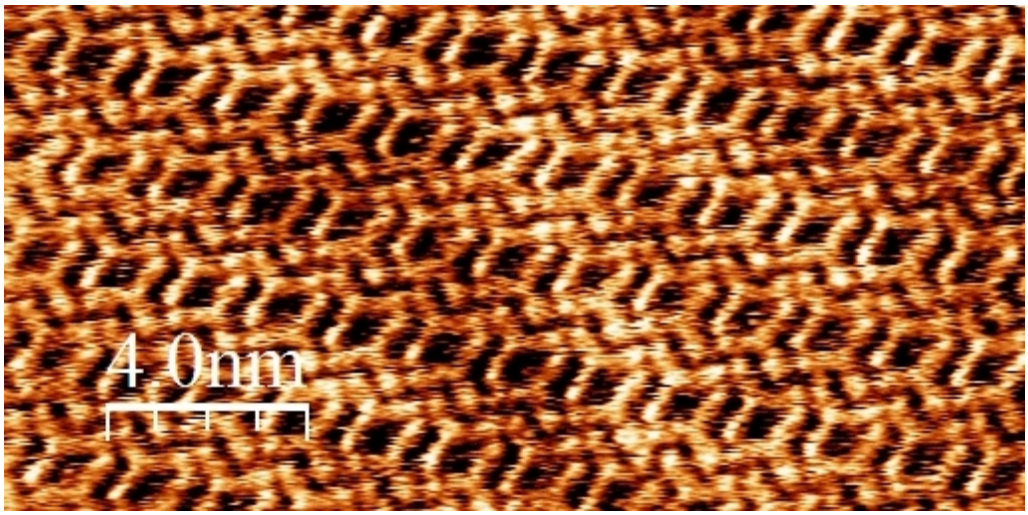

Figure 6.3: TBPB on Au(111)from ethanol. The image which appeared to be a unique phase labelled Phase 1. Further examination suggests this is a distorted image of Phase 2 with distortions due to thermal drift. The herring bone reconstruction of the gold can be seen through the layers of molecules as the lighter and darker regions of the molecules.

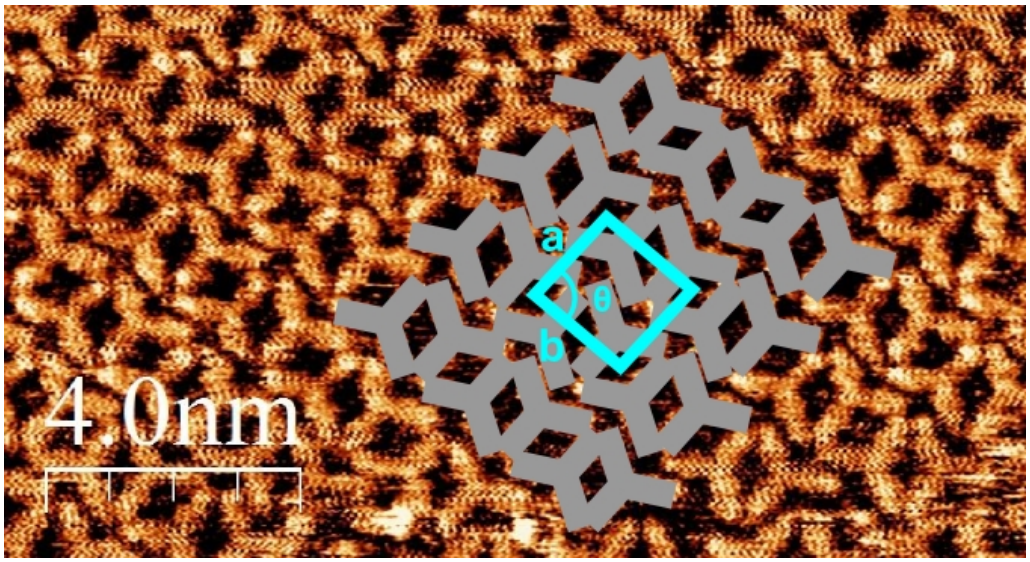

Figure 6.4: The structure of the second phase of TBPB. This image is from a sample made using a solution at 0.0685mg/mL. There is some high frequency noise present in the image, but the resolution still clearly shows the molecule. Imaging parameters were: set point 300pA, Set point 0.6V.

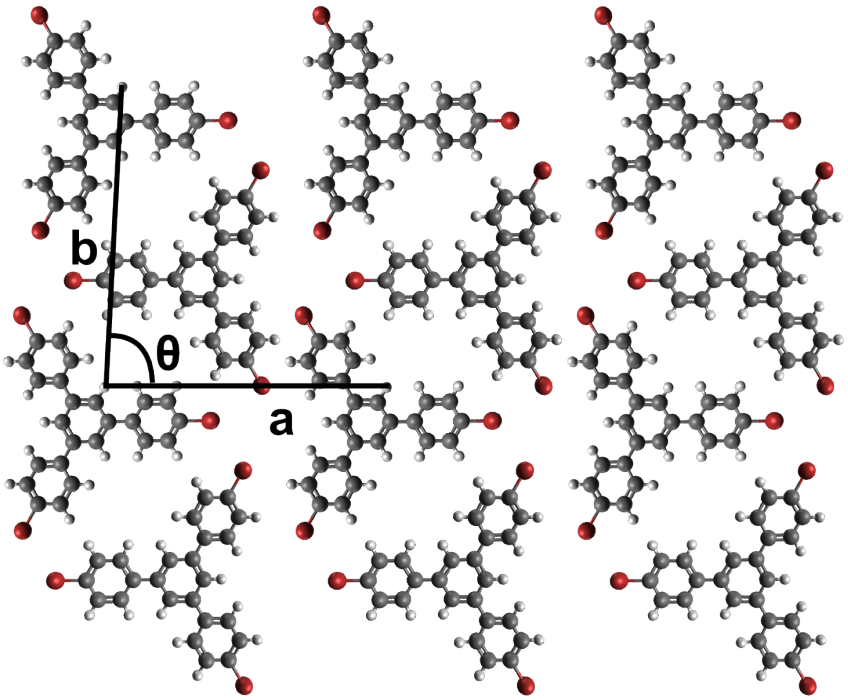

Figure 6.5: Molecular model of TBPB phase 2 deposited at room temperature on Au(111) from ethanol. Lattice parameters: a=1.65 nm±0.01 and b= 1.75 nm±0.01 with $\theta = 87° \pm 2$.

orientation of the molecules, to one of the structures that have been observed on Ag (111) by Walch *et al* [136]. On areas of the sample where only Phase 2 is present, surface coverage of Phase 2 is $(65.5 \pm 0.3)\%$. Phase 2 is the phase seen in the majority of STM images of the TBPB molecule obtained from drop casting solutions in ethanol. Due to the availability of additional data since publication of [138], the lattice values for Phase 2 have been revised. Due to the symmetry of the molecule within the image, it is possible to confirm that there is no significant drift distortion present by measuring the length of the branches of this molecule relative to the center, and checking that they are identical in length. The key way to identify Phase 2 is to look for 3 points of molecules meeting in a 'v' of another molecule. This geometry can be accounted for if we examine the electronegativities of the atoms involved. Bromine is more electronegative than carbon [110] which results in the bromine nuclei withdrawing electron density away from the rest of the molecule. As the TBPB molecule is a fully conjugated system, the electrons delocalize over the whole molecule, meaning this charge can be withdrawn from further than just the adjacent

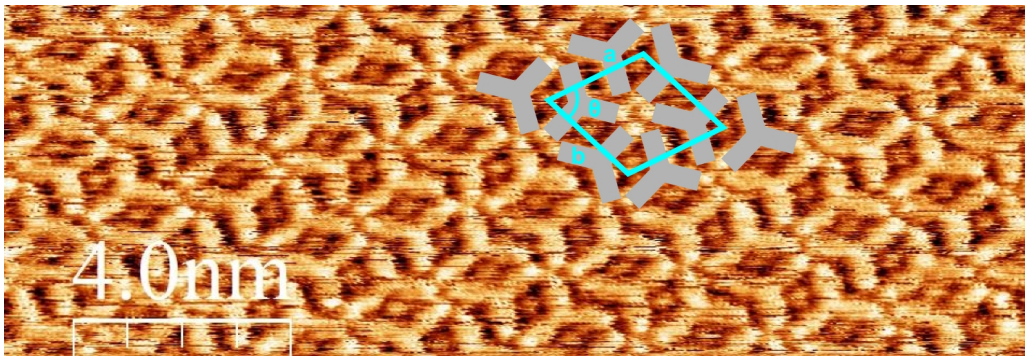

Figure 6.6: The structure of the third phase of TBPB. The key feature of Phase 3 is that 6 bromines meet at a point. Imaging parameters were: set point 500 pA, bias voltage 0.4V .

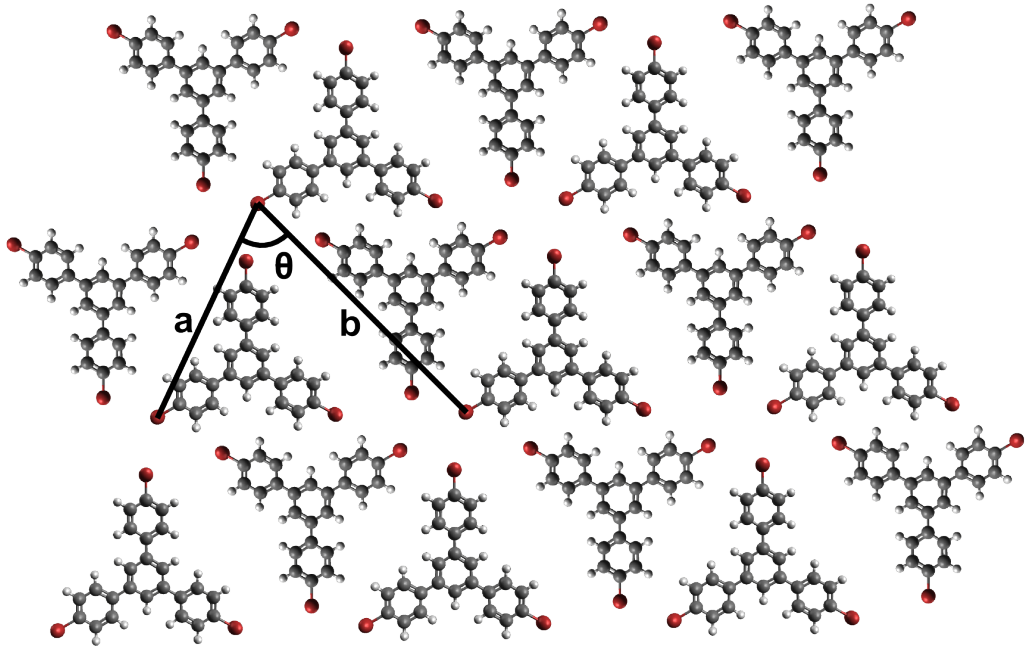

Figure 6.7: Molecular model of TBPB phase 3 deposited at room temperature on Au(111) from ethanol. Lattice parameters: a=1.76 nm±0.02 and b= 2.21 nm±0.9 with $\theta = 70 \pm 0.07$.

atom. This results in the molecule having a small permanent dipole with the tips where the bromine atoms lay having a slight negative charge and the central benzene ring having a slight positive charge. Bromine atoms attached to the nearest neighbour molecules are attracted to this partial positive charge, but are repelled by each other, which causes three points to line up in a 'v' equidistant apart and stabilizes the Phase 2 morphology by the formation of halogen bonds [139]. Note that this does not take into account specific effects of the surface or solvent in the network formation.

Phase 3 is much more rarely observed than Phase 2. Phase 3 features

Phase	a	b	θ
Phase 2	1.65 nm±0.01	1.75 nm±0.01	$87° \pm 2$
Phase 3	1.76 nm±0.02	2.21 nm±0.9	$70° \pm 0.07$

Table 6.1: Lattice parameters for TBPB phases

points from 6 molecules coming together. It was more commonly observed in depositions using butanol as the solvent. The coverage of molecules in images of Phase 3 has been calculated to be $(56.1 \pm 0.3)\%$. A careful examination of Figure 6.6 reveals a mismatching line laying along the b axis one molecule to the left of the ones highlighted in grey. Along this line, the orientation of the diamond shaped voids is rotated compared to the rest of the structure.

6.3.2 Concentration variation

It was proposed that a reduction in the concentration of the molecule within the drop cast solution of TBPB may lead to a more open structure, in a similar way to using lower vaporisation rates in vacuum studies has led to more open structures of other molecules .

For all drop casting at room temperatures, the same structures were observed as in section 6.3.1 and [138], however at lower concentrations it was notably more difficult to obtain any clear images of the domains of the adsorbed molecule. There was no change in the statistical preference for either phase morphology as a function of concentration, and both phases were observed at a similar frequency as to with the saturated solutions. As the molecules are mobile on the gold surface it is believed that they aggregate in such a way to maximise van der Waals interactions with each other. Therefore fewer molecules would lead to larger spaces between these domain islands, reducing the likelihood of bringing the tip down on top of a region of molecules as opposed to an area of clean substrate.

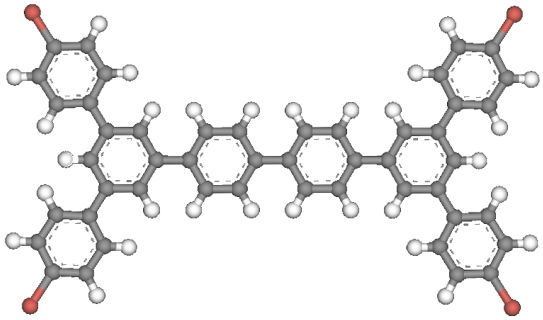

Figure 6.8: The structure of the TBPB dimer, $3,3'',5,5''$-tetra(4-bromophenyl)quaterphenyl (TBPQ)

6.3.3 Dimerisation

Dimerisation was achieved by drop casting solutions of TBPB onto pre-heated substrates (still using mica backed Au(111) at ambient conditions) which were held at 200 °C. Due to this temperature being far above the boiling point of ethanol, the deposition was performed in a fume hood. Substrates were allowed at least five minutes for temperature equilibration before deposition.

It can be seen in Figure 6.9 that pairs of TBPB molecules have undergone an aryl-aryl coupling reaction, which arises from cleavage of C-Br bonds on neighbouring molecules, followed by the formation of a carbon-carbon bond.

Rather than the complete polymerisation we had initially hoped for, the coupling appears to have terminated once two molecules of TBPB had bonded to form the dimerized product:
$3,3'',5,5''$-tetra(4-bromophenyl)quaterphenyl (TBPQ - see Figure 6.8). The length of the quaterphenyl backbone is determined to be 1.31 ± 0.1 nm, consistent with density functional theory computer simulations of TBPQ [137]

The morphology of the dimer on the surface matches what we would expect both sterically, due to the shape of TBPQ, and energetically. As the

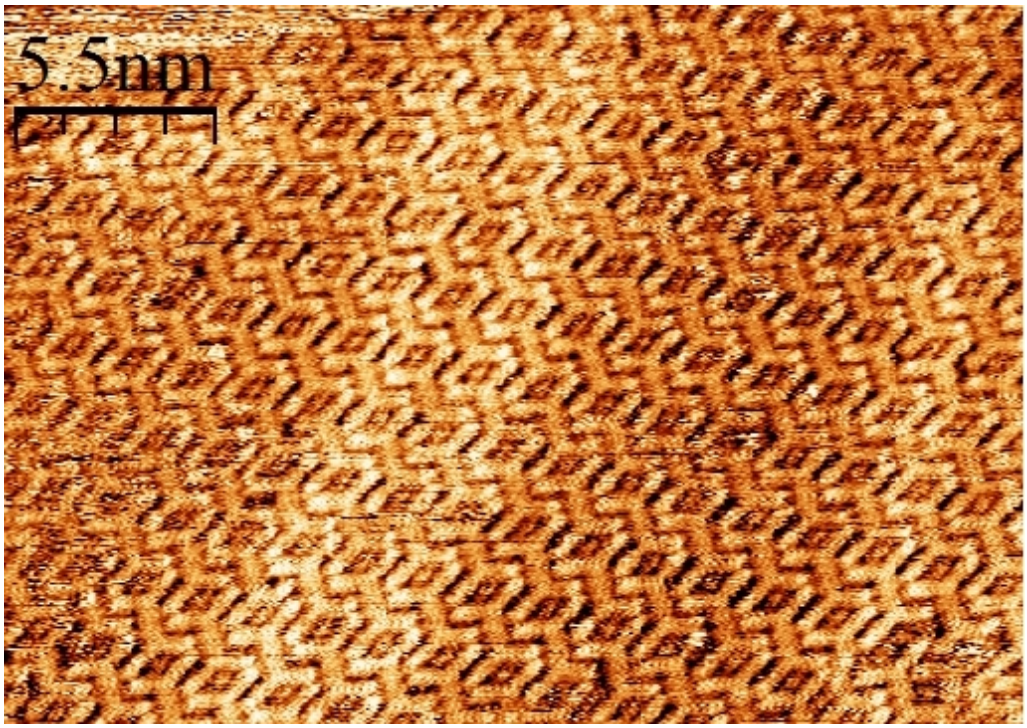

Figure 6.9: STM image showing the dimerised form of TPBP, $3,3'',5,5''$-tetra(4-bromophenyl)quaterphenyl (TBPQ). The herring bone reconstruction of the Au(111) substrate surface can also be seen as bright lines across the scan. Note the appearance of a feature between the dimer molecules believed to be trapped adatoms. Molecules were deposited from ethanol onto a substrate heated to 200 °C

position where the covalent linkage has occurred is now the furthest point in the conjugated system from the electron withdrawing bromine nuclei, the partial positive charge these bromine nuclei induce will relocate to this point. This allows the remaining bromine atoms on nearest neighbours to form halogen bonds with this electro-positive region around the newly formed bond.

Various solutions were suggested as to why the reaction had terminated at dimers and not fully polymerised. One suggestion was that we had only just reached the minimum activation energy needed to dimerise, and once that process was complete there was insufficient energy for the larger molecule to bond again. Blunt *et al* [137] observed progression from dimers to a multiply connected molecular network after further annealing. This hypothesis is also supported by the presence of an image where half of the molecules are in the dimerised form, and the other half in one of the close packed phases (Figure 6.11). There are one or two observed cases of trimers,

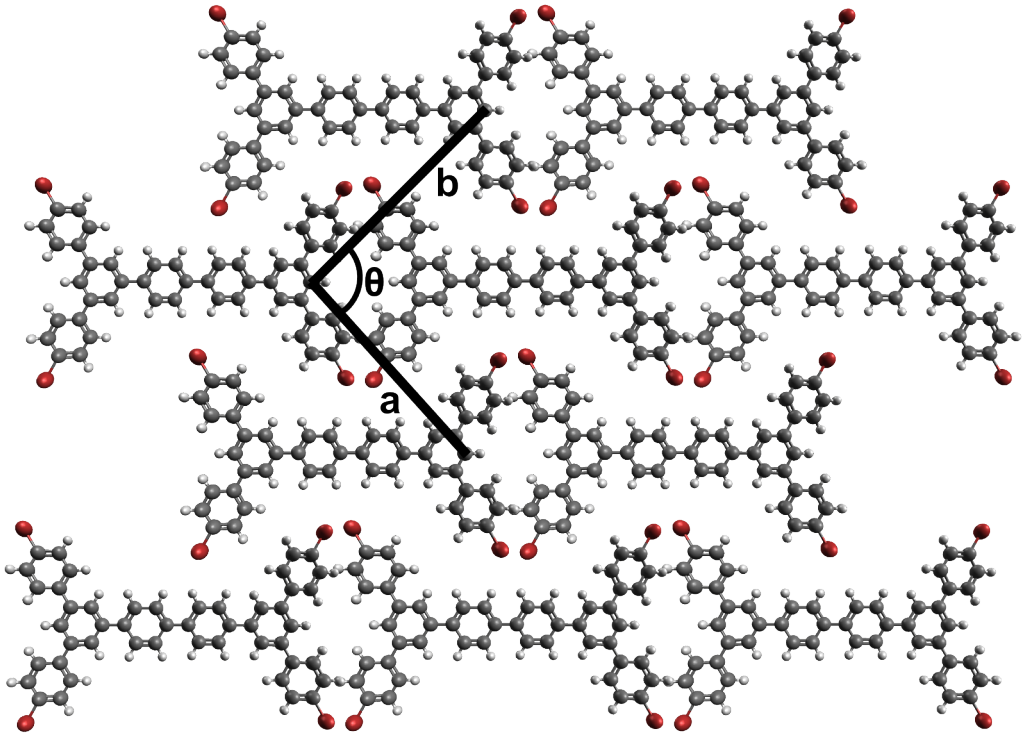

Figure 6.10: Molecular model of TBPQ formed when molecules of TBPB are deposited from ethanol onto an Au(111) substrate heated to 200 °C. Lattice parameters $a = 1.6 \pm 0.1$ nm, $b = 1.7 \pm 0.1$ nm, angle $\theta = 93 \pm 14°$

being attributed to to a minor localised temperature spike possibly caused by a defect in the underlying gold. All trimers that have been found are located at domain boundaries. To eliminate insufficient thermal energy as a possible solution, the experiment was repeated with deposition temperature of 250 °C.

We saw no change towards greater connectivity of molecules, only more images of the same dimer structure seen with depositions at 200 °C. This is contradictory to what was seen in UHV following further annealing of dimerised samples. This may be due to the bromine atoms being able to desorb from the surface in vacuum, which is not possible at the higher pressures of ambient conditions.

6.3.4 Discussion of dimerisation results

Examination of images of the dimers, such as Figure 6.9, shows that the molecules have formed dimerised pairs, and that all of those pairs lay in

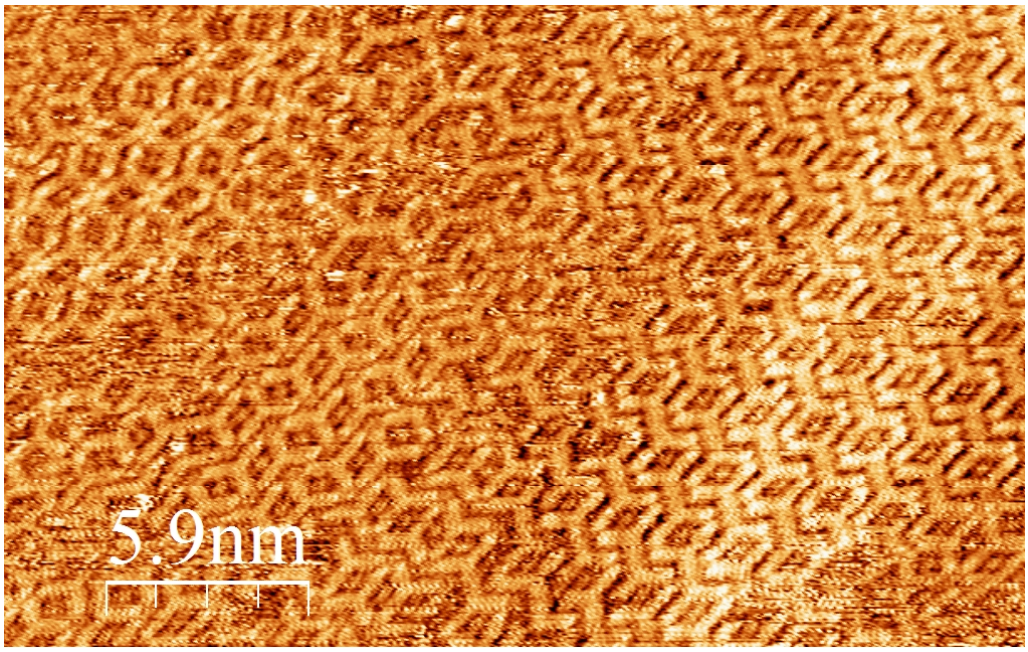

Figure 6.11: An STM image showing coexistence of TBPB close packed Phases 2 (lower left), 3 (upper left) and the dimerised form, TBPQ (right). An Au(111) on mica substrate heated to 200 °C is used for the deposition from ethanol.

the same direction for each domain. This suggests that there is something occurring which makes one direction preferable. If we compare the molecular models proposed for the phases of the unheated samples (Figures 6.5 and 6.7 we can see that Phase 2 (Figure 6.5) does not have any bromide pairs perfectly lined up with each other. If we allow for a small movement of the molecule to align bromide groups then there are two bromides on each molecule that are equally close to each other in Phase 2, which would suggest dimerisation would be equally possible in two directions leading to either a mixed phase with two dimer directions (separated by 60°) and possible zigzagged polymers. The polymerisation would require a lower surface coverage than what is observed experimentally and atmospheric pressure makes this unfavourable. In Phase 3 (Figure 6.7) each molecule has one other molecule it is perfectly aligned with. Once those initial bonds have formed, the other bonding groups are nowhere near any other bonding group for further polymerisations which agrees with the experimentally observed termination at dimers. This suggests that for the experiments performed here, that Phase 3 acts as an intermediary phase. If there was sufficient energy to desorb the dimer molecules into solution it should be possible

for larger polymers to form, however higher energies causes the solvent to evaporate more rapidly. A less volatile solvent may be an option for this but as we observed in Chapter 5, changing the solvent can have a dramatic effect on the network structure.

Origins of the bright feature observed between dimer molecules

A careful examination of Figure 6.9 will reveal a feature present between the forked ends of two neighbouring TBPQ molecules. This feature has been suggested to be caused by adsorbed bromine atoms, left over from the aryl-aryl coupling but still remaining adsorbed to the gold surface, however as these features are also present (albeit fainter) in scans of the unreacted monomers, this is unlikely to be be the case. Time of flight, secondary ion mass spectroscopy data (ToF-SIMS) from these samples obtained and analysed by J. C. Russell [138], show that, for room temperature deposition, bromine atoms remain attached to adsorbed TBPB monomers in over 95% of cases.

Another possible source for these features is a gold atom from the underlying substrate that has been raised up by interactions with the molecules. At the sites where we find these raised features the suspected gold atom is surrounded by 4 bromine atoms. Square planar complexes are common for gold if it is in the Au(III) state [140] and gold is known to form co-ordination complexes with bromine, however in those specific cases the bond angles between gold and bromine (along the Br-Au-Br angle) would be 87° [141] and not the much narrower angle we are seeing, therefore we can conclude that the gold atom is not forming co-ordinate bonds with all four of the bromides. Gutzler *et al* [78] attributed similar spherical features to single substrate atoms coordinate bonding to several bromides in their experiments on copper. Although they are not strongly bonding with any components of the molecule these features are most likely to be confined gold adatoms.

Although it was possible to go to even higher temperatures in an at-

tempt to obtain complete polymerisation, it was decided not to attempt this at the time due to safety concerns, we were approaching the autoignition temperature of ethanol, and the results from the previous temperature increase were sufficient to eliminate the effect of temperature as the problem.

6.4 Other related and future work

The same experiment was attempted using polycrystalline copper as a substrate. This was to recreate under ambient conditions some of the results seen by the Lackinger group in vacuum [78, 136]. After over two weeks of scanning at a variety of set points and tip biases, no resolvable trace of the molecule was detected in samples created by drop casting from solution in either ethanol or nonanoic acid.

Other follow on work, which took place in Nottingham, used a similar molecule with iodine in place of the bromine groups. They did succeed in generating small polymers but not a full uniform covalent network. The details of the work on 1,3,5-tri(4-iodophenyl)benzene (TIBP) can be found in [118]. Many of the suggested extension experiments we recommend for TBPB are also applicable to TIPB.

Some quick attempts at imaging were performed on 1,3,5-tri-(4-bromobiphenyl)-benzene, which has longer branches and should lead to larger pores, but as initial trials showed poor solubility in ethanol and no successful imaging it was put to one side. A proper solvent selection trial is needed and the TBPB work should be repeated using the suitable solvent for the biphenyl form, once it is found.

As solvent polymorphism has been observed in other self assembled structures (such as the hydrogen bonded TPTC networks discussed in Chapter 5) it would be interesting to see if the structures formed by adsorbed TBPB were similarly affected by a change of solvent. A change to less volatile solvents, such as phenyl-octane or nonanoic acid, would require a

transition from dried samples to full liquid STM imaging.

A few brief preliminary experiments were performed using a solution of TBPB in ethanol (the same solution which gave the main results in section 6.3 on gold)on a polycrystalline copper substrate. No clear images of the molecules were obtained. More work is required to obtain suitable scanning parameters for the new substrate before making any firm conclusions. It is also possible the polycrystalline nature of the substrate was a problem, and the experiment should be repeated on single crystal thin films of copper.

To further the temperature experiments, samples where full coverage of dimer molecules have been prepared should be further annealed under an argon atmosphere to see if this promotes further linkage. Further linkage has been seen previously in UHV studies by Blunt *et al* [137], although in that work the networks formed were highly disordered.

6.4.1 DiBromo-BiAnthryl experiments

Some preliminary work was carried out on the molecule 10,10'-dibromo-9,9'-bianthryl (DBrBA) expanding from the work by Fasel *et al* [122] in vacuum. The transition from UHV to ambient conditions introduces the requirement for an appropriate solvent. The solubility needs to be sufficient for the molecule to become mobile in the solvent, yet low enough for it to be energetically favourable for the molecule to come out of solution and adsorb to the substrate surface.

Solubility tests for DBrBA were carried out in toluene, nonanoic acid and ethanol. Solutions were ultrasonicated for 30 mins and then allowed to settle overnight. All three solutions were made with the amount of powder required to make a 1 milimolar solution, however not all of the powder fully dissolved in any of the samples, resulting in three over-saturated solutions. Out of the three solvents used, toluene was the most effective solvent at dissolution of the powder, and ethanol was the least effective. This result

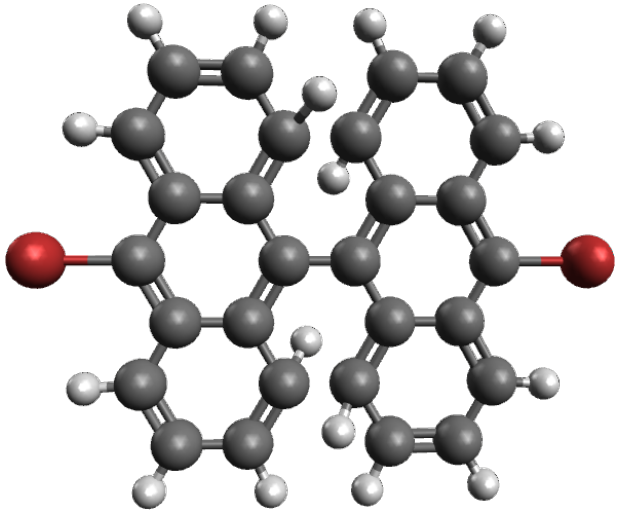

Figure 6.12: A model of the chemical structure of 10,10'-dibromo-9,9'-bianthryl (DBrBA). Hydrogen atoms at the central row are expected to angle out of the plane. Model created using Avogadro Free cross-platform molecule editor [142].

led to the selection of the 1 mM DBrBA in toluene solution for the STM experiments.

Samples were made by applying a 10 μL droplet of 1 mM solution of DBrBA in toluene (HPLC grade, 99.9%, Sigma-Aldrich) onto flame annealed substrates of 100 nm Au (111) on Mica. The droplet was blown off with nitrogen gas after 2 minutes dwell time. STM imaging of samples was performed using an Agilent Technologies 4500 PicoPlus STM using a PicoScan controller and STM tips formed from mechanically cut PtIr (80:20) wire. A set point of 0.04 nA and a bias voltage of 0.7 V were used to obtain the images of these samples.

The image in Figure 6.13a shows molecules of DBrBA in a similar configuration as the image from Fasel *et al.* There is some drift present in the image which causes the discrepancy in the size of the molecules. Unfortunately it was not possible to obtain a clear enough sequence of images to compensate for this drift (as discussed in section 2.4).

After the initial sample, from which Figure 6.13a was obtained, other samples prepared in a similar way did not yield images of any molecular structure. We linked this low success rate to the molecules being confined to small islands, in the same way we had seen for low concentration of

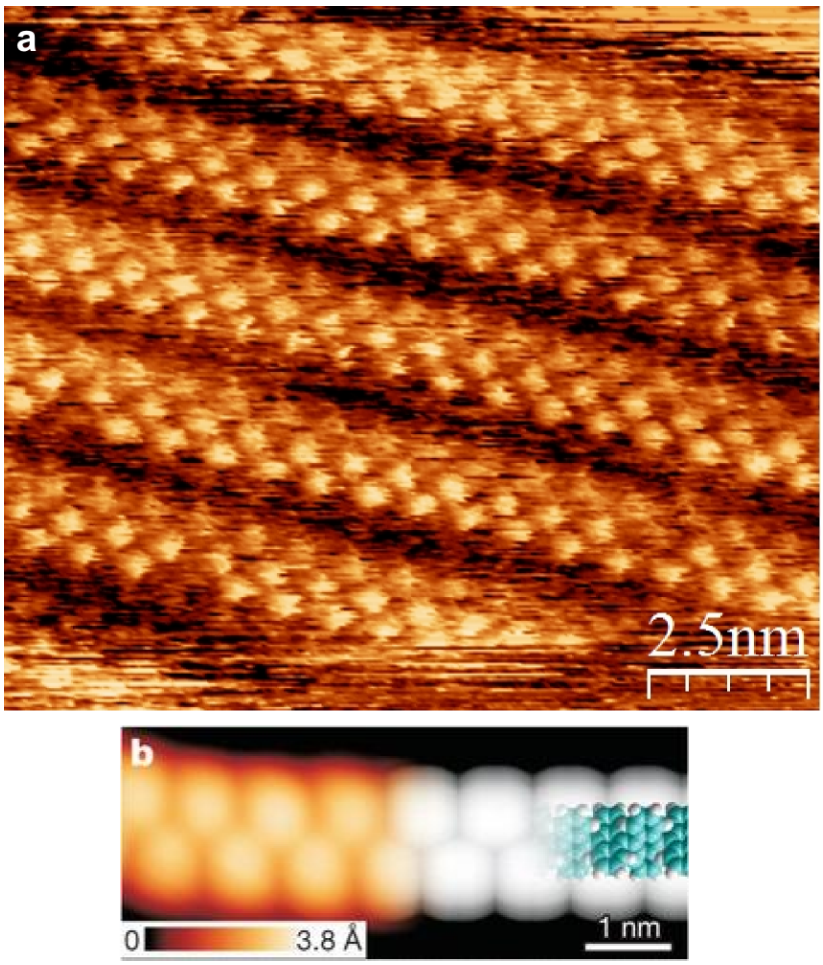

Figure 6.13: a) STM image of DBrBA on Au(111) from toluene and b) Image from Fasel *et al* [122] showing the same molecule in UHV with overlaid simulation

TBPB. To counteract this, additional solutions were made up in toluene at the higher concentrations of 2 mM and 4 mM to see if the presence of more powder would shift the dissolution equilibrium towards allowing more of the molecule to enter solution. STM scans of drop cast samples made from these solutions did not show any observable structure.

Optical study

Optical microscopy investigation of these samples was undertaken to try and understand what was happening to the molecules on the surface on a larger scale.

For the 4 mM solution it was clear that the coverage of the surface was far higher than monolayer, with visible thick amorphous aggregations, which would have led to difficulties in obtaining good conductance from the surface.

On samples where the 1 mM and 2 mM solutions had been drop cast it was noticed that there were dark drying rings around where the droplet had landed. Although the droplet was blown off using nitrogen gas, some of the solvent does evaporate during the two minute dwell time, resulting in some drying rings at positions towards the outer limits of where the droplet had initially covered. Closer investigation of these dark drying rings revealed dendritic aggregations as shown in Figure 6.14. The 2 mM solution had more of these aggregations between drying rings, but their density was significantly higher at the ring locations. Similarity can be seen between the dendritic structures in Figure 6.14 and structures observed in work by Pauliac-Vaujour *et al* [143]on dewetting of Au-Thiol nanoparticles in toluene.

A change to immersion of the substrate in the selected solution yielded no better results and imaging with STM was unsuccessful. An optical examination of the sample revealed similar structures to those seen in Figure

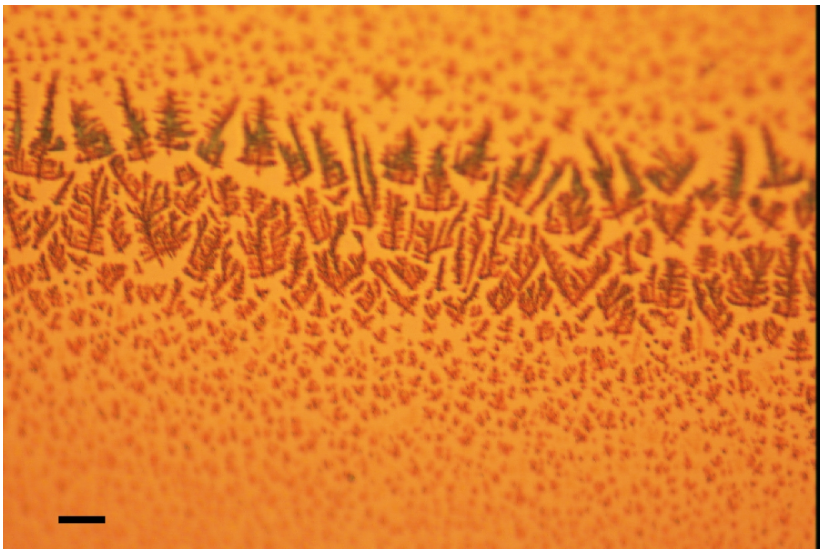

Figure 6.14: Optical image of dendritic features on a sample where 1 mM DBrBA in toluene has been drop cast onto Au (111) and blown dry with nitrogen. Scale bar is 10 μm.

6.14 but smaller in size and more evenly distributed across the sample area.

From this we draw the conclusion that DBrBA has insufficient solubility in the solvent toluene for reliable monolayer depositions. We either require an alternative solvent or the addition of an emulsifying agent.

Covalent linkage attempts

Attempts to covalently link the molecules of DBrBA were performed. The hot plate used in the experiments described in section 6.3.3 was incapable of reaching the temperature of 400 °C that Fasel *et al* [122] used for their cyclodehydrogenation step. We instead utilized a tube furnace for our annealing step where the sample was held under a flow of argon at 100 standard cubic centimetres per minute (sccm). Samples were prepared by both drop casting and immersion of DBrBA in toluene, in order to compare the two methods. Only one sample could be annealed at a time.

The sample was loaded into the tube and the argon flow initiated. Heating started after four minutes of argon flow, to displace any oxygen from within the tube, which would have resulted in oxidation and breakdown of the molecule. Once the temperature within the tube had reached 200 °C

it was held there for 10 minutes before being cooled and then removed for examination. It was assumed that any excess molecule would become either desorbed in the annealing process or form a second covalent layer on top of the first.

Our examination at this midpoint did not show us what we had expected, in fact the Au(111) surface appeared indistinguishable from one where there had been no molecular deposition. This was the case for both deposition techniques.

In hindsight it would have been better to use the hot plate for the initial covalent coupling reaction (as we did for TBPB), and then utilizing the tube furnace for the cyclodehydrogenation step, if the coupling had yielded positive results.

We also attempted to scan the solution of DBrBA in nonanoic acid. All of our scans appeared to feature large white objects, appearing similar to how one would expect a spec of dust to appear on an STM image. This suggests the powder has remained as a suspension of particles consisting of agglomerates of the DBrBA molecule, rather than becoming a solution. A more appropriate solvent is required before further work can be done on ambient studies of this molecule.

6.5 Conclusions on covalent networks

We have demonstrated a solution based approach to the formation of large molecules and nanostructures by covalent coupling reactions with the example of 1,3,5-tri(4-bromophenyl)benzene. Although complete covalent polymerisation was not observed, we have seen indications that it may be possible once experimental conditions have been optimized. We have also demonstrated a concentration independence of the structure of room temperature depositions of TBPB. Our experiments on 10,10'-dibromo-9,9'-bianthryl highlight the need for careful selection of carrier solvent.

Chapter 7

Graphene Synthesis and Related Experiments

Graphene growth has been attempted by many different methods over the last ten years by numerous research groups around the world. The discussions in this chapter concern the methods we attempted using nickel as a catalyst for graphene crystal growth. Much of the work in this chapter was performed jointly with L. M. A. Perdigao.

7.1 Development of graphene growth by nickel catalysis

Growth of graphene by transition metal catalysis has been examined by many groups over the years with a recent increase in interest [67, 144–152]. Of all the metals used for the catalysis of graphene growth, nickel has the advantage of having a very good match in the lattice spacing with graphene [149] along the (111) plane (0.252 nm spacing for Ni (111) [153] compared to 0.246 nm for graphene [44]).

Carbon feedstock for the graphene growth on transition metal catalysts

often involves gas injection CVD of methane, or short chain alkenes [154–156].

Carbon thin film growth can be result of the breakdown of adsorbed molecules, or segregation of carbon from the bulk of the nickel metal. Segregation occurs when the carbon atoms are more strongly bound on the surface of the metal than they are within the bulk. This can be explained by the energy released by formation of carbon-carbon bonds between surface carbon atoms such as would be required to form graphene. If the energy released by the formation of these bonds is greater than that required to overcome the carbon-substrate interaction then layers will form on the surface. However if the carbon-substrate interaction is too weak then the carbon will rise to the surface and may evaporate off before these bonds have had a chance to form. As such the annealing temperature is a very important parameter, the carbon dopant atoms need sufficient energy to move through the host crystal, but insufficient energy to escape from the surface. Upon cooling, the movement of the carbon is increasingly restricted which leads to non-equilibrium segregation. As the sample cools the ability of the carbon to diffuse through the nickel decreases. If the sample is cooled too fast the carbon atoms are forced to remain in place. With a slower cooling rate the carbon will attempt to reach its equilibrium position, which leads to a wider spread throughout the bulk. Carbon has been shown to have a high solubility within nickel metal [151] (upto 1 atomic % [157]), and carbon formation on nickel surfaces though equilibrium segregation has been observed before [150].

Previous work in the literature has used both nickel cut from commercially available rolled sheets [155, 158, 159], and alternatively thin layers of nickel deposited by physical vapour deposition (PVD) on silicon oxide [154, 160].

Obraztsov *et al* suggested a mechanism for graphene formation on polycrystalline nickel where any grains where the Ni (111) surface is exposed acting as nucleation sites for graphene growth [155]. Obraztsov *et*

al's mechanism eliminates the need for expensive single crystal substrates, with Ni(111) grains initiating the growth which expands and continues over grain boundaries onto other crystal faces. They also mention creases forming in the graphene film which they attribute to the difference in thermal expansion coefficients of graphite and nickel.

The key to forming a monolayer is a fine balance between the nickel thickness, the annealing time and the cooling rate of the process. Other groups had reported that the optimal cooling rate after the nickel anneal was 10 $^{\circ}Cs^{-1}$ [154, 158], yet we found this rate was too slow and samples using this rate were forming thick multilayer carbon films.

One major drawback with a nickel based growth method is that certain characterisation techniques for the graphene films and many projected applications require the graphene to be on an insulating substrate. This has led to the need for development of a method of transference from the nickel catalyst to other substrates such as silicon oxide. The transfer method we used is described in section 7.2.

7.1.1 $NiSiO_2$ series

Initially our samples were prepared with the nickel deposited by physical vapour deposition (PVD) using a standard commercial evaporator [161] with a base pressure of $10^{-6} - 10^{-7}$ mbar for thermal sublimation. Following this, the samples were removed to a separate vacuum chamber with base pressure 5 x 10^{-10} mbar for annealing. In order to gain more control and to address concerns about the origin of the carbon, we moved to combining both processes into a single vacuum chamber.

The silicon oxide substrates we used were boron doped p-type (100) wafers supplied commercially from Si-Mat [162]. Wafers were 600 ± 25 μm total thickness with a 300 nm thermal oxide on each side. The resistivity of the wafers was guaranteed to be less than 0.0015 Ω cm. After scribing

the wafer into 10 mm by 6 mm sections, there was a considerable amount of dust left over around the edges. This was rinsed off with cleanroom grade isopropyl alcohol (IPA) and then blown dry with nitrogen gas.

Once the substrates were loaded into the evaporator they were left for several hours while the chamber pumped down to 2x10^{-7}mbar. The nickel evaporation proved tricky, as it is not just a case of turning the heating current to a set point and waiting, the current needs to be increased until some deposition is detected then slightly reduced, otherwise the rate continues to increase dramatically, and the transition can be quite sudden. If the heating current is increased too quickly the nickel can corrode through the heating boat. A quartz crystal microbalance measures the thickness of nickel deposited and is accurate to the nearest 0.1 nm, however achieving a specified layer thickness with this precision is difficult as the closing of the shutter, although quick, is not immediate. After nickel deposition the sublimation current is gradually decreased and the samples are left for 20 mins to cool before venting.

Once the samples are removed from the metallisation chamber, they are moved into a second vacuum chamber to be annealed. The sample holder is mostly made from non-conducting macor ceramic, with a conducting base plate, clamps, and screws. The annealing sample holder can only mount one sample at a time, where the metallisation chamber can hold several. A small heating filament of highly boron doped Si (111) with resistivity of $<10^{-3}$ Ω is clamped beneath the sample. When loaded into the annealing chamber, two electrical contacts are brought into contact with the back to the sample holder allowing a current to flow through the Si (111) filament, heating the sample. The samples were outgassed at 500 °C for 12-18 hours before a shorter anneal at a higher temperature for 15 minutes (exact temperatures are discussed in the results section of this chapter). Heating current was reduced to zero gradually over 15 seconds. All temperatures were measured externally with a pyrometer at incidence to the viewing window.

It is important to note with this method that there is no addition

of a carbon containing compound. It was discovered that the source of the carbon for the growth of graphene films was due to adsorbed carbon on the silicon substrates prior to the nickel deposition. Due to the high solubility of carbon within nickel metal, this carbon was able to diffuse into the nickel layer during the annealing process and upon cooling would become segregated to the surface, forming graphene. In order to gain greater control of the process we need to remove this carbon from the silicon while under vacuum, and deposition and annealing must both take place *in situ*. This has led to the development of the next method.

Propylene carbon source

The carbon feedstock of choice is propylene gas. Propylene is one of the simplest sp^2 carbon systems, and as it is readily available in pressurised gas cylinders, it can easily be injected into the vacuum system. Our vacuum system consists of a load-lock and two main sections, a metallisation chamber and an annealing chamber. The load-lock is pumped by a scroll-backed turbo molecular pump, whereas both the metallisation and annealing chambers are pumped by ion pumps and titanium sublimation pumps.

Silicon substrates are initially loaded into the sample holder which is blown with N_2 gas before entering the load-lock. The load-lock is then pumped down using the scroll pump until the turbo back pressure is less than 5 x 10^{-1} mbar, at which point the turbo pump can be activated. After approximately 2 hours, the load lock will have reached a pressure of order 10^{-8} mbar (although there is no pressure reading within the load-lock, only at the back of the turbo) and the sample is moved into the annealing chamber. The silicon oxide is then annealed at 800 °C (whilst keeping the pressure below 5 x 10^{-6} mbar) until the pressure at this temperature is below 5 x 10^{-7} mbar, typically taking 12-18 hours.

The nickel in the metallisation chamber sits within a quartz crucible, which is gently heated with a tungsten filament and allowed to outgas for

10 minutes before nickel deposition onto the SiO_2 is due to start. After 10 minutes the substrates are moved from the annealing chamber into the metallisation chamber, but are kept in such a position where they are not exposed to the nickel source. The rate of nickel deposition is measured by a quartz crystal microbalance, which assesses the rate of deposition by the effect of changing mass on the resonant frequency of the quartz crystal. Once this rate has stabilised to close to 0.02 nm s^{-1} the sample is moved into position and deposition begins. The voltage to the quartz crucible needs to be constantly adjusted in order to maintain a uniform deposition rate. Once the desired thickness is reached the sample is moved out of line from the nickel source and the effusion cell needs to be cooled slowly, as a rapid cooling tends to trigger a rapid increase in sublimation rate.

Following nickel deposition the sample is left to cool overnight and then moved back to the annealing chamber. The propylene cylinder is used to fill a gas line (rather than being directly exposed to the vacuum) which is purged and refilled before use. The sample is heated to the desired annealing temperature and allowed to stabilise before propylene exposure. Propylene is bled into the system so that the pressure in the top chamber reaches $1.0\text{x}10^{-6}$ mbar. After 20 mins of propylene exposure the bleed valve is closed and cooling begins.

C_{60} carbon source

Some experimentation was performed using fullerene (C_{60}) as a carbon feedstock for the graphene synthesis process. Fullerene is a source containing only carbon atoms, many of which are already in the sp^2 hybridised form seen in graphene, and C_{60} has been shown to decompose on a nickel surface [163, 164]. For sample growth the C_{60} is sublimed from a Knudsen cell within the same vacuum chamber that the nickel deposition is performed. C_{60} is deposited typically half an hour after the nickel deposition has finished. Following C_{60} and nickel deposition, these samples are annealed *in situ* at 700 °C for 15 minutes.

7.1.2 NiHOPG series

Another variation of the growth process uses highly oriented pyrolytic graphite (HOPG, see 3.1.1) as both a substrate and a carbon source. Freshly mechanically exfoliated HOPG is loaded into the high vacuum sample holder and loaded for nickel deposition. After nickel deposition the sample is annealed *in situ* with temperatures and times comparable to the other methods we have used. The intention here is that during annealing the top layer of graphite will diffuse through the nickel layer and reform on the nickel surface. There is no problem of extra hydrogen atoms which may prevent linkage and no need for any additional gas lines into the annealing chamber. The disadvantage with this method is that it is likely to produce multilayer if annealed for too long.

7.1.3 NiSapphire series growth

A few samples were grown using sapphire as a substrate. Nickel deposition was performed on the hexagonal symmetry of the (0001) plane (C plane) of a 0.43 mm thick wafer. The sapphire samples appeared to be slightly more delicate than the silicon oxide ones, with several breaking while being removed from the annealing chamber. The sapphire substrates did not take the nickel as well as the other substrates, with large deep holes appearing in the nickel. Due to the appearance of these holes (as shown in Figure 7.2) work on sapphire was discontinued.

7.2 Transfer process

This section describes the basic transfer method utilized to transfer the graphene grown by nickel catalysis on both SiO_2 (using a feeder gas) and on HOPG (with the carbon diffusing through the nickel to form a monolayer) samples. Iron (III) chloride is used as the etchant, as it is a standard etchant

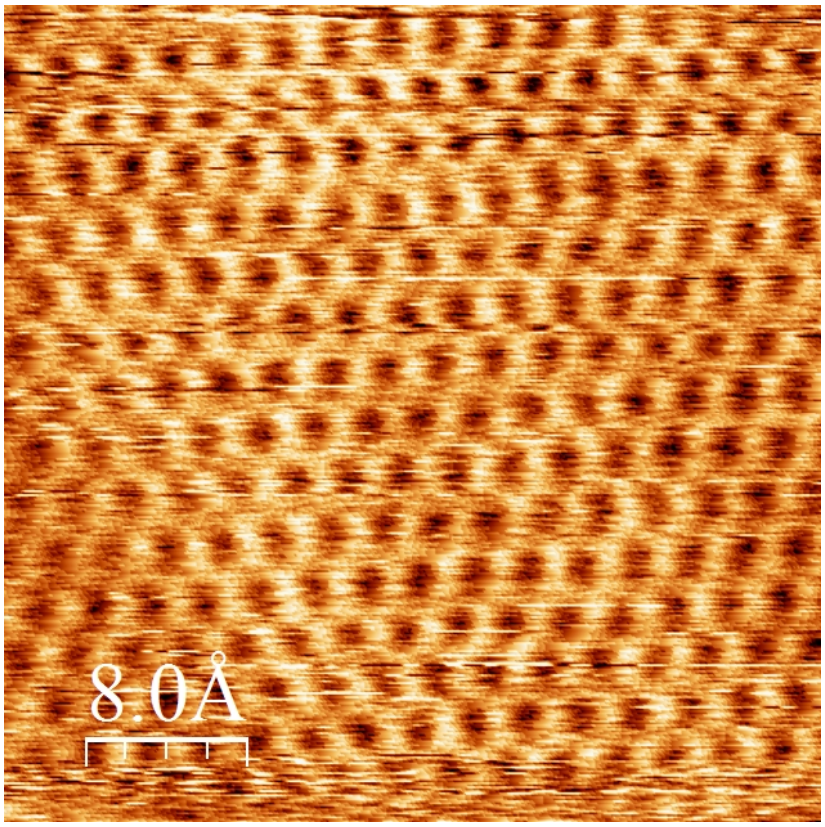

Figure 7.1: STM image of graphene grown on sapphire using propylene as a feedstock. Care was taken to find a flat region of the sample away from the deep pits that can be seen on the AFM image.

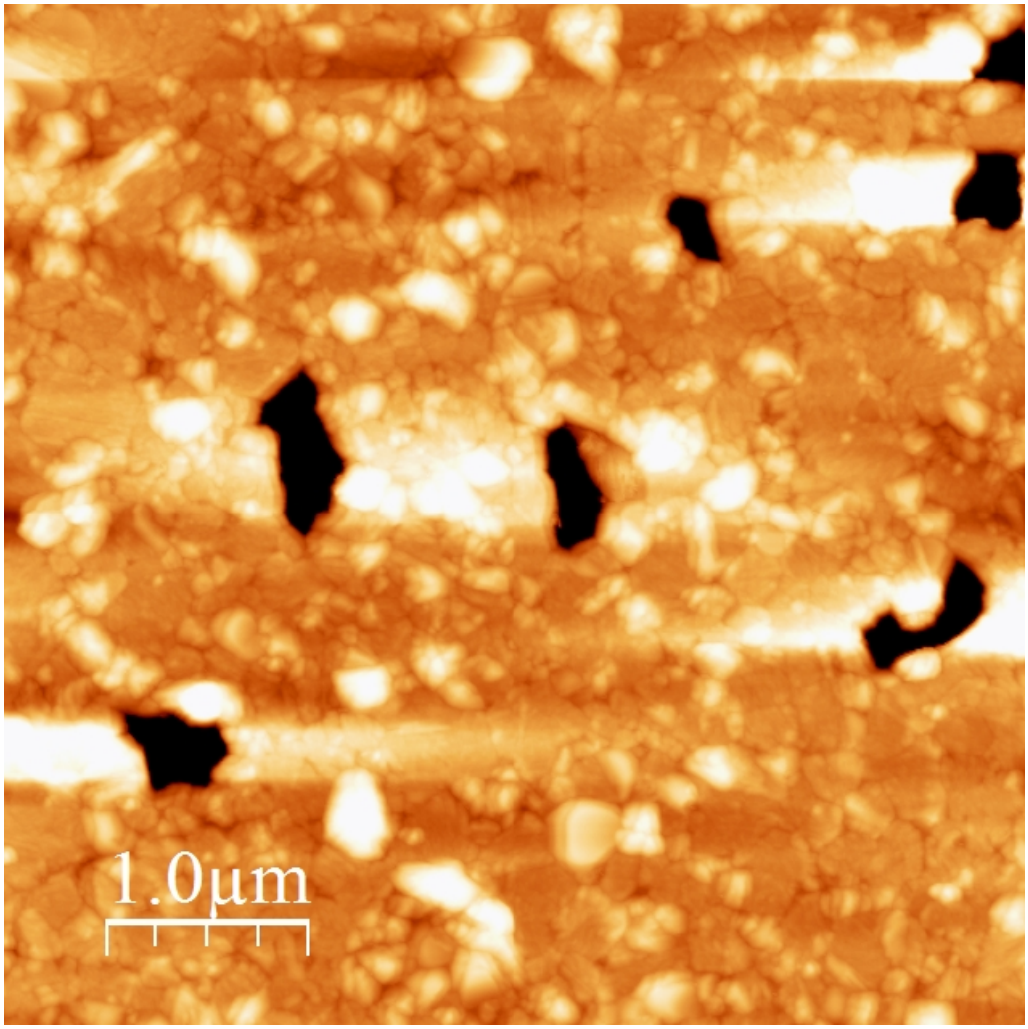

Figure 7.2: AFM of Ni on Sapphire. Note the deep holes (black areas) within the nickel layer.

used for etching copper in the production of electrical printed circuits [165] and known to work on nickel [166]. Variations to this method are discussed later in section 7.4.2.

All glassware is cleaned with deionized water, ethanol, acetone, methanol, isopropanol and blown dry with nitrogen gas before use. Samples are spin coated with 45k molecular weight poly- methylmethacrylate (PMMA) at 3000 rpm for 40 seconds. The PMMA is from a 5% solution in the solvent anisole supplied by MicroChem Corp. [167]. After spinning, the samples are heated to 180 °C for 2 minutes on a hot plate to drive off the remaining solvent and harden the PMMA layer. This PMMA layer is quite thin (approximately 250 nm [168]), therefore to improve the ease of which it can be manipulated it is then coated in a layer of poly-dimethylsiloxane (PDMS). This layer is then cured in a convection oven at 150 °C for 10 minutes. Once the PDMS has been cured a scalpel (cleaned in the same way as the glassware) is used to cut away the PDMS from the sides of the base substrate in order to expose the Ni at the sides of the stack. The nickel is etched away with 1 mol dm^{-3} $FeCl_3$ solution made up from powder (>97% Sigma-Aldrich) using deionised water from our in house system. The $FeCl_3$ solution is filtered using grade 1 Whatman filter paper before use. This purity of iron (III) chloride is being used since previous less pure etchant had revealed copper contamination. This etching process takes several hours depending on the size of the sample, a 10 mm by 6 mm sample which has been properly exposed takes around 6 hours but they are usually left overnight.

Following the etching, the polymer stack (PDMS +PMMA +graphene) is removed from the $FeCl_3$ and excess $FeCl_3$ is rinsed off with deionised water. The polymer stack is then left floating on the water where the desired substrate (typically SiO_2) is brought in underneath it and used to it lift out. At this stage there is a brief thermal cycle to dry off any water that is between the graphene and the substrate. This involves 10 minutes in the convection oven at 100 °C. Next the PMMA layer is dissolved using an isoclean acetone soak, which also causes the PDMS to drop off leaving

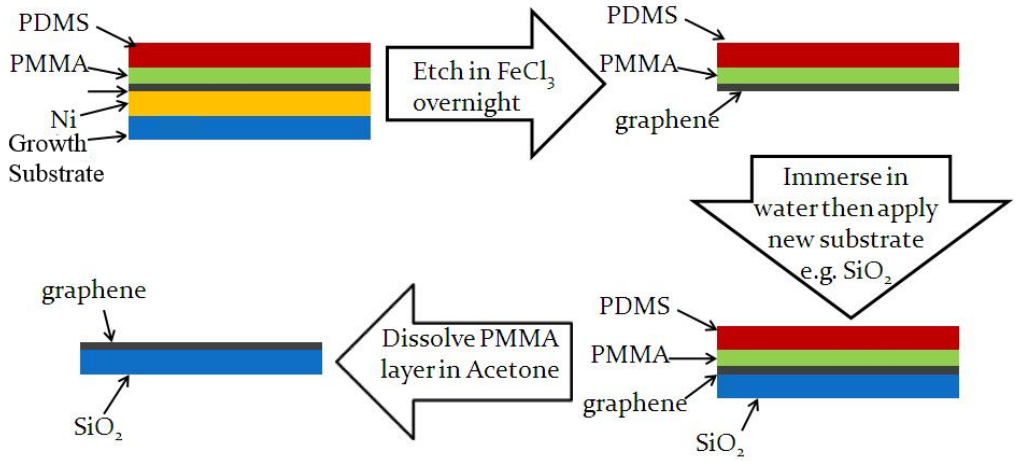

Figure 7.3: The transfer process for moving graphene from a sacrificial nickel think film to an SiO_2 substrate.

only the new substrate with the graphene layer on top. As acetone has been known to leave a drying stain the acetone is rinsed off using isoclean isopropanol and then the surface is blown dry with nitrogen.

7.3 Sample characterisation

We characterise the sample at several stages during the growth process. Initial examination of the nickel films was performed using atomic force microscopy (AFM) to determine nickel grain size, as this was predicted to have an effect on the resulting graphene films. In samples where the growth and anneal was performed in separate vacuum system the samples were characterised before and after anneal. For samples where the annealing was performed *in situ* the grain size was only measured post-anneal.

There are several methods for characterising graphene layers on surfaces. STM is suitable for graphene on flat metallic substrates, Raman spectroscopy works well on any non-metallic substrate, however with our samples Raman is not possible due to the fact the Raman activity of the metals swamps out any signal in the same region of the spectra as our adsorbed graphene layers. Finally graphene can be seen optically on certain thicknesses of silicon oxide due to an interference effect and the high optical

absorbency of graphene [169, 170].

7.3.1 Optical characterisation of graphene

Optical microscopy is the method used initially to determine the presence of graphene on a sample post-transfer. Silicon oxide samples with certain thicknesses of the oxide layer provide sufficient contrast to identify graphene layers due to an interference effect [170]. A silicon oxide thickness of 300 nm was the benchmark for optical characterisation of graphene for some time [169] and is the thickness we initially used as a sample substrates. Following the publication of work by Blake *et al* [170] we changed to using a 90 nm oxide thickness SiO_2 as the target substrate recommended by that paper to improve graphene contrast. Both oxide thicknesses have good contrast for the sample in green light.

Two different optical microscopes were used for the characterisation at various stages of the project, an Olympus BX51 and a Leica DM2500M. Both microscopes were operated in bright field reflectance mode. An exposure time between 40 and 60 ms was used for image capture. Optical characterisation provided a qualitative indicator of a successful transfer process, with further characterisation of the quality of the film to be carried out subsequently using Raman spectroscopy.

7.3.2 Raman spectroscopy for graphene characterisation

Raman spectroscopy is the main quantitative method for determining the quality of the graphene films we produce, providing us with a guide to grain size, defect density and number of layers present. It is a non-destructive, non-contact, high throughput method of characterisation. A typical spot size for the laser would be ~ 2 μm [160]and the spectrum represents the total signal from the area under the spot.

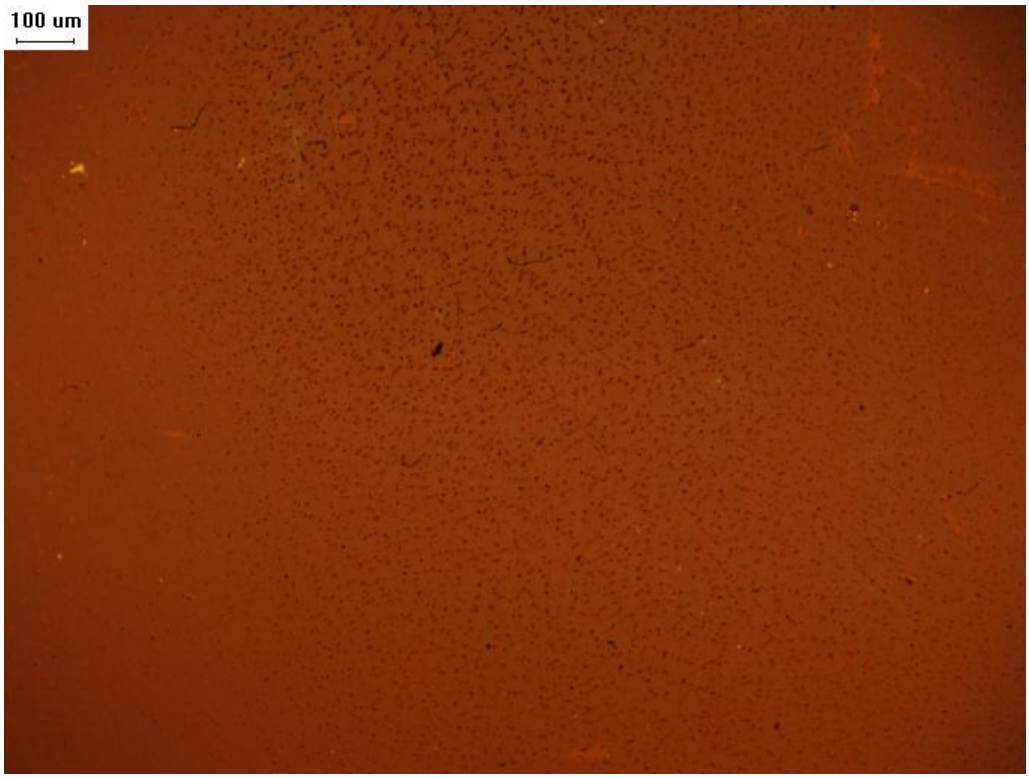

Figure 7.4: Optical image of graphene on SiO_2 grown by the sacrificial nickel thin film method. The dark dots in this image are believed to be iron oxide microcrystallites left over from the etching process.

Whenever a photon encounters a molecule there are several outcomes which can occur. If the photon energy corresponds exactly to the separation between states in the electronic, vibrational or rotational structure, the photon will become absorbed, leaving the molecule in an excited state. However if there is no state with corresponding energy to excite then the photon can either be transmitted (which leaves it unaffected) or scattered. Only a small proportion of incident photons will be scattered with the intensity of the scattered light, I_S, having the dependency on wavelength, λ shown in the equation below [171].

$$I_S \propto \lambda^{-4} \tag{7.1}$$

Of the scattered photons, the majority will be scattered elastically in what is known as Rayleigh scattering. About 1 in 10^7 [172] of the scattered photons will scatter inelastically, transferring some of their energy to the

molecule, resulting in a down shift in the frequency of the photon. These lower frequency photons form what is called 'Stokes radiation'. It is also possible that the photon may gain energy, which can happen when the photon scatters from a molecule which is already in an excited state. The increase in photon energy results in an increase in frequency and is called 'anti-Stokes radiation'. These inelastic scattering processes are collectively known as 'Raman scattering' and both the linewidth and intensity of these frequency shifts is what produces the Raman spectrum for a sample.

Raman spectroscopy can normally be used to investigate both rotational and vibrational states in samples, but in our studies, as the graphene molecule is confined to the surface, rotation is impossible.

Because these shifts can be very small it is important to use monochromatic light for the illumination of samples to ensure that the light from the source is not mistaken for sample data. For this reason laser light is used to illuminate samples, with as much other light as is possible to cut out removed, as to decrease noise levels.

7.3.3 Key features of graphene Raman spectra

There are 3 main peaks to look for in the Raman spectra of mono and few layer graphene. They are the G band at $\sim$ 1580 cm^{-1}, the 2D band at $\sim$ 2700 cm^{-1} and if there are defects present there will also be the D peak at $\sim$ 1350 cm^{-1}. Much information can be gleaned from the ratios of the intensities and the widths of these peaks. It should be noted that the laser energy has been known to affect the relative intensities of the D and G peaks as discussed by Pimenta et al [173].

The G peak is the most simple to understand as it arises directly from the double degeneracy of the E_{2g} vibrational mode at the centre of the Brillouin zone [173]. This vibration can be pictured by deforming the hexagons into a more rectangular shape and then releasing (with the degeneracy aris-

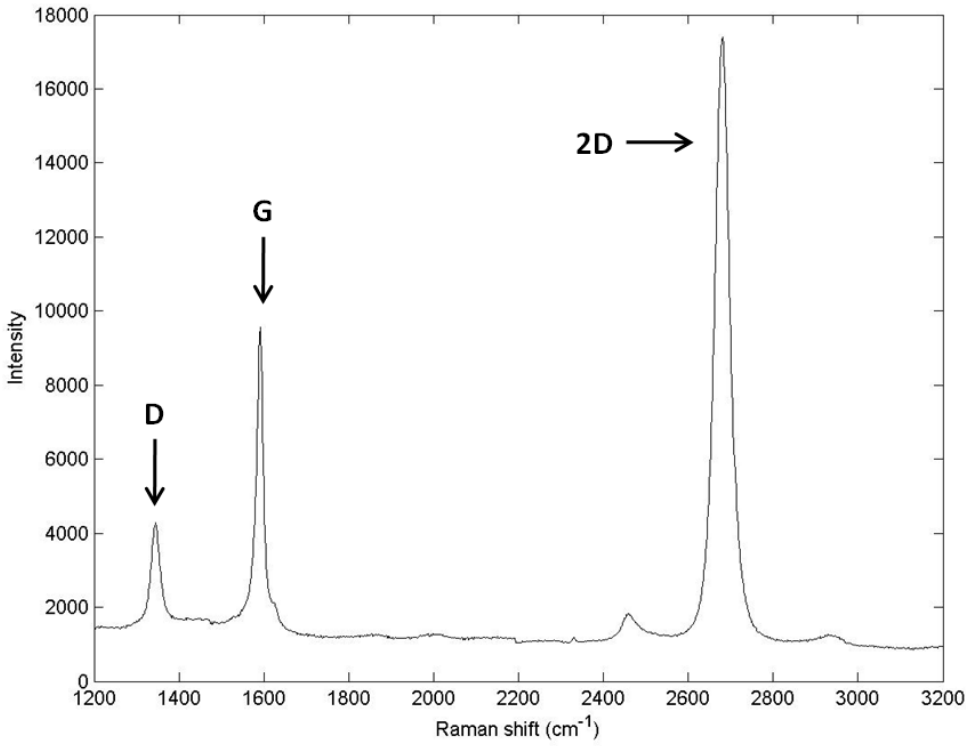

Figure 7.5: A typical Raman spectra from an area of a sample containing graphene. The three main peaks have been labelled.

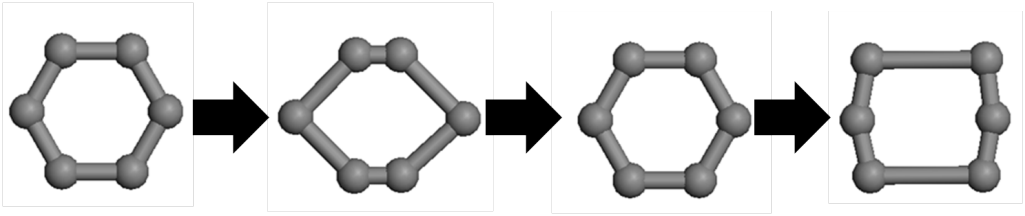

Figure 7.6: This is the doubly degenerate E_{2g} vibrational mode associated with the G peak in the Raman spectra of graphene.

ing from the threefold symmetry of the graphene lattice) and the presence of this peak is a clear indication of sp^2 carbon bonding [173]. As this peak is present in all samples it is often the peak used for normalisation of multiple spectra being compared.

The D band arises from phonon interactions with zone boundaries so is prominent at the edges of the graphene layer and at the sites of defects. As such the intensity of the D peak is often used as a simple way to obtain an estimate of the film quality and for the centre of pristine sheets, should be absent altogether.

More detail on the origins of the D peak were given by Tuinstra and

Koenig [174]. The ratio of the D and G bands (I_D/I_G) can be used to estimate the in plane crystallite sizes as these values are inversely proportional. In addition the width of the D peak can indicate the distribution of domain sizes present, with a broader D peak indicative of a larger range of domain sizes [173].

Historically the 2D band has been referred to as the G' band due to the fact it was the second most prominent peak in all graphite spectra but it has since been learned that this peak is nothing to do with the G peak, but is caused by the second order contribution of the same zone boundary phonons responsible for the D peak [175]. There are also some works where this peak is referred to as D* (as mentioned in Pimenta *et al* [47]). The 2D peak is highly sensitive to the number of layers present. For monolayer graphene the 2D peak is a single Lorentzian peak but as the number of layers increases it evolves into two component peaks, the higher intensity one slightly up shifted from the peak position in the monolayer. The full width half maximum (FWHM) of the 2D peak is also larger for graphite (50 cm^{-1}) than for graphene (25 cm^{-1}) [175] so this can be used as another indicator of the number of layers.

The ratios of the 2D and G peak gives information about the number of layers [158] with monolayer corresponding to a 2D peak roughly four times the height of the G peak [175]. At more than 5 layers thickness the shape of the 2D peak is almost indistinguishable to that of bulk graphite. It should be noted that although Ferarri *et al* state we should expect a 2D/G ratio approaching 4 [175], due to the laser frequency dependency of the G peak mentioned earlier and by Pimenta et al [173], we will be comparing to a commercially bought graphene film.

Figure 7.7 shows a Raman spectrum from a sample of graphene from the same stock used in the experiments in 5.3.2. The film was transferred to silicon oxide by the method discussed in section 7.2 before these spectra were obtained.

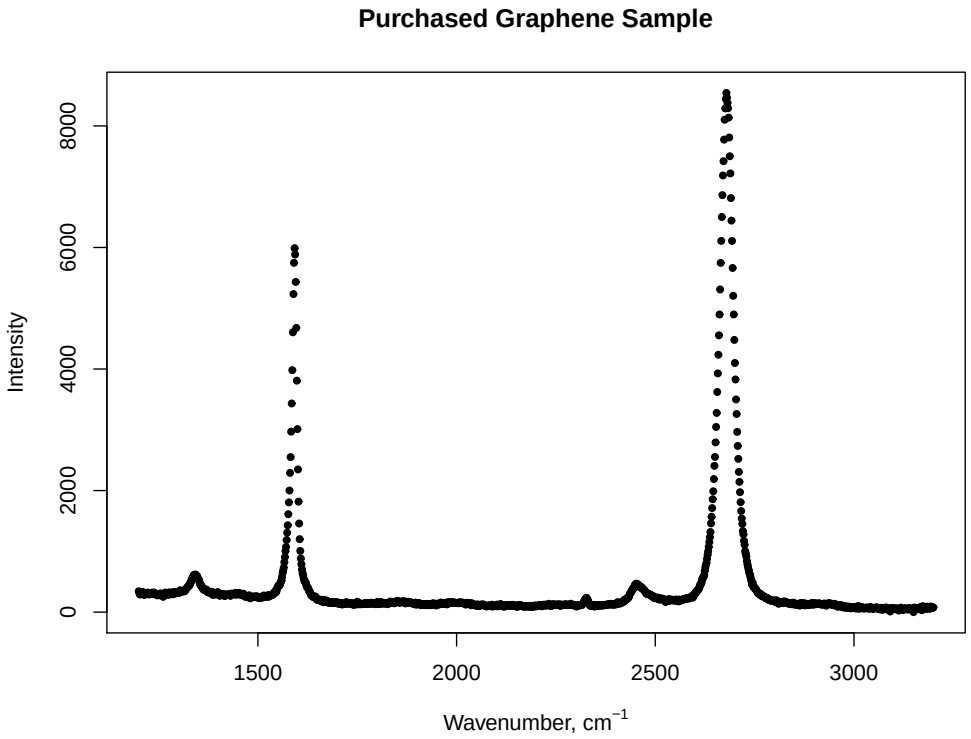

Figure 7.7: Raman spectrum of Graphene purchased from Graphene Laboratories Inc. after transfer to silicon oxide by the method described in section 7.2. Note the D peak is small and the 2D peak is much more intense than the G peak, although not 4 times as intense as predicted by [175].

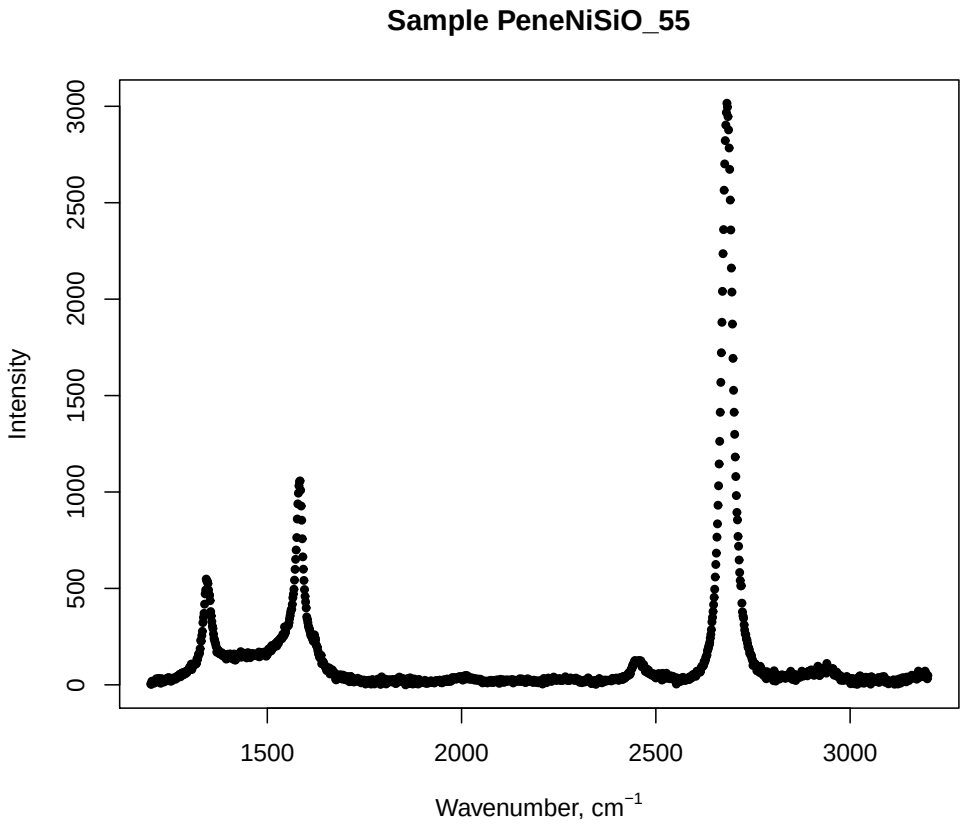

Figure 7.8: Raman spectrum of a sample grown using the propylene method described in section 7.1.1. This sample had the highest 2D/G peak ratio and the smallest FWHM of the 2D peak (32.85 cm^{-1}) from the set of samples grown with the propylene method. The layer is more defective than the bought sample with a higher D peak than would be ideal.

Spectral comparisons to other allotropes of carbon

Graphite has already been covered in the previous section, which leaves this section to help distinguish between other forms of carbon such as diamond, fullerenes, and nanotubes. One of the other peaks to consider is the peak for sp^3 bonded carbon at ~ 1333 cm^{-1} as seen in thin diamond films. Due to the proximity of this peak to the graphene D peak it is easy to mistake this for a large defect peak however if there is a thin diamond film rather than a defect heavy graphene one, the G peak will be very small (due to the lack of sp^2 bonding). The diamond peak is also narrower than typical for the D peak (14-18 cm^{-1} FWHM for diamond [176]).

For carbon nanotubes there is a slight (~ 6 cm^{-1}) down shift present in the G band due to the curvature present in the tubes [177]. There is also often a significant D peak present, especially near the end of a nanotube. The 2D peak in carbon nanotubes also has a slight down shift (< 20 cm^{-1}) compared to graphene.

Fullerenes have quite a different spectra due to the presence of pentagons of carbon in their structure. Although there is a low peak in roughly the position you would see the G peak in graphene, the strongest signal in C_{60} is at 1470 cm^{-1} which is due to the expansion and contraction of the hexagons and pentagons out of phase. There is also a peak corresponding to this expansion in phase at ~ 496 cm^{-1} [178] which is not present in graphene spectra.

All of the peaks mentioned here which fall within our spectral window will be looked for during analysis.

7.3.4 Raman spectroscopy method

A Horiba LabRAM HR Evolution system was used to obtain Raman spectra using the 532 nm wavelength green laser. The 532 nm laser was selected

due to the good contrast between graphene and the underlying substrate in green light.

A 100 μm aperture and a diffraction grating of 600 lines/mm are used within the Raman system for gathering the spectra. The system is calibrated initially using a blank SiO_2 sample using the 520.7 cm^{-1} line of silicon.

Spectra are taken at set positions over areas which had significant contrast visible during the optical microscopy examination, with the laser spot aligned using the co-axial optical microscope built into the Raman system. The spectra are taken over the range 1200 cm^{-1} to 3200 cm^{-1} with an exposure time of 10 seconds and the spectra averaged over four cycles. Reducing the window over which the spectra are taken over reduces the time required for each sample. Averaging over four cycles removes anomalous signal spikes. No additional filter is needed as the detector is not saturated at any point during obtaining spectra from these samples. Spectra were taken over each area of different contrast within a sample.

7.3.5 Raman spectra analysis

All the Raman data is stored in a tab delimited format and subsequently loaded into R [179] for numerical analysis. Each spectrum is treated with a simple linear background removal and peaks are identified as shown in appendix 1. When comparing spectra from different samples we will examine three things. Firstly, the I_G/I_D ratio whose value proportional to crystallite size, which we shall call the crystallite size factor, C_F. Secondly, we examine the I_{2D}/I_G ratio which takes a value approaching 4 for monolayer graphene [175] which we will call the layer factor, L_F, and the full-width half maximum (FWHM) of the 2D peak which we will refer to as FWHM-2D. Note that different areas on a single sample can give slightly different spectra, even with the same settings. Due to this we will be comparing the best spectrum from each sample.

We compare our samples to the spectrum obtained from a commercially available supply of graphene on SiO_2 which became available after these experiments were conducted. The peak values of C_F and L_F for the calibration sample were 6.80 and 1.45 respectively.

7.4 Results and discussions

7.4.1 Comparison of different growth methods

Crystallite size

As discussed in the introduction to this chapter, it was believed that the graphene growth was nucleating from the crystals with the Ni(111) face in the surface plane. As defects are expected where growth from different nucleation sites meet, a larger crystallite size was expected to produce a lower defect density by reducing the density of these nucleation sites, however large grain size would also lead to a rougher surface which would put strain into any graphene films produced. It was predicted there would be an optimal grain size in which these two factors would balance out. AFM was taken of each sample post-anneal to maintain a record of crystallite size and surface roughness.

Variations into the cooling rate were performed on samples grown using propylene as the carbon feedstock with cooling from 650 °C to room temperature in 90 s, 120 s and 180 s. As can be seen in Figure 7.10 this variation in cooling rates did not produce a distinct visual variation in the nickel crystallite size as shown by AFM. Transfer of these films was attempted, however problems with the PMMA layer adhering to uncoated areas of the SiO_2 and damage to the tweezer tips led to this set of transfers failing. Rather than repeating the growth and transfer of these samples it was decided to move onto something else, due to the lack of clear difference in the AFM data.

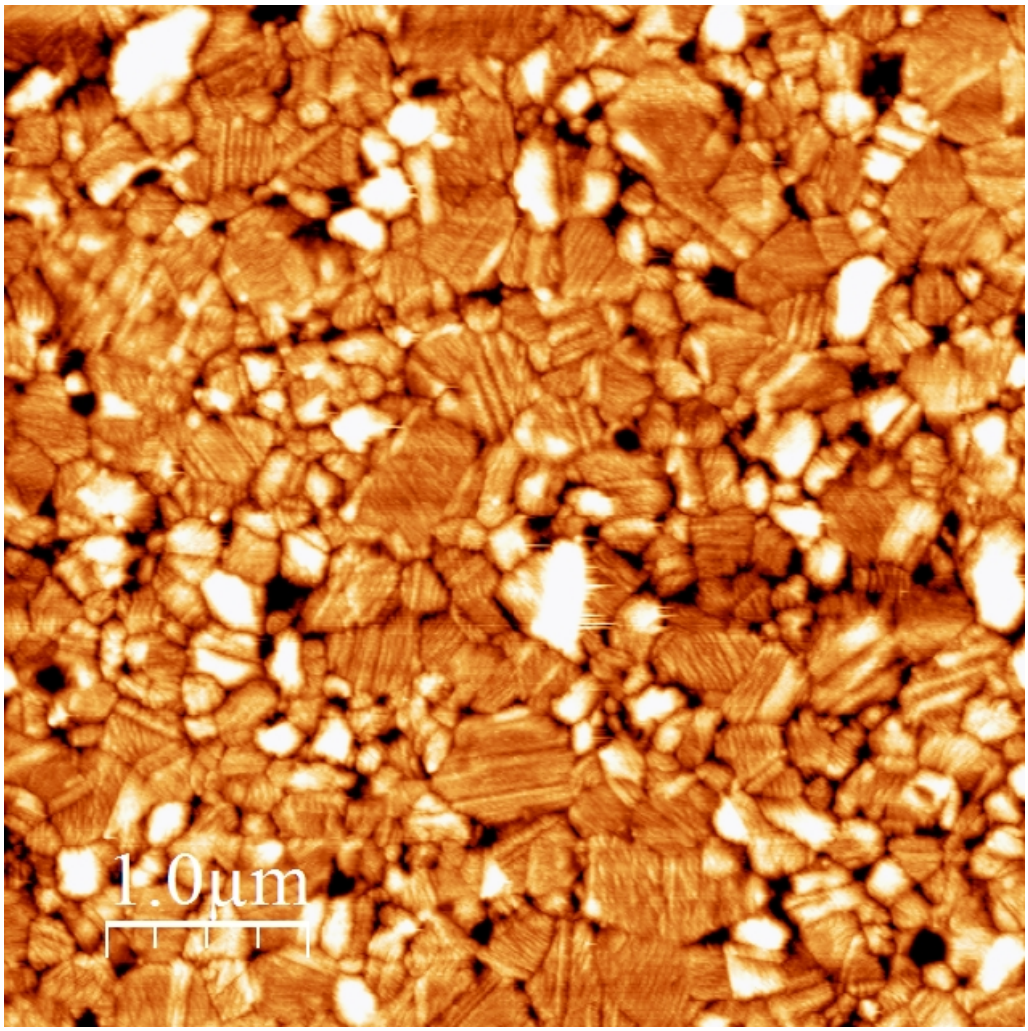

Figure 7.9: AFM image of a polycrystalline nickel layer on an SiO_2 substrate, deposited by our commercial evaporator and then vacuum annealed at 700 °C for 15 mins. Higher features are in light and lower features are dark, with 10 nm difference between the two extremes. This is a typical post anneal substructure of all our samples produced in this way. Thicknesses of this nickel layer varied from 70-110 nm with very little variation in the surface appearance.

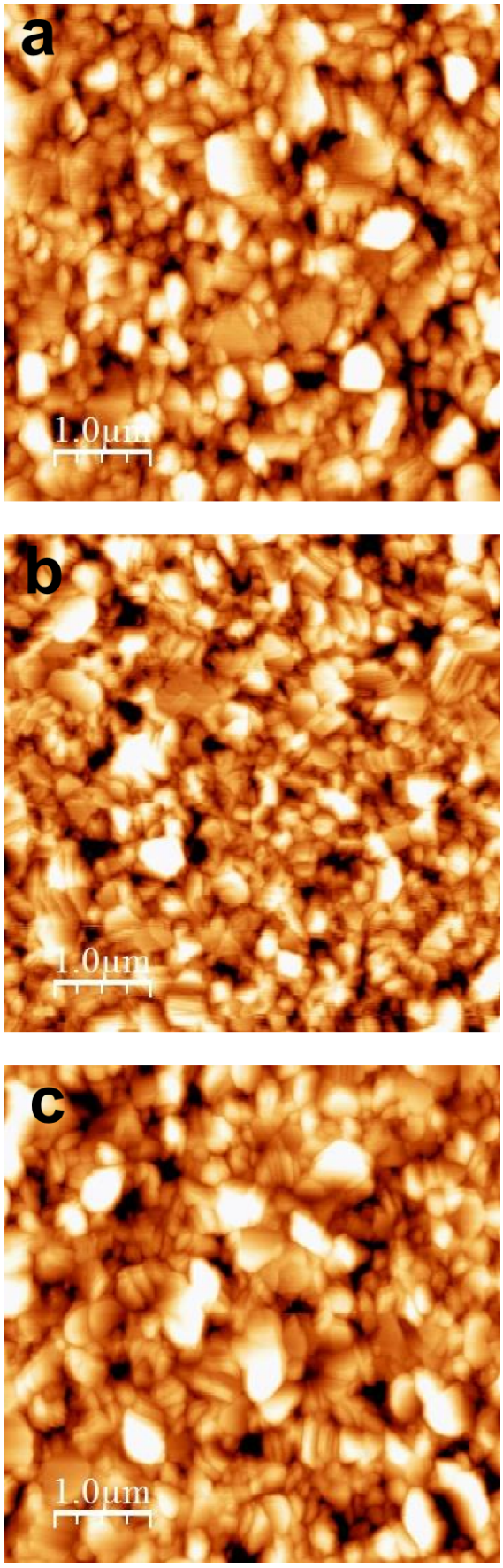

Figure 7.10: AFM images of nickel on $SiO_2$from the cooling rate variation experiments with cooling performed in a) 90 s, b) 120 s and c) 180 s. Cooling performed by rate of reduction of heating and not by other means (such as electrical cooling.) Note how there is no remarkable difference in the grain size of the nickel across these three samples.

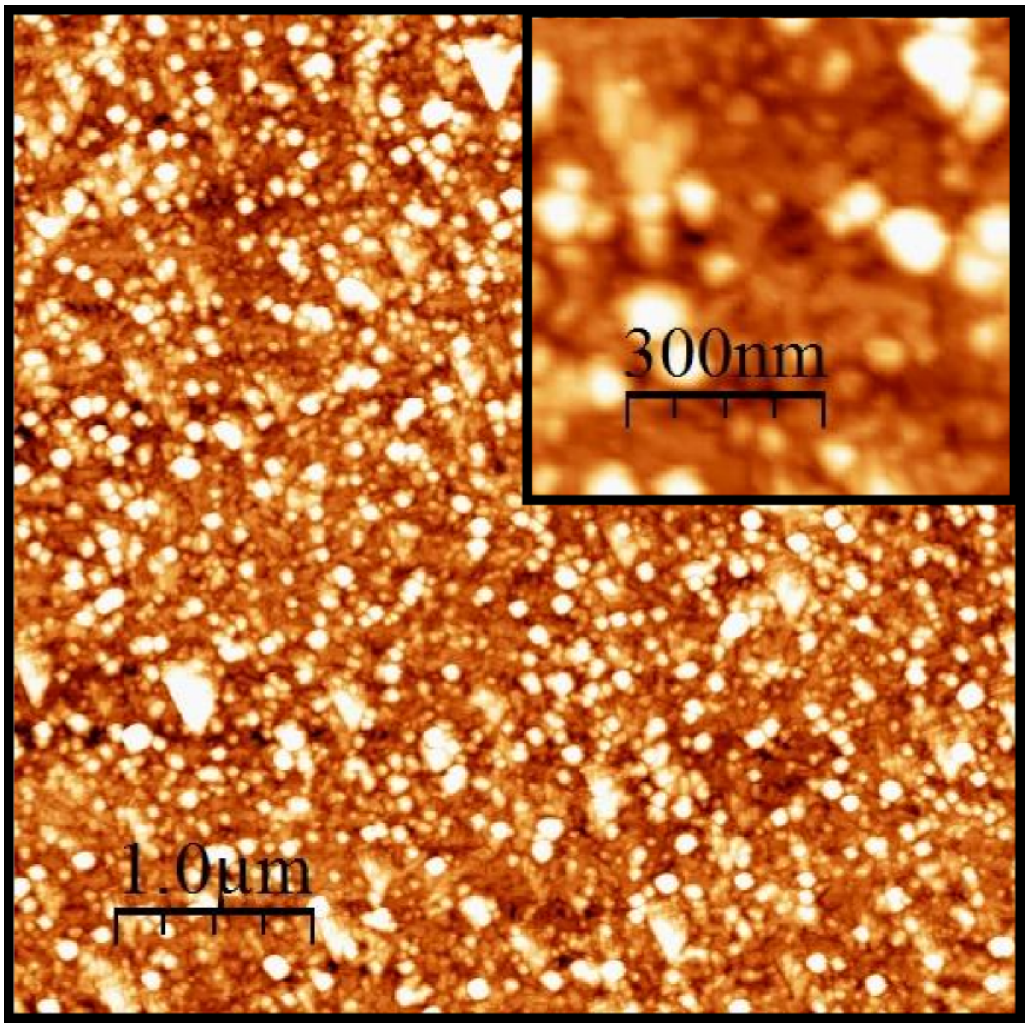

Figure 7.11: AFM image of a sample of Nickel deposited on HOPG and annealed at 710 °C. The inset is a zoomed in image of the same area. This shows a significantly smaller grain size than seen on SiO_2 or sapphire.

When we look at the nickel crystallite size from other methods and compare them we see few differences between the silicon oxide based methods, regardless of source of carbon. Figure 7.1 of nickel on sapphire, shows a similar crystallite size after annealing to those produced on silicon oxide. AFM of HOPG grown samples shows a much finer micro-crystal structure on the surface than the other samples. Substrate seems to also have a greater effect on crystallite size than anneal temperature which does not lead to any noticeable variation within the temperature range investigated.

Growth Methods: Optical and Raman Analysis

Examining numerous samples from each series allows comments to be made on each method. Considering the Raman spectra for the samples leads to the question of which factor should be given most significance, the crystallite factor, the layer factor or the FWHM of the 2D peak? A high crystal factor means a larger area of good quality graphene, a larger layer factor sample will have a fewer number of layers, or may even be a single complete monolayer with a partial second covering layer. The FWHM of the 2D peak gives us an idea on the quality of the film as a narrower 2D peak means fewer different environments of the carbon atoms, increasing the likelihood that the product we have is uniform and does not contain regions of amorphous carbon.

The values of C_F and L_F for the industrially supplied sample were 6.80 and 1.45 respectively with a FHWM for the 2D peak of 41.5176 cm^{-1}. Looking at the samples where graphene was grown from native carbon, the best spectra came from the film on sample NiSiO54 which had values of $C_F = 1.09$, $L_F = 1.81$ and the 2D-FWHM of 38.6941 cm^{-1}. An optical image is included as Figure 7.12. The problem with native carbon is the unpredictability and lack of control available over film growth. This leads to great variations in the films over different samples.

The samples grown from C_{60} show some variation, with no one region being especially superior. The spectrum with the narrowest 2D peak had a poor crystallite factor compared to spectra from other regions on the same sample, indicating smaller graphene grain size. The two areas are shown in question are shown in Figure 7.13. Looking at the values, we see for the area in Figure 7.13a) are: C_F 0.67, L_F 2.28, FWHM 42.8572 cm^{-1}, and for the area in Figure 7.13b):C_F 0.86 , L_F 1.67 , FWHM 44.2856 cm^{-1}. Although they have marginally broader 2D peaks and smaller crystallites the values are comparable to the best of the native carbon films.

We see improvement in the samples grown using propylene. Sample

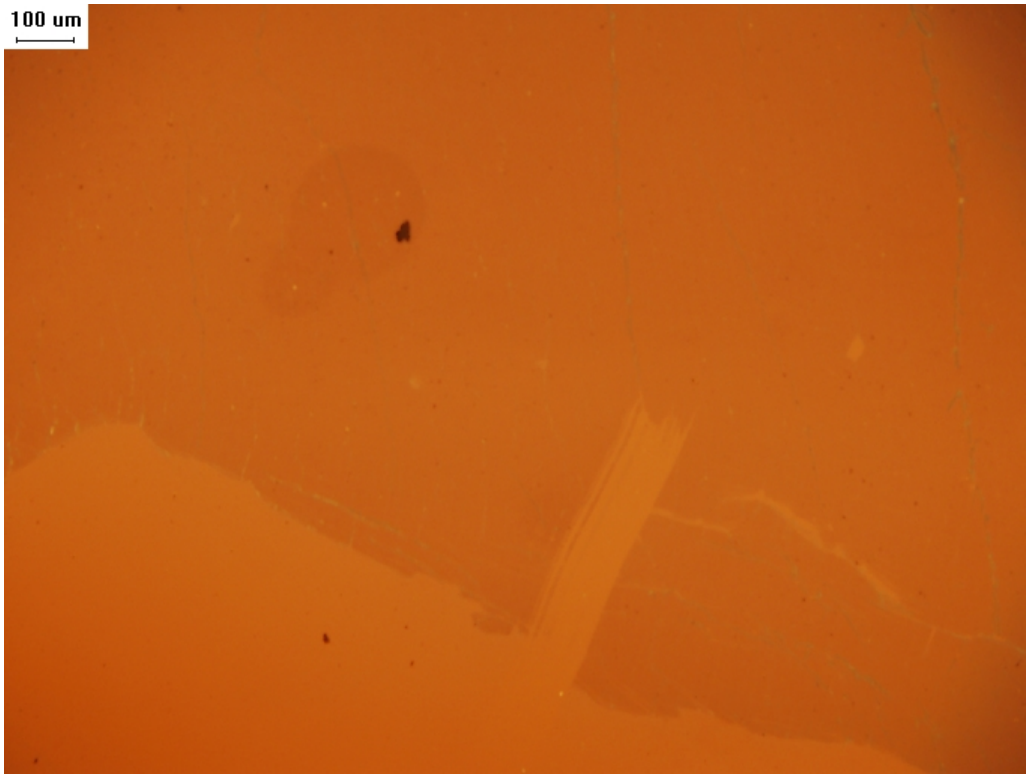

Figure 7.12: Optical image of NiSiO54 graphene film taken using a 10x objective on an Olympus BX51 optical microscope with an exposure time of 60ms. The darker area is graphene, the lighter is bare silicon oxide substrate. There is a small region of bilayer to the top left of the centre next to a dark speck of contamination. This sample was grown in a commercial evaporator from native carbon.

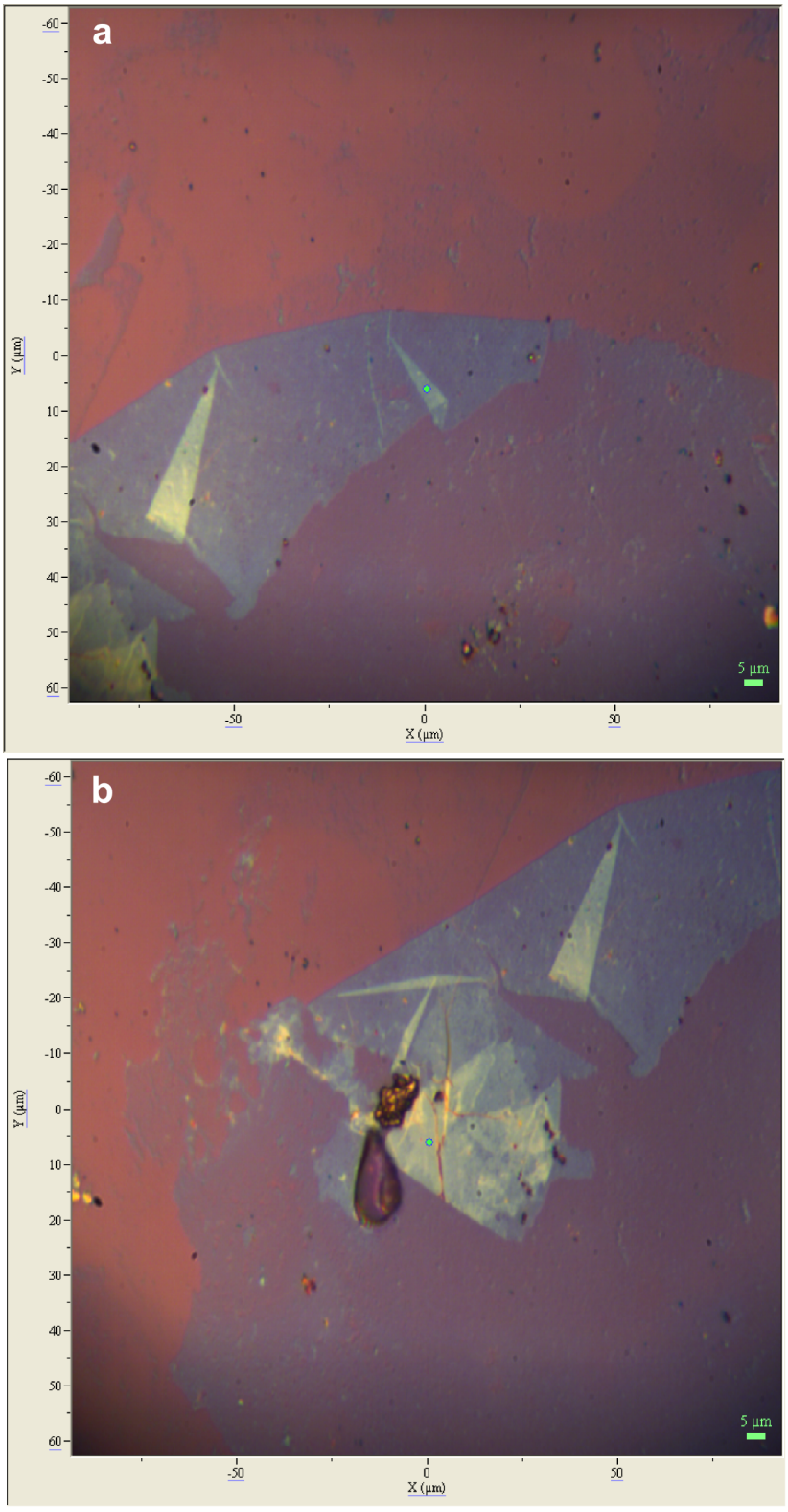

Figure 7.13: Optical images of the areas from which the best two Raman spectra for c60 grown samples were obtained. Both images are different regions on the same sample. Values for the area in Figure a) are: C_F 0.67, L_F 2.28, FWHM 42.8572 cm^{-1}, and for the area in b):C_F 0.86 , L_F 1.67 , FWHM 44.2856 cm^{-1}.

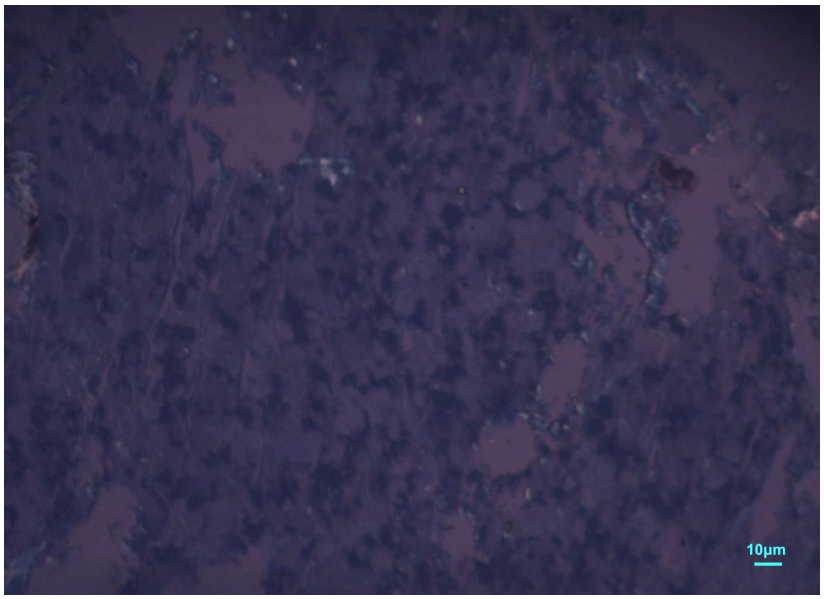

Figure 7.14: Optical image of Sample PeneNiSiO55 with C_F 1.93, L_F 2.85, and 2D-FWHM 32.8569 cm^{-1}. This is the area from which the best Raman spectrum from this series was taken. Vertical cracks (resulting in a lower C_F 1.93) and regions of bilayer can be seen.

Pene-NiSiO-55 gave values surpassing the commercial sample in all but the crystal factor. Values for sample *Pene-NiSiO-55* are C_F 1.93, L_F 2.85, and 2D-FWHM 32.8569 cm^{-1}. An optical image of this sample is included in Figure 7.14. Vertical cracks are visible throughout and the darker areas on top are indicative of thicker layers beginning to form. The area itself does not cover the whole sample. Lack of uniformity in the sample is not ideal for applications.

The samples grown on a HOPG substrate show a structure more similar to the C_{60} or native carbon samples rather than the propylene samples, small patchy areas of high quality film of order tens of microns, with larger areas with the film appearing to have folded back on itself to form multilayer. Figure 7.15a shows the best spectrum with 7.15b showing the area from which it is from. The values of C_F 2.50 L_F 3.09, and 2D-FWHM 39.7878 cm^{-1} are the best for any HOPG substrate based sample we produced, surpassing values on the commercial sample for all but the C_F. The crystal factor is, across all samples, lower on the HOPG grown samples than the propylene grown samples and is still less than half the value of the commercial sample. There is also some visible dirt on the samples when

examined under the microscope suggesting the sample transfer method is not a clean enough process.

These experiments highlight the need for complementary analysis techniques. Although a sample may show good graphene when examined under STM and have a good Raman spectrum, the coverage over the area may be poor, with little material transferred. The optical microscopy examination can give you an indication of how much material has been transferred to a sample but cannot distinguish between high quality graphene and thin films of amorphous carbon. It is only using both these techniques together that the bigger picture can be brought together. Also taking a single point Raman spectrum is not ideal, even if the optical study is used to direct it at an area of high optical contrast, as there is significant variation across the samples surfaces.

7.4.2 Modifications to the transfer method

HCl Etch variations

The etching process represents the stage of production most likely to cause contamination of samples. $FeCl_3$ is a standard industrial etchant for the electronics industry [165]. The sacrificial nickel layer is involved in a redox reaction, where the nickel is oxidised, and the iron is reduced from the ionised form to iron metal. As we are operating under atmospheric conditions any finely powdered iron metal that forms is likely to quickly be oxidised to iron oxide which results in the observed brown flecks observed in post transfer optical microscopy studies. These iron oxide particles will be present on the side of the graphene which was in contact with the nickel and therefore end up between the graphene layer and the substrate after transfer, which will have an adverse effect on the electrical properties. The rinse with deionised water after etching can remove some of them but it does not get all of them. Other groups [67, 180, 181] have used iron nitrate

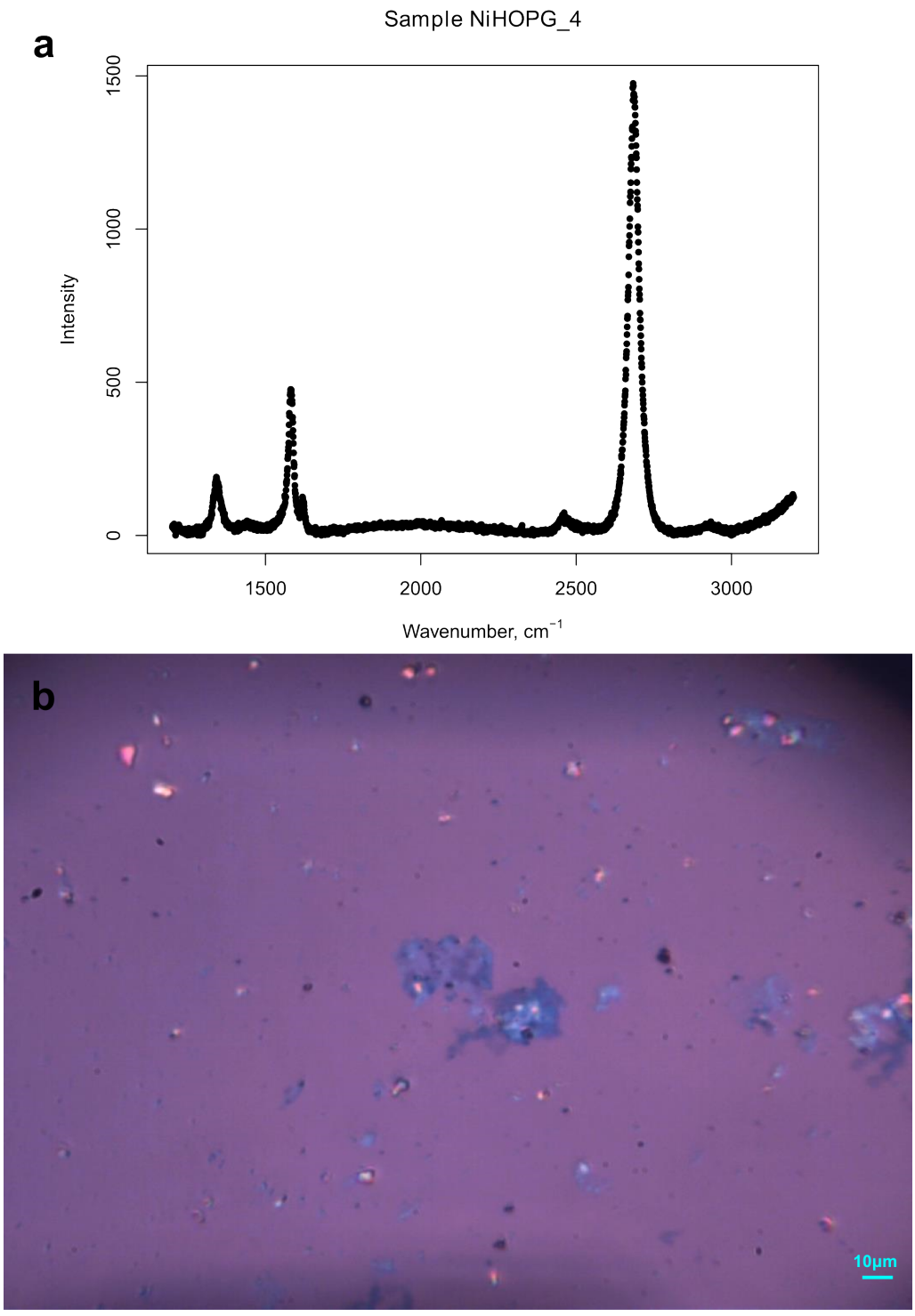

Figure 7.15: a) shows the Raman spectrum for sample NiHOPG_ 4, the best spectra to our criteria. The values of C_F2.50, L_F3.09, and 2D-FWHM 39.7878 cm^{-1} are the best for any HOPG substrate based sample we produced. b) shows the area in which it was taken. Note the small grain size of this area at the centre. The sample also appears to be quite dirty from the transfer process.

for the etching process, yet as this also uses iron, it has the same problem. In order to remove the source of these particles we need to use an alternate etchant which does not contain iron.

The simplest choice of alternate etchant was hydrochloric acid [166]. HCl is known to dissolve metals, it still contains chloride ions (in case they are involved in the mechanism), it is cheap and readily available and it does not contain transition metal atoms.

Initially a solution of HCl at 1 mol dm^{-3} (the same concentration as the iron chloride) was used however after 24 hours of etching the process was still far from complete (although some progress had been made). As this extra time is unacceptably long we increased the concentration of the acid. 2 molar HCl was used on two samples and 21 hours later one of them had etched completely but the other had not. This was progress in the right direction but it was still too slow. At this point, where we had attempted using HCl as an etchant on four different samples, a decision was made that HCl was too slow. As fuming HCl (37%) is approximately 12 molar solution we could have gone to higher concentrations to increase the etch rate but as the higher concentration etch rate was expected to be comparable to $FeCl_3$, yet be more dangerous, it was decided not to do this.

As the speed of a HCl etch was deemed too slow, we took a different approach of adding an additional rinsing stage to the transfer process. After removing the sample from the $FeCl_3$ etchant we rinsed with the 2 molar HCl solution before rinsing with deionized water, with the hope it would remove the iron oxide. As these particulates were much smaller than the bulk nickel had been, a long exposure should not be necessary.

In hindsight we should have looked at a hydrochloric acid and hydrogen peroxide mixture, rather than pure HCl in order to get a competitive etch rate. Published work by Reina *et al* [182] showed success at etching with HCl at 3% but give no indication in their work about the timescale of this process.

Hot plate vs. oven bake

Some investigation was taken into the variations caused by using an oven bake method for the PMMA curing treatment rather than the hot plate curing method with the hope it could reduce the cracking observed in the graphene films. It was suggested that as the hot plate curing method heated from the bottom that the bottom of the PMMA layer would cure faster than the top and this may result in cracking of the PMMA layer and causing the cracking of graphene film during transfer. The idea behind the change to an oven bake was that in an oven bake the PMMA would cure from the top down, leaving the PMMA at the contact surface more flexible and less likely to crack as it dried on that surface. It is also possible cracking of the PMMA layer occured during curing of the PDMS layer above it.

Unfortunately no noticeable change was observed in the few samples in which the oven bake was attempted, but it was not attempted many times. More samples were needed to be able to obtain a clear decision on whether oven bake or hot plate was the best method.

7.5 Improvements and future work

7.5.1 Transfer improvements

The transfer process is long and intricate with many stages with a high possibility of errors occurring. For most stages the sample is held using tweezers. We need to avoid contact with the flat faces of the wafer to avoid scratching the graphene, however doing so makes handling the sample extremely difficult, especially during blow drying. An SiO_2 piece larger than the transferred material can allow some extra area where scratches are not important, in order to increase ease of handling. The PMMA spinning has to be done in the clean room as PMMA is primarily used as a lithography resist and exposure to UV light increases solubility (this is irrelevant for

our processes but we do not want to damage the stock). Transportation from clean room facilities into normal labs gives opportunity for damage. Ideally the whole process should eventually be moved into a clean room environment.

7.5.2 Raman improvements

After the completion of this work it is clear that several changes are needed to improve the whole process. Moving to full Raman mapping rather than taking spectra at specific points. This process relies on the auto focus script on the Raman system to maintain a good focus throughout the process. There had been several problems with the auto focusing tool at the time these data were being collected and it was deemed too unreliable to be used. Several problems with the illumination on the inbuilt optical microscope made it difficult to find the exact same features as had been observed on the standalone optical systems. In addition taking full Raman maps of each sample takes much longer than a few single points across the sample, and the single point spectra should provide us with a good basic indication of the quality, when combined with the optical data. Once a good quality uniform film has been identified it would be worth it to go back and perform a full Raman map.

7.6 Graphene synthesis summary

The C_{60} grown films and some of the better of the native carbon grown films, appear more uniform than the propylene grown samples but Raman spectra show they are of lower quality. Although the propylene samples are better under Raman at specific points, the optical images show a lack of uniformity in the films, which is far from ideal for potential applications.

The main difficulties with the work in this chapter come from the fact

that it is impossible to characterise the quality of the graphene in a suitable way before it has been transferred. STM can be used to image the graphene while it is on the nickel but the technique can only scan small areas at a time (a one micron square would be considered a large area for an STM image). As we cannot assess the quality before transfer we cannot know if a poor coverage is due to problems with the growth process, problems with the transfer process or a combination of the two.

Ultimately the nickel catalysis method is not the best for large scale graphene production. As the nickel has to be etched from the side of the stack, rather from the back of the stack (as is the case in copper catalysed methods [67, 180]), the etch distance is greater and therefore the etch time is much longer. This time is also proportional to the area of graphene produced. Our samples were of the scale of several millimetres to 1 centimetre, which is a size that is appropriate to the size of chip devices produced by the micro-electronics industry, however this does not give us the flexibility to produce larger films that might be required for flexible display technologies.

Ultimately, due to the rapid pace of development within the graphene community, both the growth and transfer methods discussed here are now obsolete due to newer copper CVD growth [67, 180], germanium based growth [183] and so called 'dry transfer' methods [184].

Chapter 8

Summary

This thesis has examined several different molecular networks adsorbed on various different substrates. Molecular networks are expected to be useful for molecular level filtering and templating, catalysis, and sensor applications .

In the work in Chapter 5, we performed investigations into the hydrogen bonded structures formed by closely related tetracarboxylic acid molecules. A change of substrate to graphene on copper resulted in the same type of random tiling as seen by Stannard *et al* on HOPG [126], with an underlying hexagonal symmetry, yet a lack of translational symmetry. We have highlighted the importance of solvent selection, and how a change of solvent can completely change the structure formed. By addition of a different solvent, to a dried TPTC monolayer we observed recrystallisation into a form that would have matched the one observed if that solvent had been used for the initial deposition. The characteristics of the random tiling networks observed for both the change of substrate, and the water deposition with recrystallisation, are comparable. Both incidences of the hydrogen bonded random tiling network show fractions of the five different molecular junction types in good agreement with each other. The Ψ values (order parameter) for TPTC deposited from nonanoic acid were in agreement for both the value obtained on graphene on copper, and for the nonanoic in-

duced recrystallisation samples. These Ψ values differed from those in the literature, with the discrepancy attributed to the smaller crystallite size due to differences in nucleation process compared to the situation on plain HOPG.

In Chapter 6 progress is made towards covalently linked porous molecular networks. We observed two distinct phases for the arrangement of the molecule TBPB on gold, down from the original 3, after revealing that what had previously been reported as phase 1, was actually a drift distorted image of phase 2. Investigations into lower concentrations of molecules suggested an island based growth mechanism for this molecule in ambient conditions, as opposed to the formation of the more open porous network observed in UHV [137]. Dimerisation of TBPB into TBPQ was achieved by deposition onto substrates heated at $200°C$ or higher, with a few higher polymerised molecules present at defects or phase boundaries. Termination of the polymerisation process after dimerisation is attributed to orientation restrictions within the initial adsorption phase structures. Variations on the TBPB experiment using larger framework molecules failed due to poor solubility of the larger molecules in ethanol. Changing solvent would require a transition from dried networks to full liquid STM studies and ideally would involve repeating the TBPB work in the new solvent. Repeating the experiments on copper failed to yield resolvable images.

DBrBA, another molecule utilising the bromine based linkage reaction, showed a promising result in an initial experiment, but attempts to repeat the result failed. DBrBA molecules tended to agglomerate into micron scale dendritic structures due to a lack of compatibility of the solvent.

In Chapter 7 we described the development of methods for graphene synthesis using nickel based catalysis. Our results highlighted the need for complementary analysis techniques, as films that looked better under optical microscopy did not match with those that had better spectra. The C_{60} grown films were more uniform but of lower quality than the propylene grown films. Propylene films had areas of higher quality but they were

smaller with less graphene per unit area across a sample. The lack of scalability in the sacrificial nickel process has led to it being surpassed by other techniques (such as the copper CVD method or germainium method [183]).

Appendices

Appendix A

Raman Analysis script

This is the R code used to analyse and plot the Raman spectra for the graphene samples:

```
# First, read in the data file.
# As this is a tab separated data file we need "read.table".
# to read in the data as an array.
raman1=read.table(file.choose())
# file.choose opens up a windows explorer box for us to select the
#file to read
names(raman1)[1]="wavenumber"
names(raman1)[2]="intensity"
# names the two columns in the dataset where [x] is the column number
# subtracting background linearly.
# The $ allows us to select named columns of the data set
raman1$intensity=raman1$intensity-min(raman1$intensity)
# plot wavenumber against intensity.  "xlab" and "ylab" set axis titles.
# "main=title" sets graph title
plot(raman1$wavenumber,raman1$intensity,main="title",
xlab=expression(paste("Wavenumber, cm"^"-1")), ylab="Intensity",pch=20)
# The G peak lies between 1500 and 1700
# first we set these boundaries
v=min(abs(raman1$wavenumber-1500)) ;
lower_g= which.min(abs(raman1$wavenumber-1500))
upper_g= which.min(abs(raman1$wavenumber-1700))
# Then we find the maximum within this range
# square brackets are used for a range within an array
intensity_g = max(raman1$intensity[lower_g:upper_g])
# repeat for other peaks
intensity_d = max(raman1[1:lower_g,2])
lower_2d= which.min(abs(raman1$wavenumber-2500))
upper_2d= which.min(abs(raman1$wavenumber-2800))
# Find intensity and position of the 2D peak
intensity_2d = max(raman1$intensity[lower_2d:upper_2d])
peakpos = which.max(raman1$intensity[lower_2d:upper_2d])
# note that this provides position of peakpos within specified range
# not within whole range
```

```
# modify peakpos to take account of full range.
peakpos = peakpos+lower_2d
# find the positions of the value at half maximum
lower_midpoint=which.min(abs(raman1$intensity
[lower_2d:peakpos]-(intensity_2d/2)))
upper_midpoint=which.min(abs(raman1$intensity
[peakpos:upper_2d]-(intensity_2d/2)))
# modify to account for full range
lower_midpoint=lower_midpoint+lower_2d
upper_midpoint=upper_midpoint+peakpos
# Find the wavenumber of the full-width half maximum
FWHM=(raman1$wavenumber[upper_midpoint]-raman1$wavenumber[lower_midpoint])
# finding the Ig/Id ratio, proportional to crystallite size
crystallite_factor=intensity_g/intensity_d
# sprintf displays a text string to the screen
# % g is a placeholder for the variable
sprintf("The crystallite factor is % g",crystallite_factor)
# finding the thickness factor
layer_factor=intensity_2d/intensity_g
sprintf("The layer factor is % g",layer_factor)
sprintf("The FWHM of the 2D peak is % g cm-1",FWHM)
```

This R code is used to automatically calculate the layer factor, crystallite factor and 2D-FWHM for all raman data files in the selected folder and write the results to a single file. This is used for samples where spectra were taken at many different points across a sample surface. The selected folder is the R active directory.

```
    # initialise variables x=1
tmp=1
txtfiles=1
FWHM=1
crystallite_ factor=1
layer_ factor=1
Gr_ data=1


    # read folder
txtfiles = list.files(pattern="*.txt")


    for(x in 1:length(txtfiles)){
# read in the files with whitespace seperating columns
tmp = read.table(txtfiles[x], sep="")


    # name the two columns in the dataset where [x] is the column
number
names(tmp)[1]="wavenumber"
names(tmp)[2]="intensity"


    # linearly remove background
tmp$intensity=tmp$intensity-min(tmp$intensity)


    # The G peak lies between 1500 and 1700
# first we set these boundaries
v=min(abs(tmp$wavenumber-1500)) ;
lower_ g= which.min(abs(tmp$wavenumber-1500))
upper_ g= which.min(abs(tmp$wavenumber-1700))
# Then we find the maximum within this range
# square brackets are used for a range within an array
intensity_ g = max(tmp$intensity[lower_ g:upper_ g])


    # repeat for other peaks
intensity_ d = max(tmp[1:lower_ g,2])
lower_ 2d= which.min(abs(tmp$wavenumber-2500))
```

```
upper_ 2d= which.min(abs(tmp$wavenumber-2800))
# Find intensity and position of the 2D peak
intensity_ 2d = max(tmp$intensity[lower_ 2d:upper_ 2d])
peakpos = which.max(tmp$intensity[lower_ 2d:upper_ 2d])
# note that this provides position of peakpos within specified range,
not within whole
range
# modify peakpos to take account of full range.
peakpos = peakpos+lower_ 2d


    # find the positions of the value at half maximum
lower_ midpoint=which.min(abs(tmp$intensity[lower_ 2d:peakpos]-(intensity_
2d/2)))
upper_ midpoint=which.min(abs(tmp$intensity[peakpos:upper_ 2d]-(intensity_
2d/2)))


    # modify to account for full range
lower_ midpoint=lower_ midpoint+lower_ 2d
upper_ midpoint=upper_ midpoint+peakpos


    # Find the wavenumber of the full-width half maximum
FWHM[x]=(tmp$wavenumber[upper_ midpoint]-tmp$wavenumber[lower_ midpoint])
# finding the Ig/Id ratio, proportional to crystallite size
crystallite_ factor[x]=intensity_ g/intensity_ d


    # finding the thickness factor
layer_ factor[x]=intensity_ 2d/intensity_ g


    } # end of the for loop


    # write the useful data into a new dataframe
Gr_ data=data.frame(1:x,crystallite_ factor,layer_ factor,FWHM)


    # set a temporary string with the first entry of the textfiles
list
namestring=txtfiles[1]


    # take the first part of the filename (the part containing the
sample name)
namebox=gsub( " .*$", "", namestring )
# gsub is a regular expression replacing everything in the first
quotes
```

```
# with those in the second.  "." is any character.
# "*" is any number of times.  $ tells it to stop at the end of
the string.
# this ‘gsub’ deletes everything after the first whitespace


    write.table(Gr_ data, file = paste0(namebox,"_ raman.dat"),
sep = "")
```

REFERENCES

[1] R. Hooke, *Micrographia:or some Physical descriptions of minute bodies made by magnifying glasses with observations and inquiries thereupon.* Royal Society of London, 1665, digitised version available from *http* : *//lhldigital.lindahall.org/cdm/compoundobject/collection/nat_hist/id/*384.

[2] F. L. Pedrotti, L. M. Pedrotti, and L. S. Pedrotti, *Introduction to Optics*, 3rd ed. Pearson Education Inc., 2007, ch. 11-4, pp. 279–281.

[3] Nobelprize.org, "Press release: The 1986 nobel prize in physics." *http* : *//www.nobelprize.org/nobel_prizes/physics/laureates/*1986/*press.html*, 26 Mar 2013.

[4] V. Hallmark, S. Chiang, J. F. Rabolt, J. D. Swalen, and R. J. Wilson, "Observation of atomic corrugation on Au(111) by Scanning Tunnelling Microscopy," *Physical Review Letters*, vol. 59, no. 25, pp. 2879–2882, 1987.

[5] A. D. Stefanis and A. A. G. Tomlinson, *Scanning Probe Microscopies: From Surface Structure to Nano-Scale Engineering.* Trans Tech Publications, 2001.

[6] B. Bhushan, *Principles and Applications to Tribology*, 2nd ed. John Wiley & Sons, 2013, ch. 3.4.3, p. 155.

[7] C. by A. D. McNaught and A. Wilkinson., *IUPAC. Compendium of Chemical Terminology,(the "Gold Book")*, 2nd ed. Oxford: Blackwell Scientific Publications, 1997.

[8] P. A. Tipler and G. Mosca, *Physics for Scientists and Engineers*, 5th ed. New York: W. H. Freeman and Co., 2004, ch. 35.

[9] D. A. Bonnell, Ed., *Scanning probe microscopy and spectroscopy : theory, techniques, and applications*, 2nd ed. Wiley, 2001.

[10] J. A. Stroscio and W. J. Kaiser, Eds., *Scanning Tunneling Microscopy*, 1st ed. Academic Press Inc., 1993.

[11] W. M. Haynes, Ed., *CRC Handbook of Chemistry and Physics*, 93rd ed. CRC Press, 2012, ch. 12:Properties of Solids, pp. 12–124: Electron work function of the elements.

[12] J. Tersoff and D. R. Hamann, "Theory of the scanning tunneling microscope," *Physical Review B*, vol. 31, no. 2, p. 805, 1985.

[13] C. Bai, *Scanning Tunneling Microscopy and its application.* Springer, 1992.

[14] J. R. Hook and H. E. Hall, *Solid State Physics*, 2nd ed. John Wiley and Sons, 1991, ch. 3.

[15] J. Bardeen, "Tunnelling from a many-particle point of view," *Physical Review Letters*, vol. 6, pp. 57–59, 1961.

[16] R. M. Feenstra, J. A. Stroscio, J. Tersoff, and A. P. Fein, "Atom-selective imaging of the GaAs(110) surface," *Physical Review Letters*, vol. 58, no. 12, 1987.

[17] N. D. Lang, "Spectroscopy of single atoms in the scanning tunneling microscope," *Physica review B*, vol. 34, pp. 5947–5950, 1986.

[18] A. Selloni, P. Carnevali, E. Tosatti, and C. D. Chen, "Voltage-dependant scanning tunnelling microscopy of a crystal surface: Graphite," *Physical Review B.*, vol. 31, pp. 2602–2605, 1985.

[19] C. J. Chen, "Origin of atomic resolution on metal surfaces in Scanning Tunnelling Microscopy," *Physical Review Letters*, vol. 65, no. 4, pp. 448–451, 1990.

[20] J. Wintterlin, J. Wiechers, H. Brune, T. Gritsch, H. Höfer, and R. J. Behm, "Atomic-resolution imaging of close-packed metal surfaces by Scanning Tunnelling Microscopy," *Physical Review Letters*, vol. 62, no. 1, pp. 59–62, 1989.

[21] T. Nishino, T. Ito, and Y. Umezawa, "Carbon nanotube scanning tunneling microscopy tips for chemically selective imaging," *Analytical Chemistry*, vol. 74, pp. 4275–4278, 2002.

[22] R. Wiesendanger and H. J. Güntherodt, Eds., *Scanning Tunneling Microscopy III*, 2nd ed. Springer, 1996.

[23] R. Wiesendanger and G. H. J, Eds., *Scanning Tunneling Microscopy I*, 2nd ed. Springer, 1994.

[24] J. K. Spong, H. A. Mizes, L. J. LaComb, Jr., M. M. Dovek, J. E. Frommer, and J. S. Foster, "Contrast mechanism for resolving organic molecules with tunnelling microscopy," *Nature*, vol. 338, pp. 137–139, 1989.

[25] H. Ohtani, R. J. Wilson, S. Chiang, and C. M. Mate, "Scanning tunneling microscopy observations of benzene molecules on the Rh(111)-(3 x 3) ($C_6H_6 + 2\,CO$) surface," *Physical Review Letters*, vol. 60, pp. 2398–2401, 1988.

[26] M. P. Samanta, W. Tian, and S. Datta, "Electronic conduction through organic molecules," *Physical Review B*, vol. 53, no. 12, p. R7626, 1996.

[27] D. M. Eigler and K. Schweizer, "Positioning single atoms with a scanning tunnelling microscope," *Nature*, vol. 344, pp. 524–526, 1990.

[28] J. Wintterlin, H. Brune, H. Höfer, and R. J. Behm, "Atomic scale characterization of oxygen adsorbates on Al(111) by scanning tunneling microscopy," *Applied Physics A*, p. 99, 1988.

[29] A. Research, *MFP3D Operation and Installation Manual v*04_08. Asylum Research, 2008, ch. 5.2.

[30] R. G. Carr, "Finite element analysis of pzt tube scanner motion for scanning tunnelling microscopy," *Journal of Microscopy*, vol. 152, no. 2, p. 379, 1988.

[31] B. Bhushan, Ed., *Springer handbook of Nanotechnology.* Springer, 2007.

[32] G. Binnig and D. Smith, "Singletube threedimensional scanner for scanning tunneling microscopy," *Rev. Sci. Instrum*, vol. 57, no. 8, p. 1688, 1986.

[33] T. E. Marlin, *Process Control: Designing processes and control systems for dynamic performance*, 2nd ed. McGraw-Hill, 2000, ch. 8, the PID algorithm.

[34] J. Stirling, "Control theory for scanning probe microscopy revisited," *preprint*, 2014.

[35] A. Chambers, *Modern Vacuum Physics*, ser. Masters series in physics and astronomy. London: Chapman & Hall /CRC press, 2005, ch. 1.4, p. 7, iSBN 0849324386.

[36] W. Steckelmacher, "Knudsen flow 75 years on: the current state of the art for flow of rarefied gases in tubes and systems," *Rep. Prog. Phys*, vol. 49, pp. 1083–1107, 1986.

[37] J. C. Swarbrick, J. B. Taylor, and J. N. O'Shea, "Electrospray deposition in vacuum," *Applied Surface Science*, vol. 252, pp. 5622–5626, 2006.

[38] C. J. Chen, *Introduction to Scanning Tunnelling Microscopy*, 2nd ed. Oxford University Press, 2008.

[39] D. Rajwar, X. Sun, S. J. Cho, A. C. Grimsdale, and D. Fichou, "Synthesis and 2d self-assembly at the liquid-solid interface of end-substituted star-shaped oligophenylenes," *CrystEngComm*, vol. 14, pp. 5182–5187, 2012.

[40] J. A. Stroscio and W. J. Kaiser, Eds., *Scanning Tunneling Microscopy*, 1st ed. Academic Press Inc., 1993.

[41] V. Y. Yurov and A. N. Klimov, "Correction of drift and slope distortions in STM image and scanner calibration," *Surface and Interface Analysis*, vol. 22, pp. 84–88, 1994.

[42] S. de Feyter and F. C. de Schryver, "Self-assembly at the liquid/solid interface: Stm reveals," *J. Phys. Chem. B*, vol. 109, pp. 4290–4302, 2005.

[43] F. K. Inagaki Michio, *Carbon Materials Science and Engineering: From Fundamentals to Applications*. Tsinghua University Press, 2006, ch. 3.2.3, p. 312.

[44] A. Bryant, D. P. E. Smith, and C. F. Quate, "Imaging in real time with the tunneling microscope," *Applied Physics Letters*, vol. 48, pp. 832–834, 1986.

[45] P. Delhaes, Ed., *Carbon Based Solids and Materials*. John Wiley & Sons, 2013, ch. 1.5.3 Presentation of the Crystalline forms.

[46] M. S. del Río, M. Gambaccini, G. Pareschi, A. Taibi, A. Tuffanelli, and A. Freund, "Focusing properties of mosaic crystals," *SPIE proceedings*, vol. 3448, pp. 246–255, 1998.

[47] M. A. Pimenta, G. Dresselhaus, M. S. Dresselhaus, L. G. Cançado, A. Jorio, and R. Saito, "Studying disorder in graphite-based systems by Raman spectroscopy," *Physical Chemistry Chemical Physics*, vol. 9, pp. 1276–1291, 2007.

[48] J. H. Warner, F. Schaffel, M. Rummeli, and A. Bachmatiuk, *Graphene: Fundamentals and emergent applications*. Elsevier, 2012, ch. 2.

[49] J. Paredes, A. Martínez-Alonso, and J. Tascón, "Triangular versus honeycomb structure in atomic-resolution stm images of graphite," *Carbon*, vol. 31, pp. 476–479, 2001.

[50] H. A. Mizes, S. il Park, and W. A. Harrison, "Multiple-tip interpretation of anomalous scanning-tunneling-microscopy images of layered materials," *Physical Review B*, vol. 36, no. 8, pp. 4491–4494, 1987.

[51] A. Yacoby, "Graphene:tri and tri again," *Nature Physics*, vol. 7, pp. 925–926, 2011.

[52] Georg Albert PVD, "Beschichtungen Hauptstraße 24 Germany 76857 Silz," georgalbert@web.de.

[53] J. V. Barth, H. Brune, G. Ertl, and R. J. Behm, "Scanning tunneling microscopy observations on the reconstructed Au(111) surface: Atomic structure, long-range superstructure, rotational domains, and surface defects," *Physical Review B*, vol. 42, no. 15, pp. 9307–9318, 1990.

[54] C. H. Wöll, S. Chiang, R. J. Wilson, and P. H. Lippel, "Determination of atom positionings at stacking-fault disloctions on Au(111) by scanning tunnelling microscopy," *Physical Review B*, vol. 39, no. 11, pp. 7988–7991, 1989.

[55] Wikimedia commons, "Herring-bone reconstruction Au(111) surface," $http://commons.wikimedia.org/wiki/File:Herring-bone.jpg$.

[56] C. Casari, S. Foglio, F. Siviero, A. L. Bassi, M. Passoni, and C. Bottani, "Direct observation of the basic mechanisms of Pd island nucleation on Au(111)," *Physical Review B*, 2009.

[57] C. Wöll, S. Chiang, R. J. Wilson, and P. H. Lippel, "Determination of atom positions at stacking-fault dislocations on Au(111) by scanning tunneling microscopy," *Physical Review B*, 1989.

[58] U. Harten, A. M. Lahee, J. P. Toennies, , and C. Wöll, "Observation of a soliton reconstruction of Au(111) by high-resolution helium-atom diffraction," *Physical Review Letters*, vol. 54, no. 24, pp. 2619–2622, 1985.

[59] J. Perderau, J. P. Biberian, and G. E. Rhead, "," *J. Phys. F*, vol. 4, p. 798, 1978.

[60] H. Melle and E. Menzel, "Superstructures on spherical gold crystals," *Zeitschrift fur Naturforschung*, vol. 33a, pp. 282–289, 1978.

[61] K. Takayanagi and K. Yagi, "Monatom-high level electron microscopy of metal surfaces," *Transactions of the Japan Institute of Metals*, vol. 24, no. 6, pp. 337–348, 1983.

[62] wok.mimas.ac.uk, search on 'Web of Science' database with the filters 2009-2012, excluding patents. Date of search: 8th July 2013.

[63] K. S. Novoselov, A. K. Geim, S. V. Morozov, D. Jiang, Y. Zhang, S. V. Dubonos, I. V. Grigorieva, and A. A. Firsov, "Electric field effect in atomically thin carbon films," *Science*, vol. 306, pp. 666–669, 2004.

[64] T. Ohta, A. Botswick, T. Seyller, K. Horn, and E. Rotenberg, "Controlling the electronic structure of bilayer graphene," *Science*, vol. 313, pp. 951–954, 2006.

[65] P. Lazar, F. Karlický, P. Jurečka, M. Kocman, E. Otyepková, K. Šafářová, and M. Otyepka, "Adsorption of small organic molecules on graphene," *Journal of the American Chemical Society*, vol. 135, pp. 6372–6377, 2013.

[66] B. Partoens and F. M. Peeters, "From graphene to graphite: Electronic structure around the k point," *Physical Review B*, 2006.

[67] X. Li, W. Cai, J. An, S. Kim, J. Nah, D. Yang, R. Piner, A. Velamakanni, I. Jung, E. Tutuc, S. K. Banerjee, L. Colombo, and R. S. Ruoff, "Large-area synthesis of high-quality and uniform graphene films on copper foils," *Science*, vol. 324, no. 5932, pp. 1312–1314, 2009.

[68] N. A. Luechinger, E. K. Athanassiou, and W. J. Stark, "Graphene-stabilized copper nanoparticles as an air-stable substitute for silver

and gold in low-cost ink-jet printable electronics," *nanotechnology*, vol. 19, p. 445201, 2008.

[69] L. Gross, F. Mohn, N. Moll, P. Liljeroth, and G. Meyer, "The chemical structure of a molecule resolved by atomic force microscopy," *Science*, vol. 28, pp. 1110–1114, 2009.

[70] D. Tomalia, "Meet the molecular superstars chemists have created," *New Scientist*, vol. 132, no. 1796, p. 30, November 1991.

[71] L. Milgrom, "Unnatural chemistry in the playroom," *New Scientist*, vol. 120, no. 1641, p. 61, 1988.

[72] E. A. Silinsh and V. Čápek, *Organic Molecular Crystals: Interaction Localization and Transport Phenomena.* American Institute of Physics, New York, 1994.

[73] A. Saywell, J. K. Sprafke, L. J. Esdaile, A. J. Britton, A. Rienzo, H. L. Anderson, J. N. O'Shea, and P. H. Beton, "Conformation and packing of porphyrin polymer chains deposited using electrospray on a gold surface," *Angewandte Chemie International Edition*, vol. 49, no. 48, p. 9136 9139, 2010.

[74] T. Kudernac, S. Lei, A. A. W. Elemans, and S. D. Feyter, "Two-dimensional supracmolecular self-assembly," *Chemical Society Reviews*, vol. 38, pp. 402–421, 2009.

[75] A. Ulman, "Self-assembled monolayers," *Chem Rev*, vol. 96, pp. 1533–1554, 1996.

[76] H. Grönbeck, A. Curioni, , and W. Andreoni, "Thiols and disulfides on the Au(111) surface: The headgroup-gold interaction," *Journal of the American Chemical Society*, vol. 122, pp. 3839–3842, 2000.

[77] M. O. Blunt, J. C. Russell, M. del Carmen Giménez-Lopez, N. Taleb, X. Lin, M. Schröder, N. R. Champness, and P. H. Beton, "Guest-induced growth of a surface-based supramolecular bilayer," *Nature Chemistry*, vol. 3, p. 74, 2010.

[78] R. Gutzler, H. Walch, G. Eder, S. Kloft, W. M. Heckl, and M. Lackinger, "Surface mediated synthesis of 2d covalent organic frameworks: 1,3,5-tris(4-bromophenyl)benzene on graphite(001), Cu(111), and Ag(110)," *Chemical Communications*, 2009.

[79] H. Kondoh, N. Saito, F. Matsui, T. Yokoyama, , and T. Ohta, "Structure of alkanethiolate monolayers on Cu(100): self-assembly on the four-fold-symmetry surface," *J. Phys. Chem. B*, vol. 105, no. 51, p. 1287012878, 2001.

[80] J. A. Theobald, N. S. Oxtoby, M. A. Phillips, N. R. Champness, and P. H. Beton, "Controlling molecular deposition and layer structure with supramolecular surface assemblies," *Nature*, vol. 424, pp. 1029–1031, 2003.

[81] K. W. Kolasinski, *Surface Science: Foundations of Catalysis and Nanoscience*, 3rd ed. Wiley, 2012, ch. 3: Chemisorption Physisorption and dynamics.

[82] J. A. Venables, *Introduction to Surface and Thin film Processes*. Cambridge University Press, 2000, ch. 4: Surface processes in adsorption.

[83] T. G. Stange, R. Mathew, D. F. Evans, and W. A. Hendrickson, "Scanning tunneling microscopy and atomic force microscopy characterization of polystyrene spin-coated onto silicon surfaces," *Langmuir*, vol. 8, no. 3, pp. 920–926, 1992.

[84] K. B. Blodgett, "Molecular films of fatty acids on glass," *J. Am. Chem. Soc.*, vol. 56, no. 2, p. 495, 1934.

[85] K. B. Blodgett, "Films built by depositing successive monomolecular layers on a solid surface," *J. Am. Chem. Soc*, vol. 57, pp. 1007–1022, 1935.

[86] K. B. Blodgett and I. Langmuir, "Built-up films of barium stearate and their optical properties," *Physical Review*, vol. 51, pp. 964–982, 1937.

[87] M. Rosoff, Ed., *Nano-Surface Chemistry*. Marcell Dekker Inc, 2002.

[88] G. Roberts, Ed., *Langmuir-Blodgett Films*. Plenum press, 1990.

[89] G. L. Gaines, *Insoluble monolayers at liquid-gas interfaces*. Wiley Interscience, 1966.

[90] J. A. Sherwin, Ed., *Langmuir Monolayers in Thin Film Technology*. Nova Science Publishers Inc., 2011.

[91] P. Atkins and J. de Paula, *Atkins' Physical Chemistry*, 7th ed. Oxford University Press, 2002, ch. 21, p. 704.

[92] J. D. Watson and F. H. C. Crick, "Molecular structure of nucleic acids," *Nature*, vol. 171, p. 737, 1953.

[93] J. E. Freund, M. Edelwirth, P. Kröbel, and W. M. Heckl, "Structure determination of two-dimensional adenine crystals on graphite," *Physical Review B*, vol. 55, no. 8, pp. 5394–7, 1997.

[94] D. J. Duchamp and R. E. Marsh, "The crystal structure of trimesic acid (benzene-1,3,5-tricarboxylic acid)," *Acta Crystallographica Section B*, vol. 25, no. 1, pp. 5–19, Jan 1969. [Online]. Available: http://dx.doi.org/10.1107/S0567740869001713

[95] S. V. Kolotuchin, P. A. Thiessen, E. E. Fenlon, S. R. Wilson, C. J. Loweth, and S. C. Zimmerman, "Self-assembly of 1-3-5-benzenetricarboxylic (trimesic) acid and its analogues," *Chemistry: A European Journal*, vol. 5, no. 9, pp. 2537–2547, 1999.

[96] M. Lackinger, S. Griessl, W. M. Heckl, M. Hietschold, and G. W. Flynn, "Self-assembly of trimesic acid at the liquid-solid interfacesa study of solvent-induced polymorphism," *Langmuir*, 2005.

[97] V. V. Korolkov, S. Allen, C. J. Roberts, and S. J. B. Tendler, "Green chemistry approach to surface decoration: Trimesic acid self- assembly on HOPG," *Journal of Physical Chemistry C*, vol. 116, pp. 11 519–11 525, 2012.

[98] L. M. A. Perdigao, E. W. Perkins, J. Ma, P. A. Staniec, B. L. Rogers, N. R. Champness, and P. H. Beton, "Bimolecular networks and supramolecular traps on Au(111)," *J. Phys. Chem. B*, vol. 110, pp. 12 539–12 542, 2006.

[99] D. L. Keeling, N. S. Oxtoby, C. Wilson, M. J. Humphry, N. R. Champness, and P. H. Beton, "Assembly and processing of hydrogen bond induced supramolecular nanostructures," *Nano Letters*, vol. 3, pp. 9–12, 2003.

[100] P. A. Staniec, L. M. A. Perdigao, A. Saywell, N. R. Champness, and P. H. Beton, "Hierarchical organisation on a two-dimensional supramolecular network," *ChemPhysChem*, vol. 8, p. 2177 2181, 2007.

[101] M. Mura, F. Silly, G. A. D. Briggs, M. R. Castell, and L. N. Kantorovich, "H-bonding supramolecular assemblies of ptcdi molecules on the au(111) surface," *J. Phys. Chem. C*, vol. 113, pp. 21 840–21 848, 2009.

[102] J. C. Swarbrick, J. Ma, J. A. Theobald, N. S. Oxtoby, J. N. OShea, N. R. Champness, and P. H. Beton, "Square, hexagonal, and row phases of ptcda and ptcdi on ag-si(111)$\sqrt{3}x\sqrt{3}r30°$," *J. Phys. Chem. B*, vol. 109, pp. 12 167–12 174, 2005.

[103] B. Uder, C. Ludwig, J. Petersen, B. Gomph, and W. Z. Eisenmenger, "Stm characterisation of organic molecules on h-terminated si(111)," *Phys. B*, vol. 97, pp. 389–390, 1995.

[104] F. Silly, A. Q. Shaw, M. R. Castell, G. A. D. Briggs, M. Mura, N. Martsinovich, , and L. Kantorovich, "Melamine structures on the au(111) surface," *J. Phys. Chem. C*, vol. 112, pp. 11 476–11 480, 2008.

[105] J. Greenwood, H. A. Fruchtl, and C. J. Baddeley, "Ordered growth of upright melamine species on ni(111): A study with scanning tunnelling microscopy and reflection absorption infrared spectroscopy," *J. Phys. Chem. C*, 2012.

[106] R. Thomas and G. U. Kulkarni, "A hydrogen-bonded channel structure formed by a complex of uracil and melamine," *Beilstein Journal of Organic Chemistry*, vol. 3, p. 17, 2007.

[107] J. A. Gardener, O. Y. Shvarova, G. A. D. Briggs, , and M. R. Castell, "Intricate hydrogen-bonded networks: Binary and ternary combinations of uracil, ptcdi, and melamine," *J. Phys. Chem. C*, 2010.

[108] A. Ranganathan, V. R. Pedireddi, and C. N. R. Rao, "Hydrothermal synthesis of organic channel structures: 1:1 hydrogen-bonded adducts of melamine with cyanuric and trithiocyanuric acids," *Journal of the American Chemical Society*, vol. 121, pp. 1752–1753, 1999.

[109] V. R. Pedireddi, S. Chatterjee, A. Ranganathan, and C. N. R. Rao, "Noncovalent synthesis of layered and channel structures involving sulfur-mediated hydrogen bonds," *Journal of the American Chemical Society*, vol. 119, pp. 10 867–8, 1997.

[110] W. M. Haynes, Ed., *CRC Handbook of Chemistry and Physics*, 93rd ed. CRC Press, 2012, ch. 9: Molecular Structure and Spectroscopy, pp. 9–74: Electronegativity.

[111] S. B. Lei, C. Wang, S. X. Yin, H. N. Wang, F. Xi, H. W. Liu, B. Xu, L. J. Wan, and C. L. Bai, "Surface stabilized porphyrin and phthalocyanine two-dimensional network connected by hydrogen bonds," *J. Phys. Chem. B*, vol. 105, pp. p10 838–10 841, 2001.

[112] L. Grill, M. Dyer, L. Lafferentz, M. Persson, M. V. Peters, and S. Hecht, "Nano-architectures by covalent assembly of molecular building blocks," *Nature Nanotechnology*, vol. 2, pp. p687–691, 2007.

[113] F. Ullmann and J. Bielecki, "Synthesis in the biphenyl series," *J. Chem. Ber.*, vol. 34, p. 2174, 1901.

[114] J. A. Lipton-Duffin, O. Ivasenko, D. F. Perepichka, and F. Rosei, "Synthesis of polyphenylene molecular wires by surface-confined polymerization," *Small*, vol. 5, pp. 592–597, 2009.

[115] S. Weigelt, C. Busse, C. Bombis, M. M. Knudsen, K. V. Gothelf, E. Lægsgaard, F. Besenbacher, and T. R. Linderoth, "Surface synthesis of 2d branched polymer nanostructures," *Angewandte Chemie International Edition*, vol. 47, pp. 4406–4410, 2008.

[116] M. Treier, N. V. Richardson, and R. Fasel, "Fabrication of surface-supported low-dimensional polyimide networks," *Journal of the American Chemical Society*, vol. 130, p. 1405414055, 2008.

[117] C.-Z. Guan, D. Wang, and L.-J. Wan, "Construction and repair of highly ordered 2D covalent networks by chemical equilibrium regulation," *Chemical Communications*, vol. 48, pp. 2943–2945, 2012.

[118] G. Eder, E. F. Smith, I. Cebula, W. M. Heckl, P. H. Beton, and M. Lackinger, "Solution preparation of two-dimensional covalently linked networks by polymerization of 1-3-5-tri(4-iodophenyl)benzene on Au(111)," *ACS Nano*, vol. 7, no. 4, p. 3014, 2013.

[119] M. Xi and B. E. Bent, "Mechanisms of the ullmann coupling reaction in adsorbed monolayers," *Journal of the American Chemical Society*, vol. 115, 1993.

[120] J. Hassan, M. S. Vignon, C. Gozzi, E. Schulz, and M. Lemaire, "ArylAryl bond formation one century after the discovery of the ullmann reaction," *Chemical Review*, vol. 102, p. 1359, 2002.

[121] S.-W. Hla, L. Bartels, G. Meyer, and K.-H. Rieder, "Inducing all steps of a chemical reaction with the scanning tunneling microscope tip: Towards single molecule engineering," *Physical Review Letters*, vol. 85, p. 2777, 2000.

[122] J. Cai, P. Ruffieux, R. Jaafar, M. Bieri, T. Braun, S. Blankenburg, M. Muoth, A. P. Seitsonen, M. Saleh, X. Feng, K. Müllen, and R. Fasel, "Atomically precise bottom-up fabrication of graphene nanoribbons," *Nature*, vol. 466, pp. 470–473, 2010.

[123] O. Ermer, "Fivefold-diamond structure of adamantane-1,3,5,7-tetracarboxylic acid," *Journal of the American Chemical Society*, vol. 110, pp. 3141–3154, 1988.

[124] S. J. Coles, R. Holmes, M. B. Hursthouse, and D. J. Price, "Biphenyl-3,3',5,5'-tetracarboxylic acid," *Acta Crystallographica*, vol. E58, pp. o626–o628, 2002.

[125] M. O. Blunt, J. C. Russell, M. del Carmen Giménez-Lopez, J. P. Garrahan, X. Lin, M. Schröder, N. R. Champness, and P. H. Beton, "Random tiling and topological defects in a two-dimensional molecular network," *Science*, vol. 322, p. 1077, 2008.

[126] A. Stannard, J. C. Russell1, M. O. Blunt, C. Salesiotis, M. del Carmen Giménez-López, N. Taleb, M. Schröder, N. R. Champness, J. P. Garrahan, and P. H. Beton, "Broken symmetry and the variation of critical properties in the phase behaviour of supramolecular rhombus tilings," *Nature Chemistry*, vol. 4, pp. 112–116, 2012.

[127] M. O. Blunt, J. C. Russell, M. del Carmen Giménez-Lopez, J. P. Garrahan, X. Lin, M. Schröder, N. R. Champness, and P. H. Beton, "Supplementary information from: Random tiling and topological defects in a two-dimensional molecular network," *Science*, vol. 322, p. 1077, 2008.

[128] I. Horcas, R. Fernandez, J. Gomez-Rodriguez, J. Colchero, J. Gomez-Herrero, and A. M. Baro, "WSxM: A software for scanning probe microscopy and a tool for nanotechnology," *Review of Scientific Instruments*, 2007.

[129] http://inkscape.org/, "Inkscape open source graphics editor software," v0.48.

[130] N. I. of Health, "ImageJ: image processing and analysis in Java," *http : //rsbweb.nih.gov/ij/*.

[131] I. Cebula, E. F. Smith, M. del Carmen Gimenez-Lopez, S. Yang, M. Schröder, N. R. Champness, and P. H. Beton, "Packing of isophthalate tetracarboxylic acids on au(111): Rows and disordered herringbone structures," *J. Phys. Chem. C*, vol. 117, pp. 18 381–18 385, 2013.

[132] J. C. Russell, *Supramolecular Network Formation From Solution-based Deposition Techniques*. University of Nottingham, 2011, ch. 4.5: Manipulation of the TPTC network, pp. 84–91, available in the University of Nottingham ethesis library at *http : //etheses.nottingham.ac.uk/3080/1/539203.pdf*.

[133] N. R. Champness, Private communication.

[134] R. J. Kominar, M. J. Krech, and S. J. W. Price, "Pyrolysis of bromobenzene by the toluene carrier technique and determination of d(C_6H_5Br)," *Canadian Journal of Chemistry*, vol. 56, pp. 1589–1592, 1978.

[135] M. Szwarc, "Energy of the central C-C bond in diphenyl," *Nature*, vol. 161, pp. 890–891, 1948.

[136] H. Walch, R. Gutzler, T. Sirtl, G. Eder, and M. Lackinger, "Material- and orientation-dependent reactivity for heterogeneously catalyzed carbonbromine bond homolysis," *J. Phys. Chem. C*, vol. 114, p. 1260412609, 2010.

[137] M. O. Blunt, J. C. Russell, N. R. Champness, and P. H. Beton, "Templating molecular adsorption using a covalent organic framework," *Chemical Communications*, vol. 46, pp. 7157–7159, 2010.

[138] J. C. Russell, M. O. Blunt, J. M. Garfitt, D. J. Scurr, M. Alexander, N. R. Champness, and P. H. Beton, "Dimerization of tri(4-

bromophenyl)benzene by aryl-aryl coupling from solution on a gold surface," *Journal of the American Chemical Society*, 2011.

[139] P. Metrangolo, F. Meyer, T. Pilati, G. Resnati, and G. Terraneo, "Halogen bonding in supramolecular chemistry," *Angewandte Chemie International Edition*, vol. 47, no. 33, pp. 6114–6127, 2008.

[140] D. F. Shriver and P. W. Atkins, *Inorganic Chemistry*, 3rd ed. Oxford University Press, 1999, ch. 9.10 The d-block metals: Noble Character.

[141] A. Schulz and M. Hargittai, "Structural variations and bonding in gold halides," *Chem. Eur. J.*, vol. 7, no. 17, 2001.

[142] M. D. Hanwell, D. E. Curtis, D. C. Lonie, T. Vandermeersch, E. Zurek, and G. R. Hutchison, "Avogadro: an advanced semantic chemical editor, visualization, and analysis platform," *Journal of Cheminformatics*, vol. 4, no. 17, 2012.

[143] E. Pauliac-Vaujour, A. Stannard, C. P. Martin, M. O. Blunt, I. Notingher, P. J. Moriarty, I. Vancea, and U. Thiele, "Fingering instabilities in dewetting nanofluids," *Physical Review Letters*, vol. 100, p. 176102, 2008.

[144] Y. Gamo, N. Nagashima, M. Wakabayashi, M. Terai, and C. Oshima, "Atomic structure of monolayer graphite formed on ni(111)," *Surface Science*, vol. 374, pp. 61–67, 1997.

[145] H. J. Grabke, W. Paulitschke, G. Tauber, and H. Vierhaus, "Equilibrium surface segregation of dissolved nonmetal atoms on iron(100) faces," *Surface Science*, vol. 63, p. 377, 1977.

[146] J. C. Hamilton and J. M. Blakely, "Carbon segregation to single crystal surfaces of Pt Pd and Co," *Surface Science*, vol. 91, p. 199, 1980.

[147] A. L. V. de Parga, F. Calleja, B. Borca, M. C. G. P. Jr., J. J. Hinarejos, F. Guinea, and R. Miranda, "Periodically rippled graphene: growth and spatially resolved electronic structure," *Physical Review Letters*, vol. 100, p. 056807, 2008.

[148] T. Fujita, W. Kobayashi, and C. Oshima, "Novel structures of carbon layers on a Pt(111) surface," *Surface and Interface Analysis*, vol. 37, no. 2, p. 120, 2005.

[149] J. Coraux, A. T. N'Diaye, C. Busse, and T. Michely, "Structural coherency of graphene on Ir(111)," *Nano Letters*, vol. 8, no. 2, pp. 567–570, 2008.

[150] M. Eizenberg and J. M. Blakely, "Carbon monolayer phase condensation on Ni (111)," *Surface Science*, vol. 82, pp. 228–236, 1979.

[151] M. Losurdo, M. M. Giangregorio, P. Capezzuto, and G. Bruno, "Graphene cvd growth on copper and nickel: role of hydrogen in kinetics and structure," *Phys. Chem. Chem. Phys.*, vol. 13, pp. 20 836–20 843, 2011. [Online]. Available: http://dx.doi.org/10.1039/C1CP22347J

[152] A. Dahal and M. Batzill, "Graphene-nickel interfaces: a review," *Nanoscale*, vol. 6, pp. 2548–2562, 2014. [Online]. Available: http://dx.doi.org/10.1039/C3NR05279F

[153] Y. Souzu and M. Tsukada, "Electronic states and scanning tunneling spectroscopy image of monolayer graphite on a nickel (111) surface by the dv-x method," *Surface Science*, vol. 326, no. 12, pp. 42 – 52, 1995. [Online]. Available: http://www.sciencedirect.com/science/article/pii/0039602894005583

[154] K. S. Kim, Y. Zhao, H. Jang., S. Y. Lee, J. M. Kim, K. S. Kim, J. H. Ahn, P. Kim, J. Y. Choi, and B. H. Hong, "Large-scale pattern growth of graphene films for stretchable transparent electrodes," *Nature Letters*, vol. 457, pp. 706–710, February 2009.

[155] A. N. Obraztsov, E. A. Obraztsova, A. V. Tyurnina, and A. A. Zolotukhim, "Chemical vapor deposition of thin graphite films of nanometer thickness," *Carbon*, vol. 45, pp. 2017–2021, 2007.

[156] Y. Kim, W. Song, S. Y. Lee, C. Jeon, W. Jung, M. Kim, and C.-Y. Park, "Low-temperature synthesis of graphene on nickel foil by microwave plasma chemical vapor deposition," *Applied Physics Letters*, vol. 98, p. 263106, 2011.

[157] M. Singleton and P. Nash, "The C-Ni (carbon-nickel) system," *Bulletin of alloy phase diagrams*, vol. 10, no. 2, pp. 121–126, 1989.

[158] Q. Yu, J. Lian, S. Siriponglert, H. Li, Y. P. Chen, and S. Pei, "Graphene segregated on Ni surfaces and transferred to insulators," *Applied Physics Letters*, vol. 93, p. 113103, 2008.

[159] A. N. Obraztsov, A. A. Zolotukhin, A. O. Ustinov, A. P. Volkov, and Y. P. Svirko, "Chemical vapor deposition of carbon films: in-situ plasma diagnostics," *Carbon*, vol. 41, pp. 836–839, 2003.

[160] A. J. Pollard, R. R. Nair, S. N. Sabiki, C. R. Staddon, L.M.A.Perdigao, C. H. Hsu, J. M. Garfitt, S. Gangopadhyay, H. F. Gleeson, A. K. Geim, and P. H. Beton, "Formation of monolayer graphene by annealing sacrificial nickel thin films," *Journal of Physical Chemistry C*, vol. 113, pp. 16 565–16 567, 2009.

[161] The evaporator used to deposit the Ni films was supplied commercially by Edwards, model Auto 306.

[162] Silicon Materials, Viktor-Frankl-Str. 20, D - 86916 Kaufering, Germany.

[163] C. Kusch, B. Winter, R. Mitzner, A. G. Silva, E. E. B. Campbell, and I. V. Hertel, "Stability of photo-excited c60 chemisorbed on ni(111)," *Chemical Physics Letters*, vol. 275, pp. 469–476, 1997.

[164] C. Cepek, A. Goldoni, and S. Modesti, "Chemisorption and fragmentation of c60 on pt(111) and ni(110," *Physical Review B*, vol. 53, p. 7466, 1996.

[165] N. N. Greenwood and A. Earnshaw, *Chemistry of the Elements*, 2nd ed. Elsevier, 1997, ch. 25:Iron, Ruthenium and Osmium, p. 1084,

online version available at: $http://app.knovel.com/hotlink/toc/id:kpCEE00006/chemistry-elements-2nd$.

[166] H. S. Rawdon and M. G. Lorentz, "Metallographic etching reagents: II. for copper alloys, nickel. and the alpha alloys of nickel," *Scientific papers of the bureau of Standards*, vol. 17, no. 435, p. 635, 1922.

[167] "Micro chem corporation, 1254 chesnut street, newton, ma 02464," $http://www.microchem.com$, email: mcc@microchem.com.

[168] *NANO PMMA and Co-polymer data sheet*, Micro Chem Corp., 2001.

[169] A. K. Geim and K. S. Novoselov, "," *Nature Materials*, vol. 6, p. 183, 2007.

[170] P. Blake, E. W. Hill, A. H. C. Neto, K. S. Novoselov, D. Jiang, R. Yang, T. J. Booth, and A. K. Geim, "Making graphene visible," *Applied Phycis Letters*, vol. 91, p. 063124, 2007.

[171] J. M. Hollas, *Modern Spectroscopy*, 4th ed. John Wiley & Sons Ltd, 2004.

[172] P. Atkins and J. de Paula, *Atkins' Physical Chemistry*, 8th ed. Oxford university press, 2006, ch. 13-Molecular spectroscopy 1: rotational and vibrational spectra.

[173] M. A. Pimenta, G. Dresselhaus, M. S. Dresselhaus, L. G. Cançado, A. Jorio, and R. Saito, "Studying disorder in graphite-based systems by Raman spectroscopy," *Physical Chemistry Chemical Physics*, vol. 9, pp. 1276–1291, 2007.

[174] F. Tuinstra and J. L. Koenig, "Raman spectrum of graphite," *Journal of Chemical Physics*, vol. 53, no. 3, pp. 1126–1130, 1970.

[175] A. C. Ferarri, J. C. Meyer, V. Scardaci, C. Casiraghi, M. Lazzeri, F. Mauri, S. piscanec, D. Jiang, K. S. Novoselov, S. Roth, and A. K. Geim, "Raman spectrum of graphene and graphene layers," *Physical Review Letters*, vol. 97, p. 187401, November 2006.

[176] T. McKindra, M. J. O'Keefea, Z. Xieb, and Y. Lub, "Characterization of diamond thin films deposited by a CO_2 laser-assisted combustion-flame method," *Materials Characterization*, vol. 61, pp. 611–667, 2010.

[177] H. Hiura, T. W. Ebbesen, and K. Tanigaki, "Raman studies of carbon nanotubes," *Chemical Physics Letters*, vol. 202, no. 6, pp. 509–512, 1993.

[178] D. S. Bethune, G. Meijer, W. C. Tang, H. J. Rosen, W. G. Golden, H. Seki, C. A. Brown, and M. S. de Vries, "Vibrational raman and infrared spectra of chromotographically separated C_{60} and C_{70} fullerene clusters," *Chemical Physics Letters*, vol. 179, no. 1, pp. 181–186, 1991.

[179] The R Foundation for Statistical Computing, "R for statistical computing and graphics," $http://www.r-project.org/$, v3.0.2 2013.

[180] S. Lee, K. Lee, and Z. Zhong, "Wafer scale homogeneous bilayer graphene films by chemical vapor deposition," *Nano Letters*, vol. 10, no. 11, pp. 4702–4707, 2010. [Online]. Available: http://pubs.acs.org/doi/abs/10.1021/nl1029978

[181] X. Li, W. Cai, I. H. Jung, J. H. An, D. Yang, A. Velamakanni, R. Piner, L. Colombo, and R. S. Ruoff, "Synthesis, characterization, and properties of large-area graphene films," *ECS Trans*, vol. 19, no. 5, pp. 41–52, 2009.

[182] A. Reina, X. Jia, J. Ho, D. Nezich, H. Son, V. Bulovic, M. S. Dresselhaus, and J. Kong, "Large area few-layer graphene films on arbitrary substrates by chemical vapor deposition," *Nano Letters*, vol. 9, no. 1, pp. 30–35, 2009.

[183] J.-H. Lee, E. K. Lee, W.-J. Joo, Y. Jang, B.-S. Kim, J. Y. Lim, S.-H. Choi, S. J. Ahn, J. R. Ahn, M.-H. Park, C.-W. Yang, B. L. Choi, S.-W. Hwang, and D. Whang, "Wafer-scale growth of single-crystal monolayer graphene on reusable hydrogen-terminated germanium,"

Science, vol. 344, no. 6181, pp. 286–289, 2014. [Online]. Available: http://www.sciencemag.org/content/344/6181/286.abstract

[184] J. Kim, H. Park, J. B. Hannon, S. W. Bedell, K. Fogel, D. K. Sadana, and C. Dimitrakopoulos, "Layer-resolved graphene transfer via engineered strain layers," *Science*, vol. 342, no. 6160, pp. 833–836, 2013. [Online]. Available: http://www.sciencemag.org/content/342/6160/833.abstract

Acronym Definitions

BPTC	biphenyl-3,3',5,5'-tetracarboxylic acid
DBrBA	10,10'-dibromo-9,9'-bianthryl
FCC	Face centered cubic
HAS	Helium atom scattering
HCP	Hexagonal close packed
HOMO	Highest occupied molecular orbital
HOPG	Highly oriented pyrolytic graphite
LDOS	Local density of states
LEED	Low energy electron diffraction
LUMO	Lowest unoccupied molecular orbital
NMR	Nuclear Magnetic Resonance
PTCDI	perylene tetra-carboxylic di-imide
QPTC	quaterphenyl-3,3',5,5' -tetracarboxylic acid
RHEED	Resonance high energy electron diffraction
SAM	Self assembled monolayers
SCOF	Surface covalent organic frameworks
SPM	Scanning probe microscope/microscopy
STM	Scanning tunnelling microscope/microscopy
TBPB	1,3,5-tri(4-bromophenyl)benzene
TBPQ	$3, 3'', 5, 5''$-tetra(4-bromophenyl)quaterphenyl
TEM	Transmission electron microscopy
TIBP	1,3,5-Tri(4-iodophenyl)benzene
TPTC	p-terphenyl-3,5,3,5-tetracarboxylic acid
UHV	Ultra high vacuum

List of Figures